Evaluation of Impact and Fatigue properties of Austempered Ductile Iron

MARCO DAL COROBBO AND SERGIO ARIAS

No.
Masters Thesis:
Department of Materials and Manufacturing Technology
Chalmers University of Technology
SE-412 96 Göteborg
Sweden
Telephone: + 46 (0)31-772 12 50

Printed by Chalmers Reproservice
Göteborg, Sweden 2009

Evaluation of Impact and Fatigue properties of Austempered Ductile Iron

MARCO DAL COROBBO AND SERGIO ARIAS
Department of Materials and Manufacturing Technology

Abstract

Austempered Ductile Iron (ADI) proved to be an excellent material as it possesses attractive properties: high strength, ductility and toughness are combined with good wear resistance and machinability. In this work impact and the fatigue properties have been evaluated for low alloyed Austempered Ductile Iron. To do this, Charpy-type impact test for austempered ductile iron was performed by the standard ASTM A 327M and Fatigue Crack Growth Rates (FCGR) were measured by the standard ASTM E 647. It was found that impact energy is related with the morphology of the graphite nodules in the microstructure. In particular, the impact energy increases when the nodularity and the nodule count increase, and the nodule size decreases. A clear relation with the amount of retained austenite wasn't found. For the fatigue properties it was found that these were related with the morphology of microstructure (graphite nodules, amount of retained austenite and its carbon content). However, it was observed that the the crack initiation was mainly affected by the presence of defects as porosity or carbides. When the preferential crack path was observed between two neighboring nodules, the crack growth rate increased when two graphite nodules were closer. The growth of the crack depends on the orientation of the ferrite laths, but, in this work, it was observed that the crack path probably takes place along the austenite/ferrite interface. Furthermore, it was found that the likelihood of crack formation, facilitated by decohesion of the graphite nodules, increased with nodule size.

Preface

This diploma thesis is based on work carried out in the Department of Materials and Manufacturing Technology at Chalmers University of Technology, during the autumn of 2008 and spring of 2009.

Acknowledgements

We want to take advantage of the following lines to express our gratitude with all the people which contribute to the success in finishing the present work.

Our first mention and special thanks are destined to our supervisors in Sweden, Henrik Borgström and Kenneth Hamberg from the department of Materials and Manufacturing Technology at Chalmers, for their guidance and experience on the topic. Their constructive criticism and discussions during the work served us to achieve a high level of understanding. We wish also to thank Prof. Lars Nyborg, from the department of Materials and Manufacturing Technology of Chalmers, for giving us the opportunity to carry out this work, and our supervisors in Italy and Spain, Professor Alberto Molinari from the University of Trento, José Manuel Torralba and Monica Campos of Carlos III University in Madrid, for giving us the opportunity to study abroad, and for supporting us with this work.

We also want to mention the staff of the department of Materials and Manufacturing Technology who despite of not being involved directly in this work, still unselfishly helped us with our tasks. To all of them thanks, but we are especially grateful for the support provided by Dr. Peter Sotkovszki and Dr. Yiming Yao.
Final mentions, the last but not the least, is for our families, for giving us the opportunity to study abroad and the support during all the time spent far from home. Special thanks also to all our “home” friends and all the “new” friends met in our unforgettable experience in Sweden.

Sergio Arias and Marco Dal Corobbo

INDEX

1. INTRODUCTION

Our highly developed technological society continues to exert enormous demand for light, durable and cost effective materials. This is why we continually look for new materials that combine excellent mechanical properties and characteristics as well as improving those already in service. In recent years there has been significant interest in the properties and development of Austempered Ductile Iron. This Austempered Ductile Iron, ADI, refers to ductile iron that undergoes a heat treatment called austempering. It appears that ADI could be developed into a major engineering material with a wide range of versatile engineering properties.

Therefore, the context of this work has been to evaluate the impact and fatigue properties of different alloys and heat treatments proposed in collaboration with the foundry Componenta, in order to improve the alloy as well as developing a more feasible industrial heat treatment. The impact and fatigue properties were chosen because they are important features for the material application. Moreover an extensive literature survey was conducted to compare our materials with others, but also to try to propose a new point of discussion or find suggestions for future studies.

The present work is a continuation of Caroline Glondu [5] and Javier Hidalgo [4] master thesis' conducted at Chalmers University of Technology, with a different direction.

2. AN OVERVIEW OF AUSTEMPERED DUCTILE IRON

Austempered Ductile Iron (ADI), also known as ausferritic ductile iron, is the most recent addition to the ductile iron family. It is produced by giving conventional ductile iron a special heat treatment called “austempering” [2]. The austempering heat treatment transforms ductile iron to ADI, bringing about excellent strength, toughness, and fatigue characteristics. ADI is stronger per unit weight than aluminium, as wear resistant as steel and has the potential for up to 50% cost savings [3].

For the designer ADI is a most versatile material, enabling innovative solutions to new and current problems. By selecting precise heat treatment parameters a specific set of properties can be achieved. The lower hardness ductile iron castings are used in structural applications, often where weight and cost reduction are important. Wear resistance is superior to steel at any given hardness level, making the higher hardness grades ideal for mining, construction, agricultural and similar high abrasion applications [3].

ADI competes favourably with steel forgings, especially for heavy-duty parts where reliability is paramount. It is used to upgrade from standard ductile irons, and as a substitute for manganese steel and nickel-hard materials. When strength is required ADI is particularly cost-effective: tensile and yield values are twice as high as standard ductile iron; fatigue strength is 50% higher and it can be enhanced by shot peening or fillet rolling. With its high strength-to-weight ratio ADI can even replace aluminium when reduced section sizes are acceptable [3].

2.1. History of Austempered Ductile Iron

The austempering process is neither new nor novel and has been utilized since the 1930's on cast and wrought steels [2]. In fact this kind of heat treatment had been applied on steel in 1933 and on grey cast iron in 1937 [5].

Nearly 50 years after its discovery ADI is still widely regarded as a "new material". A major reason for this was the slow commercialisation of the austempering process. ADI remained a laboratory curiosity until 1972, the year when the austempering process was firstly commercially applied to the ductile iron, when a limited facility was set up to process a small compressor crankshaft in the USA [3]. However the first truly viable commercial service was delayed until the introduction of new furnace developments at Applied Process Inc in Michigan during 1984 [3]. Since the 70's, considerable process modelling and material evaluation has followed, resulting in wider understanding and acceptance of ADI [3].

In the latter nineties the development of Ductile Iron introduced the use of thin walled parts, in order to increase the strength to weight ratio and its competitiveness against lighter alloys [18].

2.2. Market and applications of Austempered Ductile Iron

Over the most recent twenty years, heat treatment specialists and equipment engineers have refined the austempering process and plants to enable reliable production of high grade austempered materials. This has fuelled demand and a family of austempered Irons and Steels are now routinely produced. Of these ADI is becoming the material of choice as designers and engineers, which seek cost effective performance from their components and systems. In particular, manufacturers engaged in moving parts and safety critical items have benefited from increased strength, greater wear resistance, noise reduction and weight saving [7]. ADI is now established in many major markets [7] as seen in Figure 2.1.

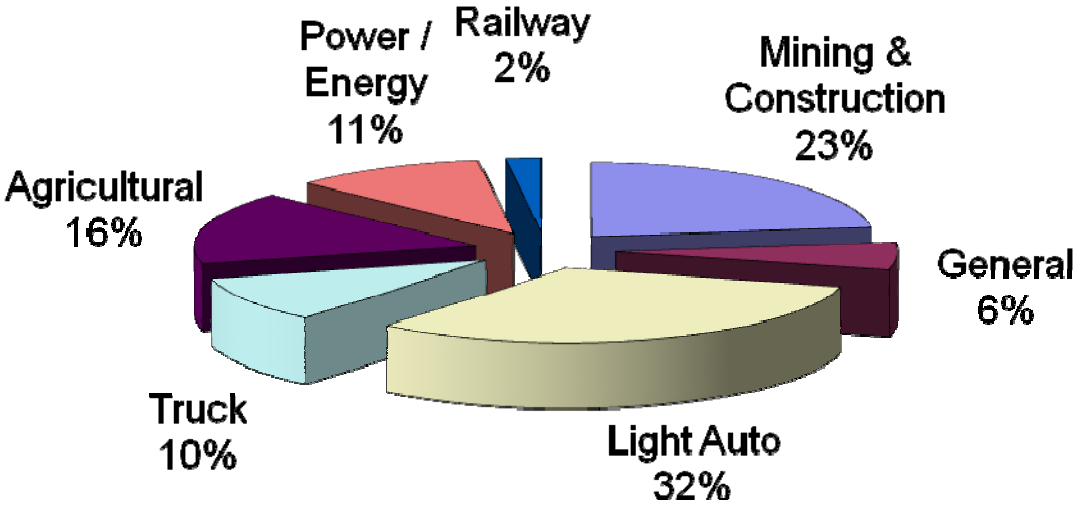

Figure 2.1: ADI treatment market distribution 2004, adapted from [7].

In *Farm Machinery and Equipment* the equipment used in farming is subjected to high wear and heavy loads. Performance is constantly being pushed to the next level as products are expected to last longer and be cost effective. The agricultural industry has therefore taken a keen interest in ADI and other austempered materials for their excellent wear characteristics.

In *Heavy Truck*, economic growth drives the need to haul heavier loads over longer distances, resulting in more time between vehicle maintenance and some difficult engineering challenges. The Heavy Truck industry recognised the potential benefits of austempering solutions many years ago. Manufacturers took advantage of the versatility of ADI to introduce innovative light weight, high performance parts.

In *Machinery Conveyors and Tooling* markets have benefited greatly by incorporating ADI and other austempered alloys in their equipment designs. Lighter weight, easier to manufacture castings have made components less expensive, last longer and reduced the weight of individual tools or material handling systems.

In the *Railway Industry* products, improvements in safety and transport efficiency: wear plates, suspension housings and suspension covers are examples of ADI application.

Construction Equipment can benefit greatly from the use of tough, wear resistant austempered Irons and Steels. Whether for ground engaging components such as bucket teeth or engine and powertrain parts, ADI and other austempered materials can improve the performance of the heavy duty equipment.
For high performance *gear and powertrain manufacturers*, austempered materials offer greater wear resistance, reduced noise, improved bending and contact fatigue, as well as increased strength and durability.
Austempering an iron, steel, or powdered metal component (depending on the specific application) can therefore deliver a valuable competitive edge. Companies such as Delphi Automotive, Dana Corporation, Ford Motor Company, AGCO, John Deere, and General Motors are among those selecting ADI and austempered steels for production and design.

The *automotive industry* is constantly looking to increase performance, reduce the cost and weight of the vehicles they produce, to boost the drive for lower emission as well as better fuel economy.
Austempered materials have a proven track record of providing strength and dependability for safety components, suspension systems, and drivetrain applications.

In *Mining/Forestry Equipment* the difficult applications and large scale engineering demand high performance and set intriguing design problems. ADI has met these challenges, providing improved strength and wear resistance, as seen in heavy-duty components.

Even the *sports goods industry* has adopted ADI for its high strength to weight and superior wear resistance: bobsleigh runners, sword blades, gun components are examples of ADI application for this kind of industry.

3. THE MICROSTRUCTURE AND HEAT TREATMENT OF AUSTEMPERED DUCTILE IRON

3.1. The microstructure of Austempered Ductile Iron

The factor that characterizes ADI is the property of combining good elongation and toughness with high tensile strength, which is a combination that increases the resistance to wear and fatigue when compared to other ductile irons. These desirable mechanical properties are associated with a unique austempered microstructure which consist of graphite nodules, acicular, carbide free ferrite with carbon-enriched austenite, rather than ferrite and carbide, as produced in normal bainitic transformation in steel [8]. When steel is austempered, the resulting microstructure consist of fine dispersion of carbide in a ferrite matrix called bainite. In ductile cast iron, the presence of a large amount of silicon suppressed the carbide formation. This microstructure in ADI be called “ausferrite” to distinguish it from the bainite structure in steels [9].

During the austempering transformation, ADI goes through a two-stage reaction. In the first stage, austenite transforms to a structure of acicular ferrite and carbon-enriched retained austenite. When ferrite forms within the austenite during the austempered process of nodular or ductile cast iron, the carbon is rejected from these regions and goes into solution in the surrounding austenite. As more and more ferrite forms, the carbon content of austenite increases. Since the carbon content of this austenite is very high (in excess of 1.0%), the austenite is stable in room temperature and hence the resulting microstructure consist of ferrite and high carbon and stable austenite [10]. This is the desired structure that provides the remarkable properties in ADI. In the second stage, when the casting is austempered longer than required for the above structure, the carbon-enriched austenite further decomposes into ferrite and carbide. In the latter case the iron contains large amount of carbide and the matrix become brittle. Therefore this reaction is undesirable and must be avoided.

The microstructure and mechanical properties of ADI can be greatly altered by suitable heat treatment process, thus the microstructure of ADI strongly depends on austempering temperature and time. Austempering to high temperatures gives place to the production of relatively thick ferrite laths in an austenite matrix enriched in carbon. When austempering

is carried out at lower temperatures, thinner needles of acicular ferrite result (Figure 3.1). If austempering time is very short, the degree of advance of the transformation is less than 100% and a percentage of untransformed austenite remains, that could transform to martensite during cooling. If austempering time is too long, as the second stage of transformation begins, Carbon precipitates in the form of carbides as described above [10].

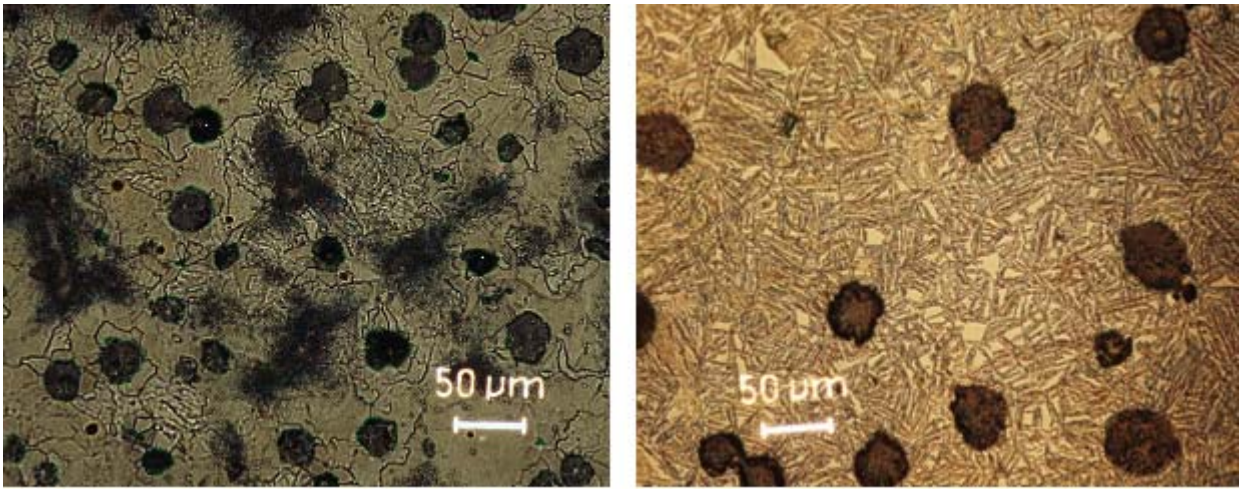

Figure 3.1: examples of matrix microstructures: as-cast DI and ADI austenized at 950°C and austempered at 360°C for 1 and 3 hours, respectively. Courtesy of Glondu [5].

The best mechanical properties in ADI are obtained after the completion of the first reaction but before the onset of the second reaction [27]. This time interval between the completion of the first reaction and the onset of the second reaction is known as the process window and it defines a restricted time-temperature domain in which the austempering heat treatment is to be carried out [26, 27]. The minimum time required for a given austempering temperature is defined by the presence in the final microstructure of ADI of no more than 3% martensite, while the maximum allowed austempering time correlates with the 90% of high carbon austenite still remained in the microstructure [26]. A successful model for the prediction of the processing window has been developed using a model for the isothermal transformation of austenite in high Si (>1,5 %wt) steels [34, 35], literature data and a linear regression technique [36, 37]. The modelling of the process window for various ADI compositions provides a guide to choosing a minimum austempering time (close to the lower boundary) to achieve the ASTM standard and simultaneously reduce the heat treatment costs [26]. In Figure 3.2 is shown an ADI

processing window predicted by a model in Pereloma et al. studies [36, 37] , from which. the austempering temperature and time can be chosen. The selection of the austempering times close to the lower boundary of the processing window allowed the significant time savings, which will result in lower production costs for heat treaters [26]; of particular interest is that the temperature range 385-430 °C was not studied [26].

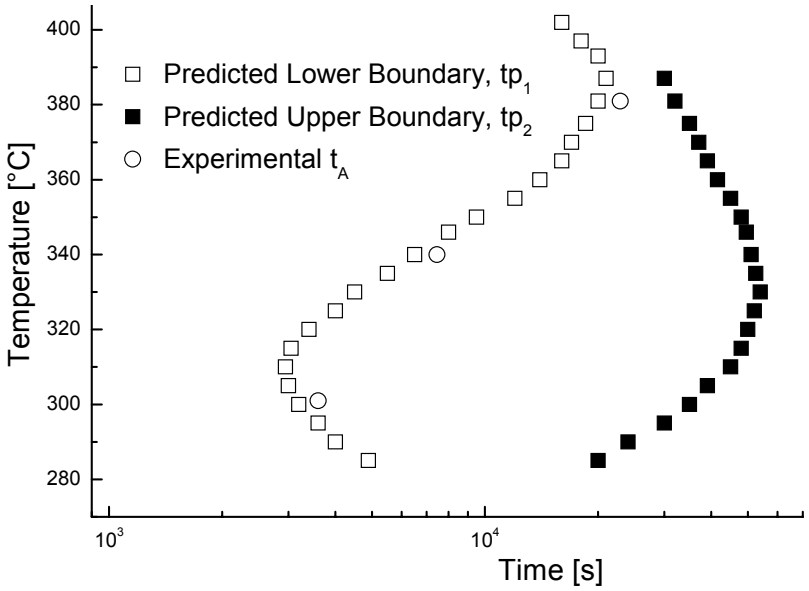

Figure 3.2: predicted processing window for studied iron and experimental austempering temperatures and times, adapted from [26].

The process window can be enlarged by the addition of alloying elements such as nickel and molybdenum; they are added to delay the transformation, and to allow the ausferritizing reaction to be completed over the whole section of the piece [27].

In conclusion, the important microstructural features are the morphology of ferrite, the retained austenite content, the carbon content of austenite, the presence or absence of carbides in austenite or ferrite [27] as well as the graphite nodules. The characteristics of the nodules in fact, must be take into account during the investigation of ADI properties. The quantity of nodules in the microstructure (nodule count), their size (usually is measured the radius or diameter of the nodules), and their shape (quantified with a parameter called nodularity, which is a measure of their roundness) can affect the behavior of the material.

3.2. Heat treatment cycle of Austempered Ductile Iron

ADI is produced by an isothermal heat treatment known as austempering, which is carried out to obtain the “ausferrite” microstructure in ductile iron. The complete ADI heat treatment cycle consists of four main stages: austenitization, quenching to the austempering temperature, austempering, cooling to room temperature (Figure 3.3).

All the different stages are of significance in determining the exact microstructure produced and each specific property is determined by the careful selection of heat treatment parameters.

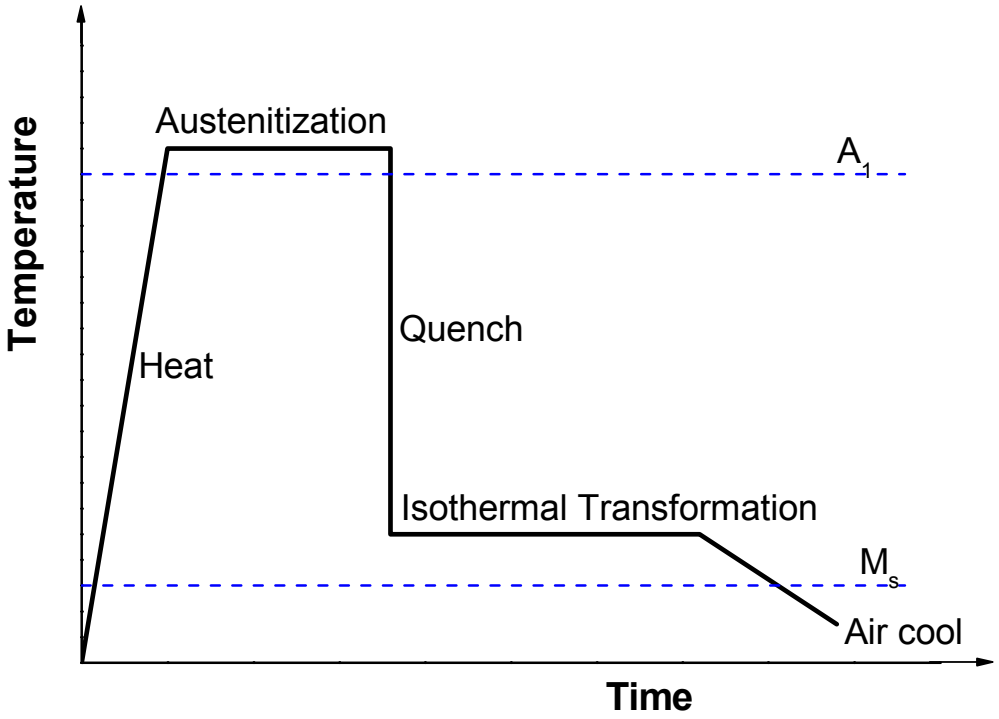

Figure 3.3: illustration of typical ADI heat treatment cycle, adapted from [11].

The Austenitization process

During austenitization, the cast component is usually heated between 850 and 950 °C for about 15 minutes to 2 hours [4]. The austenitization temperature and time are important factors that affect the microstructure and the mechanical properties of ADI. The optimum temperature and time depend on the chemical composition of the ductile iron, the graphite nodule count and the process variables like casting section size and type [6]. They have to be controlled to ensure formation of fine grain austenite and uniform carbon content in the matrix [11].

The austenitizing temperature controls the carbon content of the austenite which, in turn, affects the structure and properties of the austempered casting [6]. The austenitizing

temperature should be selected to ensure sufficient carbon transfer from the graphite nodule to the matrix occurs [5]. Furthermore, all carbides and particles need to be dissolved as well as allowing the segregated elements to even out in the matrix [5].

At high austenitizing temperatures, the diffusion of the carbon is faster, the concentration of impurity elements at the austenite grain boundaries is lower leading to a reduction of segregations, but the austenite grain is larger leading to a coarse acicular ferrite structure [1]. Thus, when the austenitizing temperature increases, the amount of retained austenite and the carbon content of the austenite increase, which is favourable for the toughness properties and for increasing its hardenability, but making transformation during austempering more problematic and potentially reducing mechanical properties after austempering (the higher carbon austenite requires a longer time to transform to ausferrite) [5, 6]. On the other hand, a too low austenitizing temperature should cause an incomplete austenitization and may affect the mechanical properties, by the presence of cell boundary cementite/carbide [5, 11]. Therefore, it is necessary to select a high enough temperature to obtain a homogeneous austenitic matrix, to minimize the enrichment of impurity elements at the grain boundaries and to increase the carbon content of the austenite in order to improve the toughness properties, but also not too high temperature to reduce the mechanical properties after austempering [5, 6].

The austenitization time should be long enough to ensure the heat of the entire part to the desired austenitization temperature to obtain the stability of the retained austenite through the saturation of the austenite with the equilibrium level of carbon, (typically about 1.1-1.3%) [5, 6]. Furthermore, the austenitization time should be as short as possible in order to avoid grain growth, but long enough to eliminate the risk of cementite phase in the austenite [5]. In addition to the casting section size and type, the austenitization time is affected by the chemical composition, the austenitization temperature and the nodule count [5, 11].

The Quenching process

The quenching is the stage of heat treatment cycle of ADI where the casting is quenched from the austenitization temperature to the austempering temperature, where the isothermal transformation is carried out.

The cooling rate must be controlled to avoid formation of pearlite around the carbon nodules, which would reduce mechanical properties [11]. Usually quench time must be controlled within a few seconds to avoid the pearlite nose in the isothermal transformation diagram (Figure 3.4). Furthermore, the casting must not be quenched to temperatures below the point of martensite formation (M_s) [4, 5, 11].

Austempering is fully effective only when the cooling rate of the quenching apparatus is sufficient for the section size and hardenability of the component [4,11].

There are several critical aspects which must be controlled: transfer time from the austenitizing environment to the austempering environment, quench severity of the austempering bath, maximum section size and type of casting being quenched, hardenability of the castings [11].

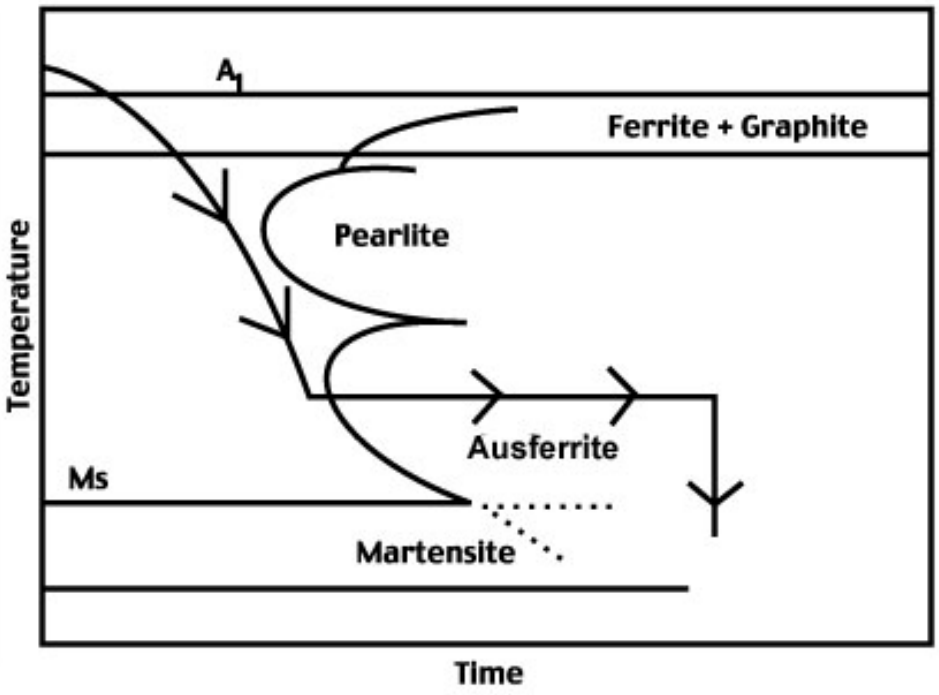

Figure 3.4: isothermal transformation diagram for an ADI alloy, courtesy of J. Hidalgo.

Therefore, from the point of view of optimum mechanical properties, it is desirable that in the austempering heat treatment of ductile iron the structure over the whole cross-section of the casting should consist of acicular ferrite and retained austenite, in which no pearlite and proeutectoid ferrite occur [1]. For this purpose it is possible to evaluate the critical bar diameter (D_c) for a particular composition of ADI or adjust the chemical composition to avoid segregation during quenching for a particular bar diameter. The critical bar diameter is a measure of the “austemperability” of ADI, and it is referred to the ability to cool a

ductile iron rapidly enough to form ausferrite and thereby avoid eutectoid (stable and metastable) transformation. The value of critical austempering diameter D_c give cooling conditions that guarantee a matrix structure with 99% ausferrite matrix in the centre of cylinder [1]. There are several regressions functions that can be used to calculate the critical bar diameter, one proposed by Voigt and Lopper [24] is:

$$D_c = 124(\%C_\gamma) + 27(\%Si) + 22(\%Mn) + 16(\%Ni) - 25(\%Mo) - 1.68 \cdot 10^4 * T^2 + 12(\%Cu \cdot \%Ni) + 62(\%Cu \cdot \%M$$

Where $\%C_\gamma$ is the carbon content of austenite after quenching, T_A the austenitizing temperature, and T is the austempering temperature. The austenite carbon content that depends on the austenitizing temperature and silicon content, can be calculated with the following equation proposed by Voigt [25]:

$$\%C_\gamma = \frac{T_A}{420} - 0.17(\%Si) - 0.95$$

The quenching process may take place in various media. The most common media used is molten salt (nitrate) bath, because it allows rapid and efficient heat transfer with a uniform low viscosity over the austempering temperature range. Moreover, it remains stable during the process and dissolves easily in water which is positive for subsequent removing and cleaning operations [28]. The disadvantage of this media is that it pollutes the environment, in a way that is comparable to a fertilizer.

Water is another media could be used: it is inexpensive, readily available and seldom contaminated but it isn't advised as the resulting rapid cooling rates increases the risk of vapour entrapment [29]. Another issue is that water is present only as steam over a temperature of 100 °C.

The other possibilities are oil and gas quenching. Oil is seldom used because its chemical instability limits its applications below 245 °C [28] but, despite of this disadvantage, oil is preferred as a quenching medium to minimize stresses [30].

Gas quenching is used to provide a cooling rate faster than that obtained in still air and slower than that for oil, where the cooling rate can be adjusted and controlled by factors

like pressure and gas type [29]. However, as high pressures are required to adequately quench the parts, gas quenching is only feasible for smaller parts.

The Austempering process

The austempering step, where the ausferrite transformation occurs isothermally, is the stage that determines the final microstructure of the casting. Austempering time and temperature must be controlled to obtain the desired microstructure in order to have optimum mechanical properties.

As described above, during austempering, a two-stage phase transformation reaction takes place. In the first stage, austenite (γ) decomposes into ferrite (α) and high carbon content or untransformed austenite (γ_{HC}). In the second stage the high carbon austenite (γ_{HC}) decomposes into ferrite (α) and ε-carbide:

1st reaction: $\gamma \rightarrow \alpha + \gamma_{HC}$

2nd reaction: $\gamma_{HC} \rightarrow \alpha + \varepsilon$

The presence of ε-carbide due to the too long holding time at austempering temperature must be avoided because resulting in the embrittlement of the matrix.

In order to obtain the best mechanical properties in ADI the process must be carried out after the completion of the first reaction but before the onset of the second reaction. This time interval between the completion of the first reaction and the onset of the second reaction is known as the process window. The process window could be modified by addition of alloying elements, so the process also depend on the chemical composition of the casting [1, 4, 5].

Austempering temperature is one of the major determinants of the mechanical properties of ADI castings [6]. To produce ADI with lower strength and hardness but higher elongation and fracture toughness, a higher austempering temperature (350-400 °C) should be selected to produce a coarse ausferrite matrix with higher amounts of carbon stabilized austenite (20-40%) [6]. Instead, to produce ADI with higher strength and greater wear resistance, but lower fracture toughness, austempering temperatures below 350 °C should be used (Figures 3.5 and 3.6) [6].

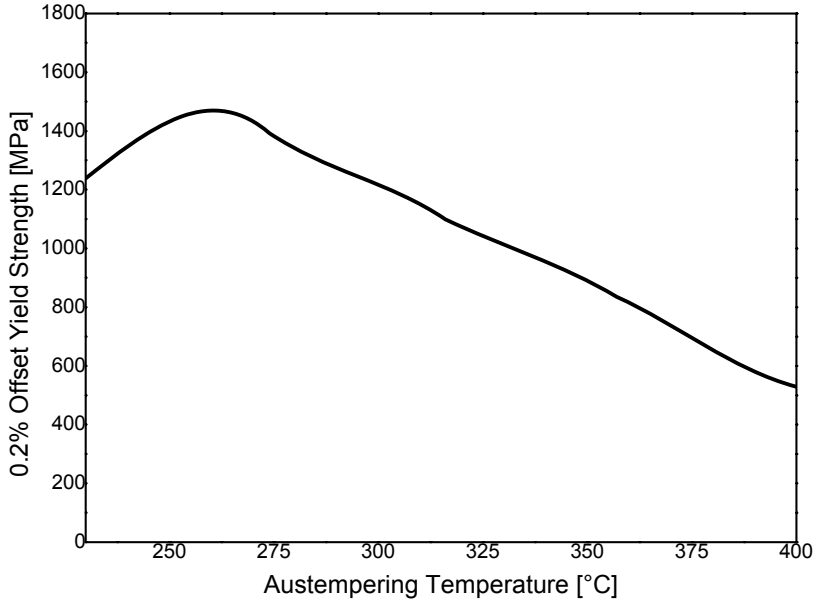

Figure 3.5: ADI yield strength vs. austempering temperature, adapted from [6].

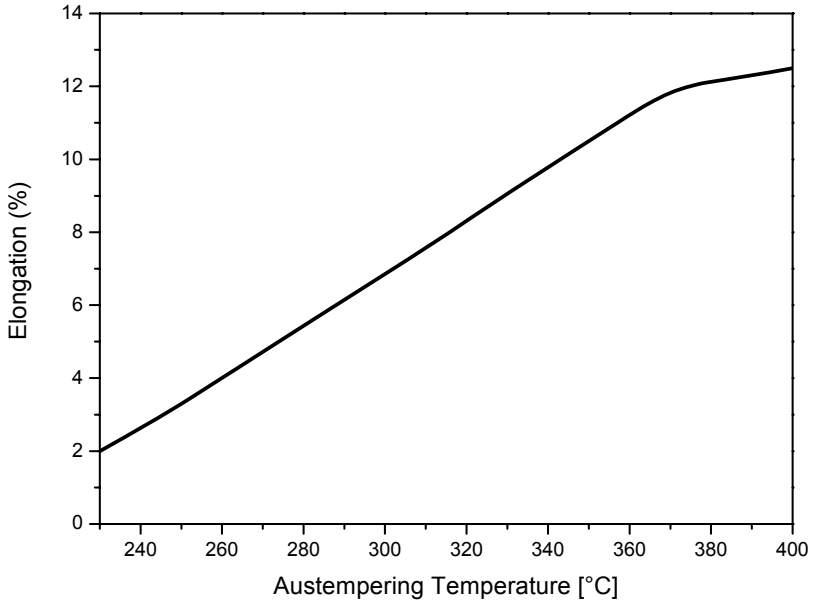

Figure 3.6: ADI elongation vs. austempering temperature, adapted from [6].

Once the austempering temperature has been selected, the austempering time must be chosen to optimize properties through the formation of a stable structure of ausferrite [6]. At short austempering times, there is insufficient diffusion of carbon to the austenite to stabilize it, and martensite may form during cooling to room temperature. The resultant microstructure would have a higher hardness but lower ductility and fracture toughness (especially at low temperatures) [6]. The minimum time required for a given austempering temperature is defined by the presence in the final microstructure of ADI of no more than 3% martensite [26]. Excessive austempering times can result in the decomposition of

ausferrite into ferrite and carbide (bainite) which will exhibit lower strength, ductility and fracture toughness (Figure 3.7) [6].

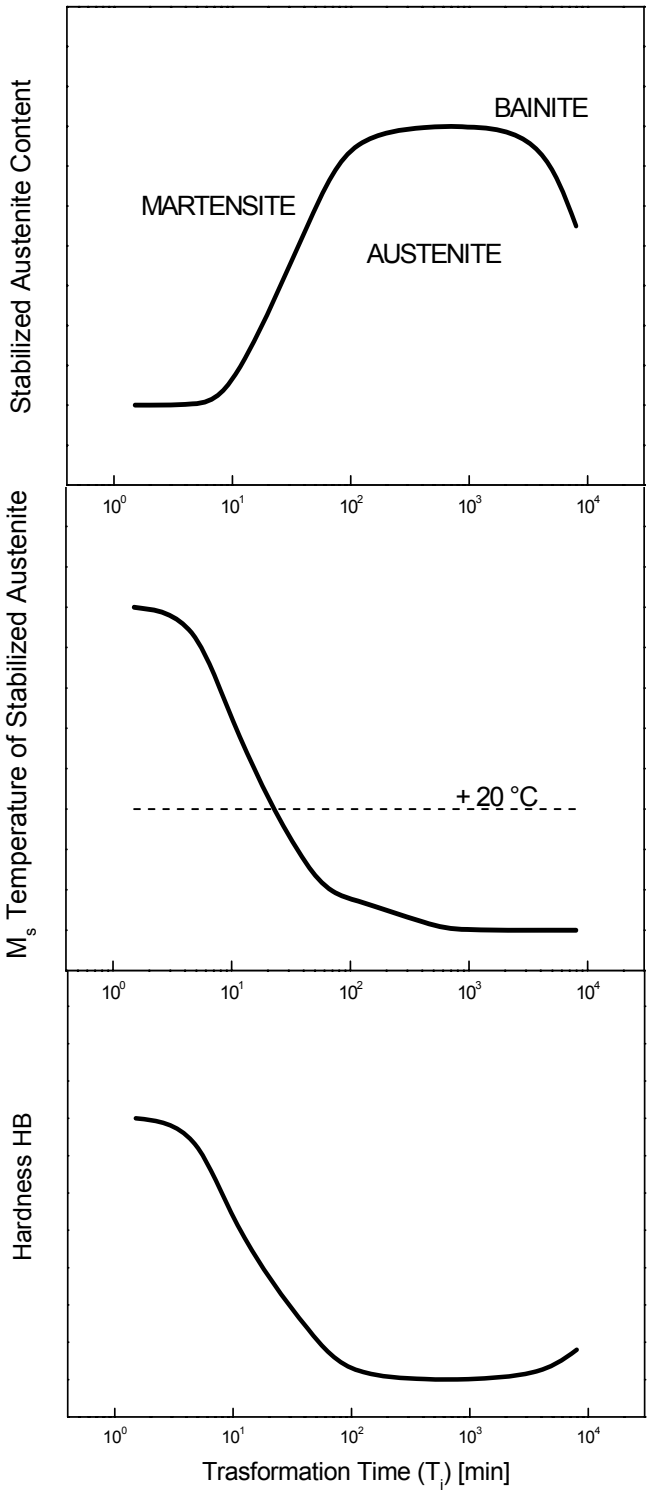

Figure 3.7: schematic diagram showing the effect of austempering time on the amount and stability of austenite and the hardness of ADI, adapted from [6].

The Cooling process

By the end of austempering step, the desired ADI ausferrite structure has developed and thus the casting is ready to cool down. The final cooling is an important stage as other steps such as austempering conditions or chemical composition. Usually the specimen was air cooled to room temperature because it is the most economical way [1]. The reason because caution has to be paid in this step is to maintain the correct microstructure obtained in the previous stages to room temperature without contaminate it.

3.3. Influence of heat treatment on properties of Austempered Ductile Iron

The microstructure and mechanical properties of ADI can be greatly altered by suitable heat treatment process. Therefore the influence of the austempering heat treatment on the various characteristics of ADI was studied by Putatunda et al. [21] for ADI alloyed with nickel, copper, molybdenum (chemical composition in table 3.1), so the results presented below have to be considered in regard to the chemical composition of iron.

Element	C	Si	Mn	S	P	Mg	Cu	Ni	Mo
Percentage	3.5	2.6	0.4	0.01	0.02	0.03	0.6	1.6	0.3

Table 3.1: chemical composition (%wt) of ductile iron of Putatunda et al. study [21], adapted from [21].

Microstructure

Both austempering time and temperature considerably influence the microstructure of ADI. At shorter austempering times, an appreciable proportion of martensite was observed [21]. The austempering time is insufficient to build up the carbon content of austenite to a level where it is stabilized on quenching. Austenite regions close to the ferrite will become enriched with carbon and stabilize, while those away from ferrite needles do not [21]. Furthermore, there were more bainitic ferrite needles around the graphite nodules and fewer away from them. This is so because transformation starts near the graphite nodules, which are potent nucleation sites for ferrite initiation, and progresses toward the prior austenite grain boundaries [21]. The prior austenite grain boundary regions were mostly free of ferrite and could therefore be assumed to be essentially martensitic. When the austempering time was increased, considerably less martensite was observed, indicating

that bainitic transformation had progressed to a greater extent. At long austempering times, no martensite was observed [21].

At low austempering temperatures, due to high supercooling, a high nucleation rate results in a large number of fine ferrite needles [21]. On the other hand, at higher temperatures, the lower nucleation rate results in fewer ferrite needles, each growing to a larger size. As the temperature was raised, the amount of austenite increased.
In fact, increasing the austempering temperature, resulted in the coarsening of the acicular ferrite as well as an increase in the austenite content [21].

Another important microstructural feature is the carbon content of austenite. At the lowest temperature, it is found that the carbon content rises steadily with austempering time. At this low temperature, the diffusion rate of carbon is low, and the kinetics of ferrite formation is fast [21]. Therefore, as ferrite forms, there will be an initial buildup of carbon at the ferrite/austenite interface. Selecting longer holding times, this carbon may gradually diffuse into austenite, increasing its carbon content. It should be noted that there is no change in volume fraction of austenite [21]. Therefore, carbon buildup is not due to the formation of more ferrite and consequent rejection of carbon into the surrounding austenite [21].

At higher temperatures, faster diffusion rates promote faster buildup of carbon in austenite, as shown by the rapid increase of carbon content with austempering time. After longer austempering times, carbon content reaches a saturation value [21]. It should be noted that the volume fraction of austenite also reached a saturation value around this time. The saturation value increases with decreasing temperature. This is to be expected as the γ/γ + α phase boundary shifts to a higher carbon content of austenite in equilibrium with ferrite increases with decreasing temperature [21].

The carbon content of retained austenite increases initially, reaches a maximum, and drops at higher temperatures [21]. At low temperatures, low diffusion rates and fast kinetics of ferrite formation, means that little carbon diffuses into the austenite. Hence, the carbon content will be low at lower temperatures [21]. As the temperature rises, more carbon will find its way into the surrounding austenite from regions transforming to ferrite due to higher diffusion rates as well as slower kinetics of ferrite formation at decreasing supercooling. As the temperature is still increased, a stage will be reached when all the

carbon from the regions transforming to ferrite will diffuse into the surrounding austenite. All the carbon in the original austenite at the austenitizing temperature (C_0) will now be in the retained austenite. This is the maximum amount of carbon that can find its way into retained austenite. The product $X_\gamma C_\gamma$(where X_γ is the volume fraction of retained austenite and C_γ is the carbon content of the retained austenite) , which gives the total carbon in the retained austenite, will then have the maximum value and will be equal to C_0. Beyond this temperature, as X_γ increases, C_γ will decrease [21]. Thus, while at lower temperatures insufficient carbon is reaching the retained austenite, at higher temperatures, no more carbon is available to enrich the austenite. The optimum is reached at an intermediate temperature, where the carbon content of austenite will be a maximum [21].

Tensile properties

Low ductility and strength at short austempering times can be attributed to the embrittling effect due to the presence of martensite at prior austenite grain boundaries [21]. Yield strength is found to be more sensitive to the austempering time than the tensile strength. Martensite content decreases as the austempering time increases [21]. Therefore, strength and ductility increase with increasing time, reaching a plateau after some length of time. This duration also correspond to the time for attaining maximum retained austenite content [21].

Both yield strength and tensile strength decrease steadily with rising austempering temperature. With increasing temperature, bainitic ferrite becomes coarser and the amount of retained austenite increases. Both these factors lead to a drop in strength but an increase in ductility [21] (Figure 3.8).

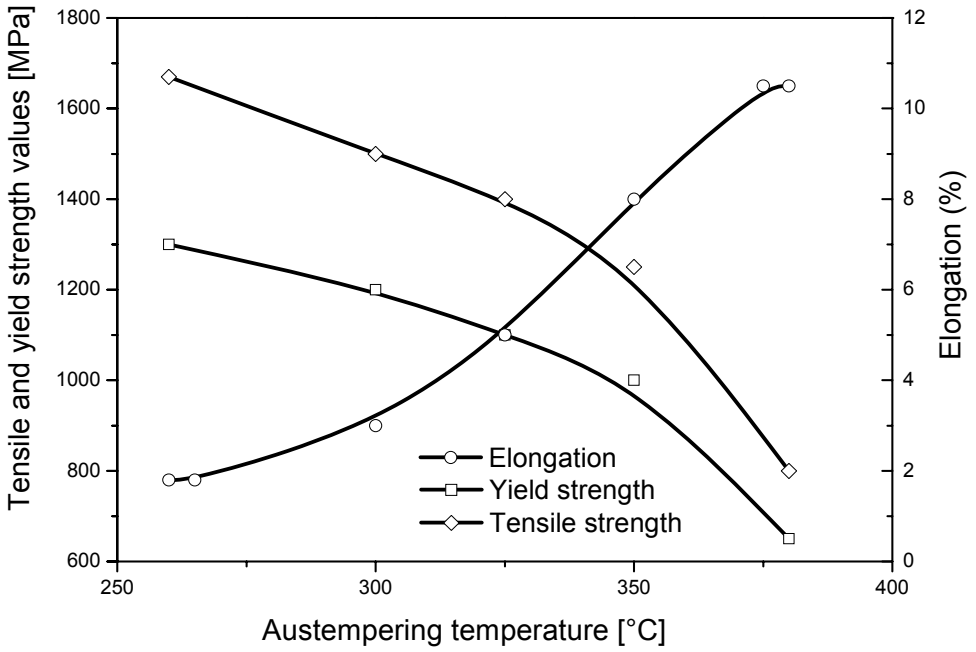

Figure 3.8: influence of austempering temperature on the tensile properties, adapted from [21].

It has to be observed that the tensile properties of this grade of ADI [21] have to be considered in regard to the chemical composition of iron. In fact, because of the high percentage of alloy elements, carbides precipitation can occurs and strongly affect the mechanical properties of ADI.

Fracture toughness

Similar to the tensile properties, the results about fracture toughness [21] have to be analyzed in terms of the chemical composition of iron.

At all austempering temperatures, fracture toughness was found to be considerably influenced by austempering time [21]. The fracture toughness of ADI increased with rising austempering time until a certain length of time. Beyond that time there was practically no change in fracture toughness.

The low values at short times can be attributed to the presence of brittle martensite at cell boundaries. With increasing austempering time, as the austenite content increases, fracture toughness improves [21].

At a given austempering time, fracture toughness was found to initially increase with increasing temperature, and thereafter decrease with a further increase in temperature

[21] (Figure 3.9). The microstructure can be said to have a profound effect on the fracture toughness. A lower bainitic structure with fine acicular ferrite imparts better fracture toughness than an upper bainitic structure with coarse feathery bainitic ferrite [21].

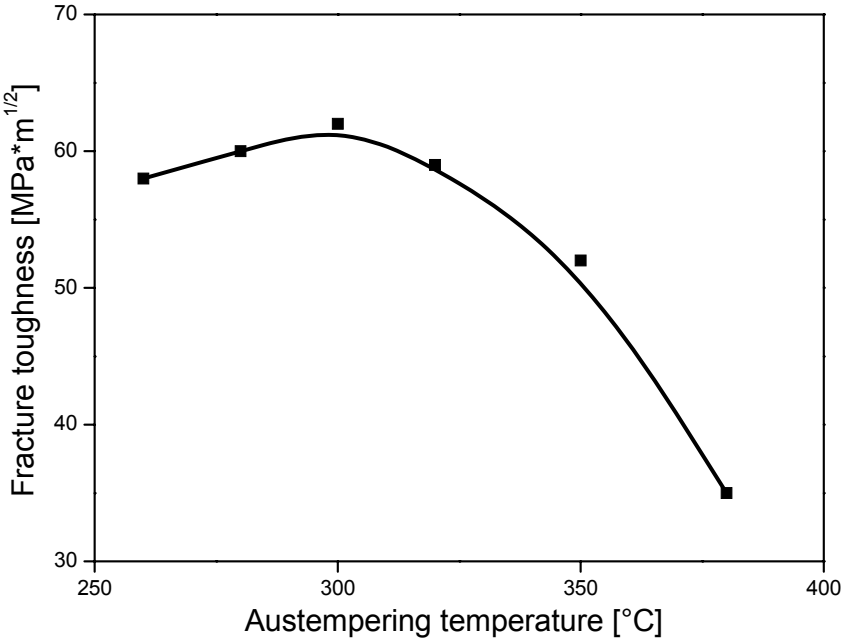

Figure 3.9: influence of austempering temperature on fracture toughness, adapted from [21].

Some of microstructural features that influence mechanical properties of ADI can be listed as follows: morphology of bainitic ferrite (whether acicular or feathery), amount of retained austenite, carbon content of retained austenite, carbide dispersion within austenite or at austenite/ferrite interface, and dislocation density [21].

Out of these, the retained austenite content is generally regarded as the most important microstructural feature. The excellent properties of ADI such as good ductility at comparatively high strength levels, excellent wear resistance, and superior fatigue properties are believed to be the result of the ability of retained austenite to strain harden or to transform to martensite when worked [21].

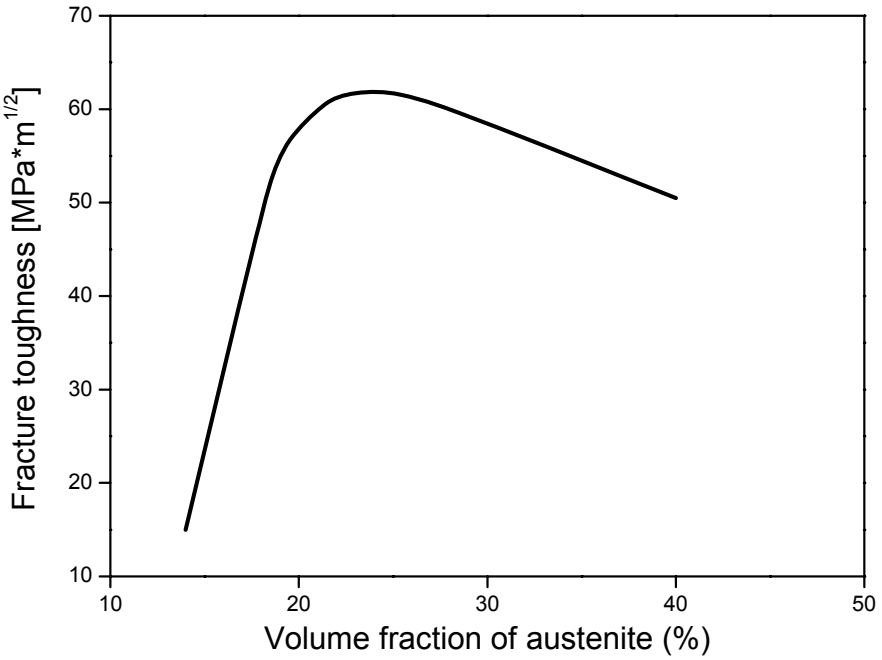

Figure 3.10: influence of austenite content on fracture toughness, adapted from [21].

There is an unmistakable trend of rising fracture toughness with increasing austenite content, up to a certain high volume fraction with a drop thereafter [21] (Figure 3.10).
Further, some martensite is to be expected due to unstabilized austenite. The presence of this brittle phase along the prior austenite grain boundaries can initiate crack and also provide a preferential path for crack propagation [21].
In the absence of this, fracture behaviour is primarily controlled by austenite, as it is the tougher of the two phases present in the microstructure. Hence, an increasing amount of retained austenite can result in an increasingly tougher material with consequential improvement in fracture toughness [21].

The drop in fracture toughness beyond a certain high volume fraction of retained austenite should be attributed to the change in morphology of ferrite rather than solely to the amount of austenite [21]. Austenite contents in excess of a certain volume percent are obtained only when austempering at temperatures higher than 350 °C [21]. At these temperatures, broad ferrite blades are formed which are free of carbides. At low temperatures, fine acicular ferrite having heavy dislocation density and fine dispersion of carbides is formed [21]. In addition, it has been shown that crack initiation in ADI starts with decohesion of graphite/matrix interface. This raises the stress concentration in the matrix around the graphite nodules. As a result, extensive plastic deformation occurs in the matrix, which is

confined to the ferrite, leading to the formation of microcracks in the ferrite or at the ferrite/austenite interface [21]. The width of the ferrite plate plays an important role in crack propagation across the austenite regions. As plastic deformation takes place in ferrite, dislocation pileups will form within ferrite at the interface. There will be a high stress concentration at the head of the pileup which, if sufficiently large, can initiate a crack within austenite. When austempered at higher temperatures, the ferrite blade width will be large, dislocation pileup will be large, and crack initiation will be easy [21].

A point worth considering at this stage is the possibility of stress-induced martensite formation, which may provide an easy fracture path, leading to lower fracture toughness. Because of high carbon content, the M_s temperature is very low, and the austenite is generally highly stable [21]. On the other hand, austenite formed at higher temperatures has lower carbon content and, therefore, lower stability. Martensite formation may be easier in these, as compared to those austempered at lower temperatures. Thus, formation of stress-induced martensite may be one of the reasons for the lower facture toughness of ADI with upper bainitic microstructure [21].

Increasing the toughness of retained austenite in the microstructure can also lead to increased fracture toughness of the ductile iron as a whole [21]. Increasing carbon content of austenite will increase its toughness, as it will result in greater interaction between dislocation and carbon atoms. It can be seen that fracture toughness rises with carbon content of austenite (Figure 3.11). Thus, a high carbon content of the retained austenite is very important in increasing the fracture toughness [21].

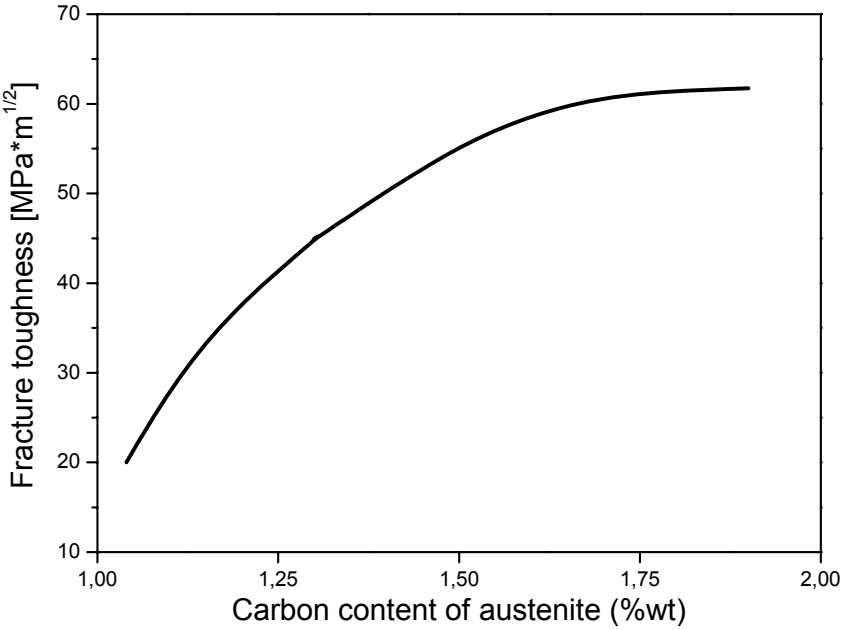

Figure 3.11: influence of carbon content of austenite after quenching on fracture toughness, adapted from [21].

The low carbon content may be one of the contributing factors to the low fracture toughness at higher temperatures, besides the morphology of ferrite [21].

Since carbon content of the retained austenite obviously has an important influence on the fracture toughness, it is worthwhile to consider another related factor, namely, the austenitizing temperature [21]. Increasing the austenitizing temperature will increase the initial carbon content of the austenite. This will increase the carbon content of the bainitic retained austenite at a given austempering temperature and time. Therefore, increasing the austenitizing temperature should have a beneficial effect on fracture toughness [21]. However, a large increase in austenitizing temperature may be found counterproductive. This can be attributed to the embrittlement of grain boundaries by phosphorus [21]. The experimental data indicated that phosphorus was liberated at a higher austenitizing temperature by partial decomposition of precipitates rich in magnesium and phosphorus [21]. Coarsening of the austenite grains may also be an important factor in the deterioration of fracture toughness at high austenitizing temperatures [21].

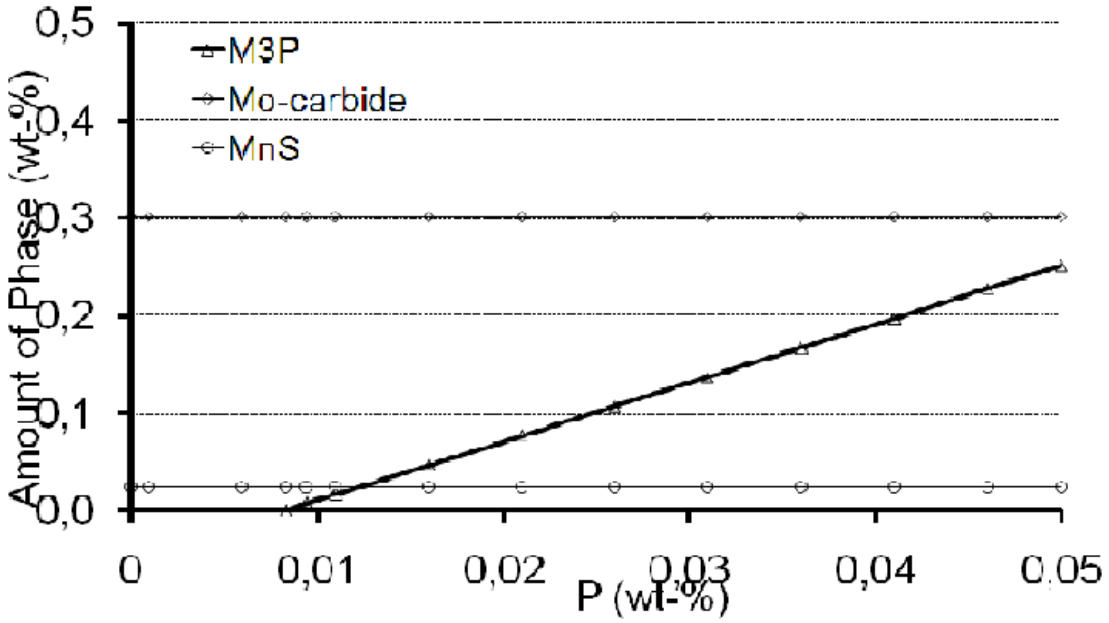

Figure 3.12: simulation of embrittlement of grain boundaries by phosphorus, courtesy of Henrik Borgström.

In Figure 3.12 it can be seen a Thermo calc model predicts the amount of iron-rich phosphide formed with varying phosphorus concentration for 900 grade ADI at 360 °C.

4. INFLUENCE OF MICROSTRUCTURE ON THE IMPACT PROPERTIES OF AUSTEMPERED DUCTILE IRON

4.1. Effect of austenitization conditions on impact properties of Austempered Ductile Iron

Grech et al. [38] investigated about the effect of austenitization conditions on the impact properties of an alloyed Austempered Ductile Iron with an initial ferritic matrix structure (containing 1.6% Cu and 1.6% Ni as the main alloying elements, the chemical composition is listed in table 4.1), more impact tests were carried out on samples of initial ferritic matrix structure and which had been austenitized at 850, 900, 950, and 1000 °C for 15 to 360 min and austempered at 360 °C for 180 min. The results showed that the austenitization temperature and time have significant effect on the impact properties of the alloy, which was attributed to the carbon kinetics [38].

Element	C	Si	Mn	S	P	Mg	Ni	Cu
Percentage	3.3	2.6	0.35	0.008	0.01	0.04	1.6	1.6

Table 4.1: chemical composition (%wt) of ductile iron of Grech et al. study [38], adapted from [38].

In a nodular iron with an as-cast pearlitic structure, the graphite spheroids and pearlite both contribute to the carbon enrichment of the austenite [42]. In a fully ferritic matrix structure, the graphite nodules are the only source of carbon, and consequently, the carbon diffusion distances involved during solution treatment may be relatively large [38]. However, some carbon can be attained from the small quantities of spheroidized carbides present. Consequently, full austenitization requires either very long solution treatment cycles or a very high carbon diffusion rate, which in turn, calls for higher austenitization temperatures [38].

At 850 °C, complete austenitization is difficult to achieve: the carbon mobility is rather slow, and the soaking time selected is not sufficient for complete austenitization to take place [38]. In fact, irons austenitized for up to 180 minutes still contain pro-eutectoid ferrite in the austempered structure [38]. The samples austenitized at 900 and 950 °C contain

acicular ferrite surrounded by high carbon austenite. The absence of pro-eutectoid ferrite and martensite can respectively be attributed to full austenitization and to the resulting stable high carbon austenite [38]. Increasing austenitization temperature increases the percentage of carbon dissolved in the original austenite, which in turn, decreases the free energy controlling the transformation of austenite to ferrite and high carbon austenite. The driving force reduction is responsible for the decrease in the number of ferrite nuclei formed and the slower growth along the ferrite platelet. Therefore increasing the austenitization temperature to 1000 °C leads to structures containing a high percentage of large austenite grains. The center of these regions is low in carbon content and is therefore relatively unstable. It transforms to martensite as the specimens cool to room temperature or upon the application of mechanical stress. This has a negative influence on the impact properties, as shown in Figure 4.1.

To summarize, increasing the austenitization temperature from 850 to 1000 °C eliminates the pro-eutectoid ferrite and increases the austenite volume fraction. The latter, however, has a lower carbon content, is less stable, and may transform to martensite on cooling to room temperature or upon the application of stress.

Specimens austenitized at 850 °C have the highest impact energy value. This has been attributed to the large volume fraction of the pro-eutectoid ferrite and the morphology of the acicular ferrite [38].

Specimens solution heat treated at 900 and 950 °C have a fully austempered structure and relatively high impact energy values [38]. In contrast, specimens austenitized at 1000 °C, have generally lower impact energy values. This is attributed to the higher percentage of low carbon austenite and the associated martensite [38] (see Figure 4.1).

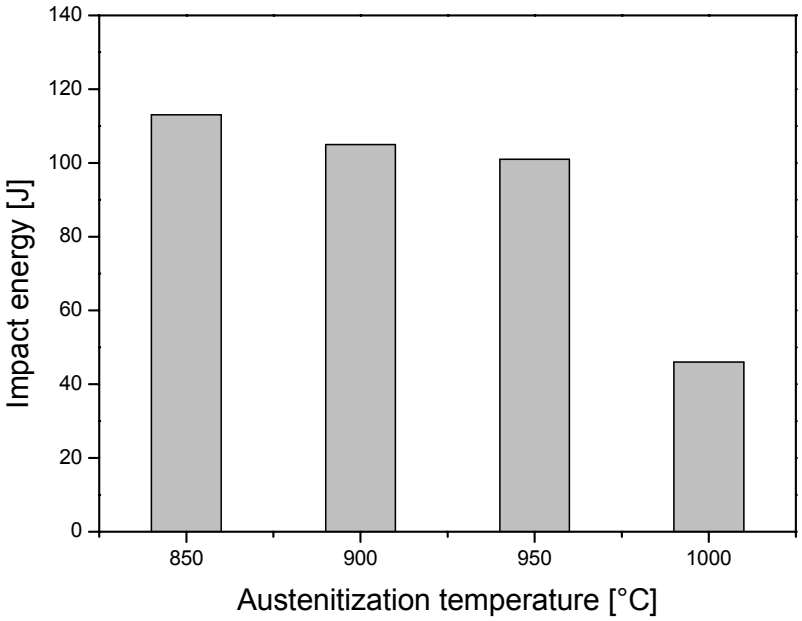

Figure 4.1: effect of austenitizing temperature on the impact properties of specimens austenitized for 180 min, adapted from [38].

The austenitizing time determines the percentage of carbon dissolved in the austenite, which in turn, affects the rate of austenite transformation during austempering and therefore, has an influence on the impact energy values attained [38].

The microstructures of samples austenitized for short periods at 850 and 900 °C contain a considerable volume of pro-eutectoid ferrite [38]. This phase is replaced by ausferrite as the soaking period extends to 360 minutes at 850 °C or to 60 minutes at 900 °C [38]. In contrast, the microstructures of specimens austenitized at 950 °C for durations between 15 and 360 min consist generally of acicular ferrite and high carbon austenite [38]. There are only marginal differences between microstructures of specimens soaked for different periods. The microstructures of samples austenitized for 15 min at 1000 °C are fully ausferritic. Increasing the soaking period to 60 min and further results in structures containing martensite [38].

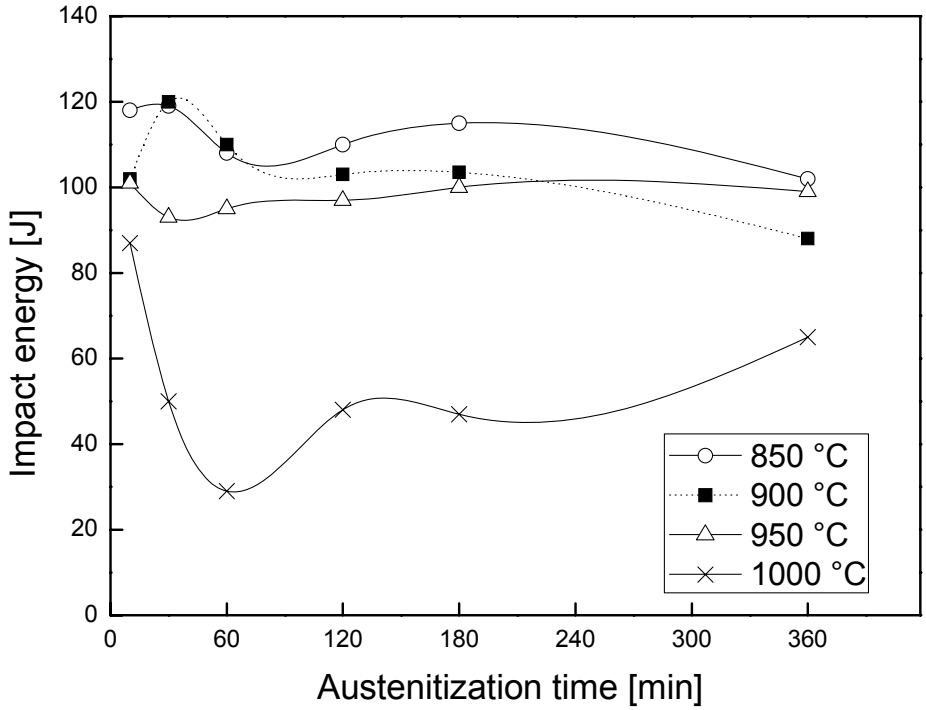

Figure 4.2: effect of austenitizing time on impact energy of specimens austenitized at 850, 900, 950, and 1000 °C, adapted from [38].

As shown in Figure 4.2, high impact properties are attained following austenitizing at 850 °C for 30 min [38]. That austenitizing temperature is insufficient for full austenitization. In fact, pro-eutectoid ferrite occurred even in samples solution treated for as long as 180 min. It is apparent that the high impact energy values are due to the pro-eutectoid ferrite and not the ausferrite [38]. Structures containing this type of ferrite would, however, have a low tensile strength compared to those with a fully ausferritic structure [38].

The impact energy values of samples solution treated at 900 °C fall as austenitization time increases to 180 min and change only marginally with further increases in the soaking time. The higher toughness values correspond to structures containing some pro-eutectoid ferrite [38]. The slightly lower impact energy values in specimens austenitized at 950 °C as compared with test samples austenitized at lower austenitization temperature can be attributed to the elimination of the pro-eutectoid ferrite phase as well as the lower rate of austenite transformation, indicating that a high austenitization temperature increases the carbon diffusion rate and leads to a rapid austenitization [38].

The toughness falls rapidly as the solution treatment time increases for samples austenitized at 1000 °C. The high impact energy values can be attributed to the low content of dissolved carbon in the austenite and, consequently, the relatively high driving force controlling the austempering reaction [38]. Increasing the soaking period to 60 min increases the dissolved carbon and results in a coarser structure containing martensite [38]. It is not clear, however, why soaking for more than 60 min gives rise to a recovery in impact energy values [38].

In conclusion, including both austenitization temperature and time parameters, it has been shown that, for the Cu-Ni alloy investigated, optimum impact energy values are attained when austenitization is carried out between 900 and 950 °C for 120 to 180 minutes [38]. These austenitization conditions are such as to eliminate the pro-eutectoid phase but at the same time do not reduce substantially the rate of austenite transformation; consequently, these optimum conditions do not promote the formation of martensite [38].

4.2. Effect of austempering conditions on impact properties of Austempered Ductile Iron

An investigation about the austempering study of properties of alloyed ductile iron [39] shows the behaviour of impact properties when the austempering conditions (time and temperature) have been changed. In that work [39], specimens austenitized in a protective argon atmosphere at 900 °C for 2 hours were rapidly transferred to a salt bath at austempering temperatures 300, 350, and 400 °C, held for 1, 2, 3 and 4 hours and then air cooled to room temperature, the chemical composition is listed in table 4.2.

Element	C	Si	S	Mn	P	Mg	Cr	Ni	Mo
Percentage	3.6	2.5	0.01	0.3	0.04	0.05	0.05	0.95	0.5

Table 4.2: chemical composition (%wt) of ductile iron of study of properties of alloyed ductile iron [39], adapted from [39].

Mechanical properties (strength, elongation and impact energy) strongly depend on amounts of acicular ferrite and retained austenite [39]. Time and temperature of isothermal transformation during austempering treatment have a marked influence on the relative amount of retained austenite (Figure 4.3) [39].

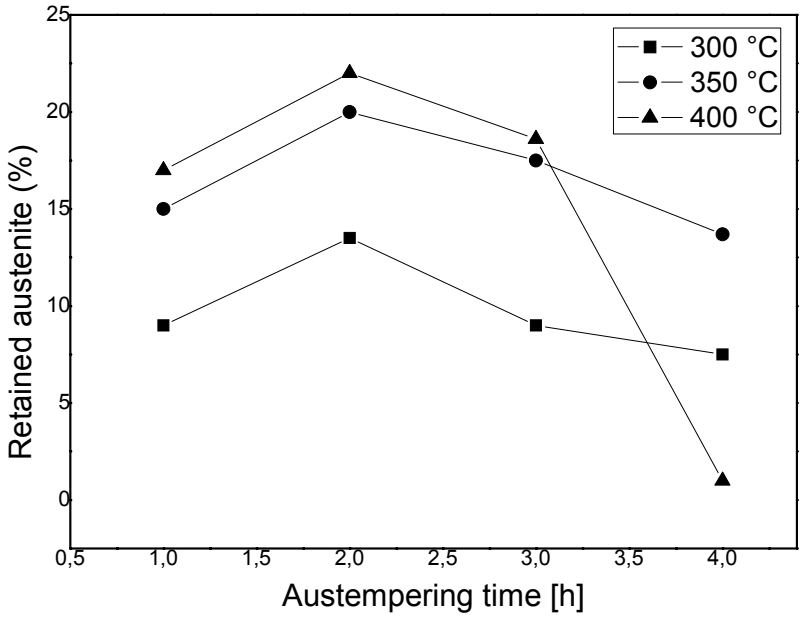

Figure 4.3: effect of austempering time on the volume fraction of retained austenite at different austempering temperatures, adapted from [39].

From the shape of curves in Figure 4.3 it is apparent that two stages are involved in the isothermal transformation, as described in the previous paragraphs. In the Stage 1 (times less than 2 h) the amount of retained austenite increases with time. This may be explained taking into account that the transformation to bainite was not completed [39]. It is well documented [40] that austenitic regions having low silicon and high carbon concentration, e.g., regions between graphite nodules, will not undergo transformation (to bainitic ferrite and retained austenite) during short time of austempering, so during the subsequent cooling from austempering to room temperature the formation of martensite cannot be prevented. With somewhat longer austempering time the amount of retained austenite increases reaching maximum after 2 h. However, after 2 h the amount of retained austenite decreases, indicating the start of the Stage 2 of austempering reaction when retained austenite decomposes to bainitic ferrite and carbide [39]. At 400 °C this decrease is more pronounced and is associated with the decomposition of austenite to ferrite and carbide [41].

Low values of impact energy (Figure 4.4) at short austempering times are connected with the significant amount of brittle fracture caused by the presence of martensite in the structure [39]. With longer time martensite disappears in the structure, whereas the amount of bainitic ferrite and retained austenite increases resulting with a maximum of

impact energy after 2 h of austempering [39]. With further increase of time a decrease in impact energy occurs. This decrease is evident especially at 400 °C: the low values of impact energy correspond to a fall of the amount of retained austenite at longer austempering time [39].

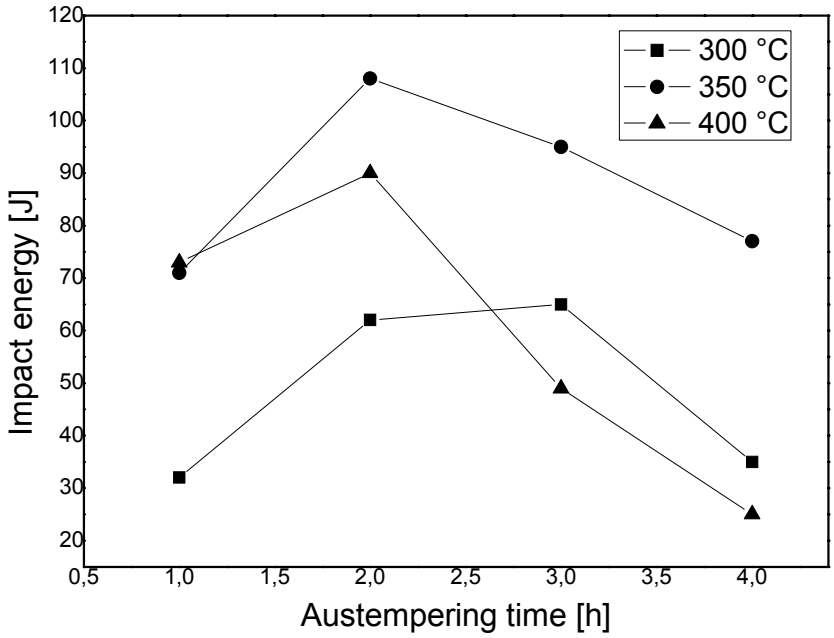

Figure 4.4: the effect of austempering time on impact energy at different austempering temperatures, adapted from [39].

The variation of impact energy after 2 h of holding at different austempering temperatures is shown in Figure 4.5. As austempering temperature increases martensite disappears from the structure and the amount of retained austenite increases [39]. These changes result in reduced strength but increase of impact energy as the amount of retained austenite increases: values of impact energy show maximum at 350 °C which coincides with the highest amount of retained austenite (see Figure 4.5) [39].

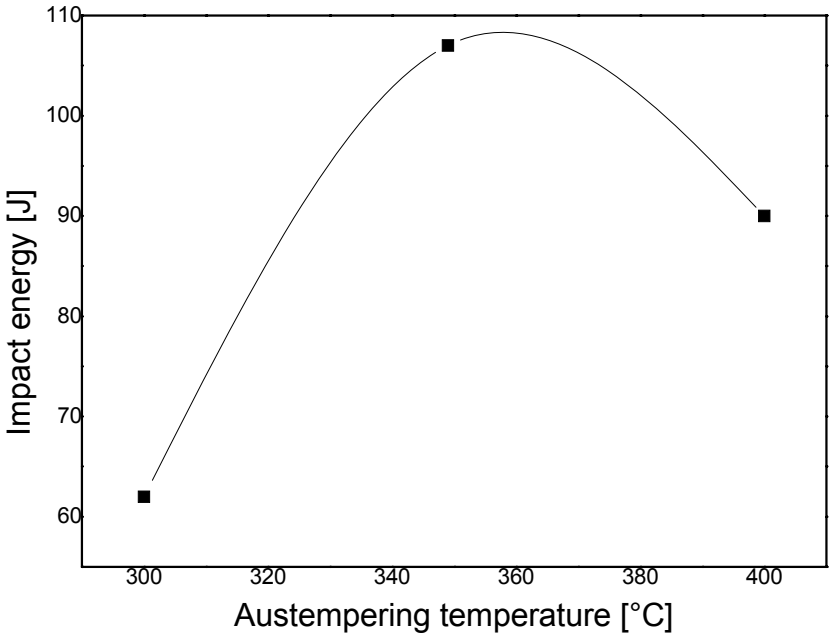

Figure 4.5: effect of austempering temperature on impact energy after 2 h of austempering, adapted from [39].

According to the results of the study the optimal processing window was established for austempering at 350 °C 2 h [39]. The obtained microstructure consisting of acicular ferrite and retained austenite yield the best combination of mechanical properties (tensile strength, elongation and impact energy) [39]. Alloying with copper improves elongation and impact energy, but decrease strength of ADI [39].

4.3. Effect of alloy elements segregation on impact properties of Austempered Ductile Iron

The effect of segregation of alloying elements on the phase transformation of ductile iron during austempering was investigated by Lin et al. [43]. Four heats, each containing 0.4%Mn, 1%Cu, 1.5%Ni, or 0.4%Mo (%wt) separately, were melted.

Segregation was found with those positive segregating elements, Mn and Mo, and those negative segregating elements, Si, Cu, and Ni [43]. The segregation of Mo is more significant than Mn. The segregation of Cu is more than Ni, and that of Ni is more than Si [43]. The ability of Cu to hinder carbon diffusion at the graphite-austenite interface during the eutectoid transformation results in pearlite being present [43]. Other alloys exhibit substantial ferrite in the as-cast structure with pearlite relegated to near the intercellular regions [43].

Between the time of finishing the first stage and beginning the second stage of bainite reaction in ductile irons, there is a significant “processing window” for austempering to obtain optimum mechanical properties [43]. The austempering temperature is a critical factor affecting the processing window, which is relatively narrow for austempering of 400 °C (falling within approximately 10^3 to $5x10^3$ seconds) but wider at 350 °C (approximately $2x10^3$ to 10^5 seconds) [43].
The microsegregation of alloying elements leads to a reduction in the processing window. The greater the degree of segregation, the less will be the span of the processing window [43]. Due to this ratio, the difficulty of controlling the process of austempering of ductile irons is increased.

Impact toughness is significantly affected by the segregation [43]. The impact strength for the specimens with less segregation is greater than for those with greater segregation [43]. The microstructures of Ni, Cu, and Mn alloys in each austempered condition show completion of the first stage of bainite reaction, and the impact values of these three alloys in the same diameter are not significantly different [43].
Mo has the most extreme segregating tendency of all alloying elements in this study, and it retards the bainite reaction and causes microshrinkage porosity in the intercellular regions. Consequently, the Mo-alloyed irons austempered at 350 °C and 400 °C have the lowest impact strength among all alloys [43].

5. INFLUENCE OF MICROSTRUCTURE ON THE FATIGUE PROPERTIES OF AUSTEMPERED DUCTILE IRON

Many different mechanical failure modes exist in all fields of engineering. These failures can occur in simple, complex, inexpensive, or expensive components or structures. Failure due to fatigue is multidisciplinary and is the most common cause of mechanical failure. Even though the number of mechanical failures compared to successes is minimal, the cost in lives, injuries, and dollars is too large [33]. Proper fatigue design includes synthesis, analysis and testing are to the real product and its usage, the greater confidence in the engineering results.
Applicable fatigue behaviour and fatigue design principles have been formulated for nearly 150 years since the time of Wöhler's early work [33]. These principles have been developed, used, and tested by engineers and scientists in all disciplines and in many countries.

The term "fatigue" refers to gradual degradation and eventual failure that occur under loads which vary with time, and which are, most of the time, lower than the yield strength of the specimen, component or structure concerned [31]. These loads are cycling in nature, but the cycles are not necessarily all of the same size or clearly discernible. A fatigue load in which individual cycles can be distinguished is usually called a cyclic load [31].

If a specimen is subjected to a cyclic load, a fatigue crack nucleus can be initiated on a microscopically small scale, followed by crack growth to a macroscopic size, and finally specimen failure in the last cycle of the fatigue life [32].
Understanding of the fatigue mechanism is essential for considering various technical conditions which affect fatigue life and fatigue crack growth, such as the material surface quality, residual stress, and environmental influence. This knowledge is essential for the analysis of fatigue properties of an engineering structure. Fatigue prediction methods can only be evaluated if fatigue is understood as a crack initiation process followed by a crack growth period [32].
The fatigue life is usually split into a *crack initiation period* and a *crack growth period* [32]. The initiation period is supposed to include formation of microcrack and microcrack growth, but the fatigue cracks are still too small to be visible by the unaided eye. In the

second period, the crack is growing until complete failure. It is technically significant to consider the crack initiation and crack growth periods separately because several practical conditions have a large influence on the crack initiation period, but a limited influence or no influence at all on the crack growth period [32].

A *constant amplitude fatigue loading* (or *constant amplitude loading*) is a fatigue loading in which all the load cycles are identical [31] (Figure 5.1). A cycle is the smallest unit of the stress history which repeat exactly. Cycles are often, but not always, sinusoidal [31].
There are several symbols in the fatigue theory: σ_a is the amplitude, σ_m is the mean stress, σ_{max} is the maximum stress in the load cycle, σ_{min} is the minimum stress in the load cycle. Mathematically a load cycle (or stress cycle) is expressed as $\sigma_m \pm \sigma_a$. Compressive stesses are taken as negative.

$$\sigma_{max} = \sigma_m + \sigma_a$$

$$\sigma_{min} = \sigma_m - \sigma_a$$

$$\sigma_m = \frac{\sigma_{max} + \sigma_{min}}{2}$$

The stress range is $S = 2\sigma a = \sigma_{max} - \sigma_{min}$, and the stress ratio, $R = \sigma_{min}/\sigma_{max}$.

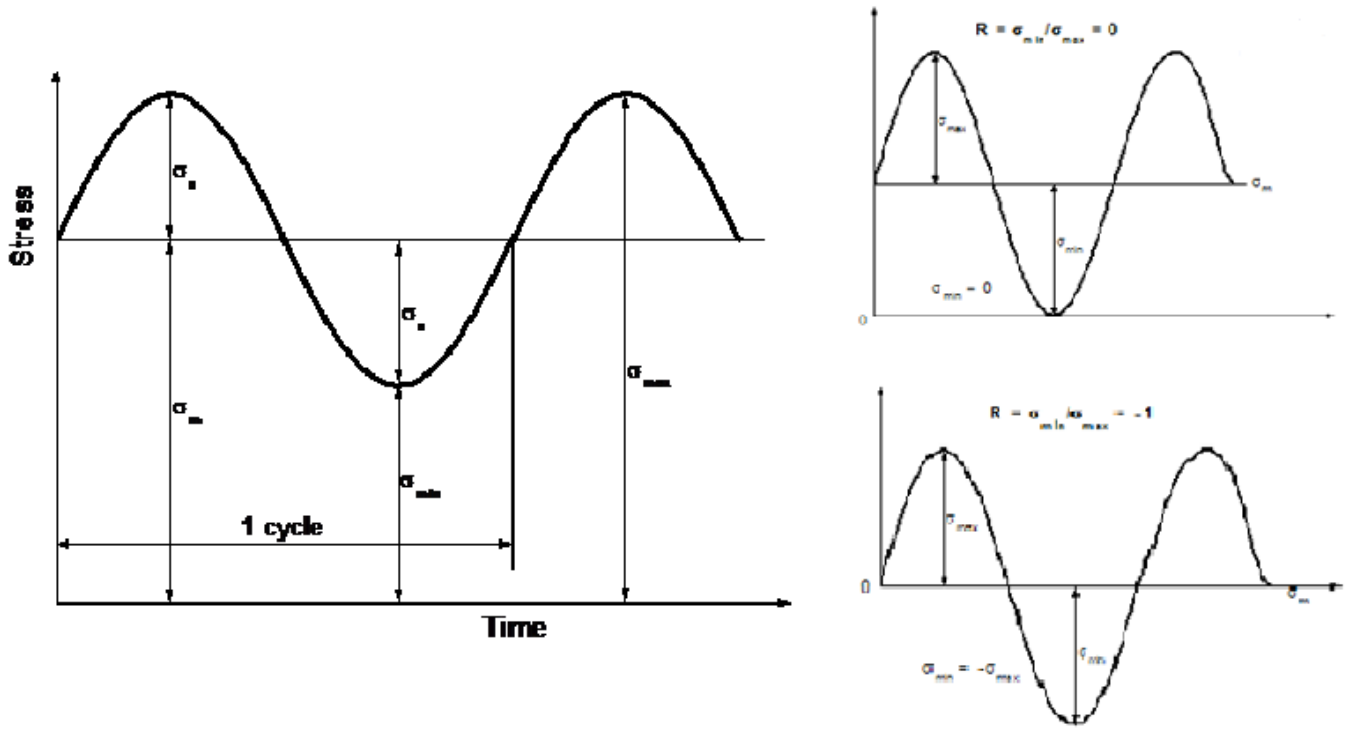

Figure 5.1: notation for constant amplitude fatigue loading, adapted from [31].

Conventionally, results are presented as S/N curves (Figure 5.2). These are plots of *Alternating stress* versus *Number of cycles* to failure, with an appropriate curve fitted through the individual data points (sometimes, stress range is used) [31]. Failure is usually defined as the separation of a specimen into two parts, but other definitions are sometimes used. For example, loss of a specified amount of stiffness or the appearance of a crack of a specified size. S/N curves are sometimes called Wöhler curves [31]. The number of cycles to failure is sometimes called the life or the endurance. It is usually plotted on a logarithmic scale, but alternating stress may be plotted on either a linear or a logarithmic scale [31]. As used to be conventional (Frost et al. 1974) these S/N curves are for endurances of less than 10^8 cycles. The region where failure takes place in less than about 10^4 cycles is called *low cycle fatigue*, and the region for longer endurances *high cycle fatigue* [31]. In some cases the tests were stopped before 10^8 cycles, when the specimens were still unbroken, and suggested that the line through the points in the S/N curves became horizontal. When it occurs, the stress corresponding to the horizontal line is called the *fatigue limit* [31].

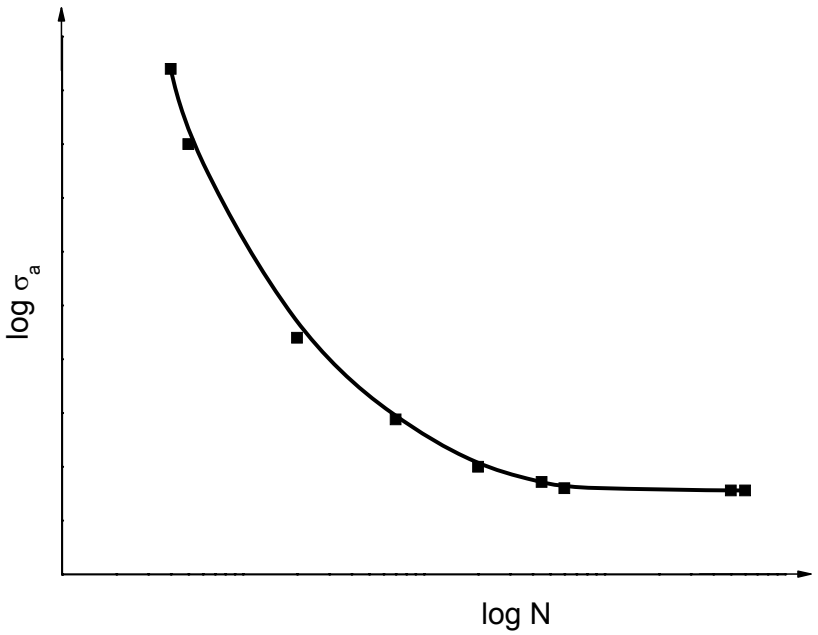

Figure 5.2: typical S/N curve, adapted from [31].

Crack surface surfaces are stress-free boundaries adjacent to the crack tip and therefore dominate the distribution of stresses in that area [31]. Remote boundaries and loading forces affect only the intensity of the stress field at the crack tip [31]. These fields can be divided into three types corresponding to the three basic modes of crack surface

displacement, and are conventionally characterized by the stress intensity factor *K* (with subscript I, II, III to denote the mode) [31]. *K* has the dimensions (stress) x (length)$^{1/2}$ and is a function of the specimen dimensions and loading conditions [31]. Conventionally, K is expressed in MPa m$^{1/2}$ [31]. In general, the opening mode (I) intensity factor is given by [31]:

$$K_I = \sigma (\pi a)^{\frac{1}{2}} \alpha$$

where σ is the tensile stress perpendicular to the crack, a is the crack length and α is a factor, of the order of unity, which depends on geometry and loading conditions [31].

In the analysis of fatigue crack growth data, the fatigue cycle is usually described by $\Delta K = (K_{max} - K_{min})$, where K_{max} and K_{min} are the maximum and the minimum values of K_I during the fatigue cycle [31]. It has been shown that ΔK rather that K_{max} has the major influence on fatigue crack growth and that, if ΔK is constant, the fatigue crack growth rate is constant [31]. For many materials, subjected to tensile loading cycle, the rate of fatigue crack growth can be expressed by the equation [31], also known as Paris law:

$$\frac{da}{dN} = C(\Delta K)^m$$

where N is the number of cycles, C is a material constant and m is an exponent, usually about 3 or 4 for steel, and represents the slope of the curve when the data are plotted log(da/dN) against log(ΔK).

A crack will not grow under cycling loading unless the range of stress intensity factor during a fatigue cycle exceeds a critical value ΔK_{th} [31]. This value of stress intensity factor is called Threshold value and if ΔK is below a certain Threshold value, fatigue crack growth does not occur [31]. It can be obtained by carrying out fatigue tests on precracked plates and plotting the results as ΔK against crack growth rate (da/dN). The resulting curves were similar in shape to conventional S/N curves, ΔK_{th} being the value of ΔK at which a curve becomes parallel to abscissa (see Figure 5.3). The parameter ΔK_{th} therefore, is analogous to the fatigue limit [31]. Furthermore, the slope of the different curves are linked by the following relation:

$$k = -\frac{1}{m}$$

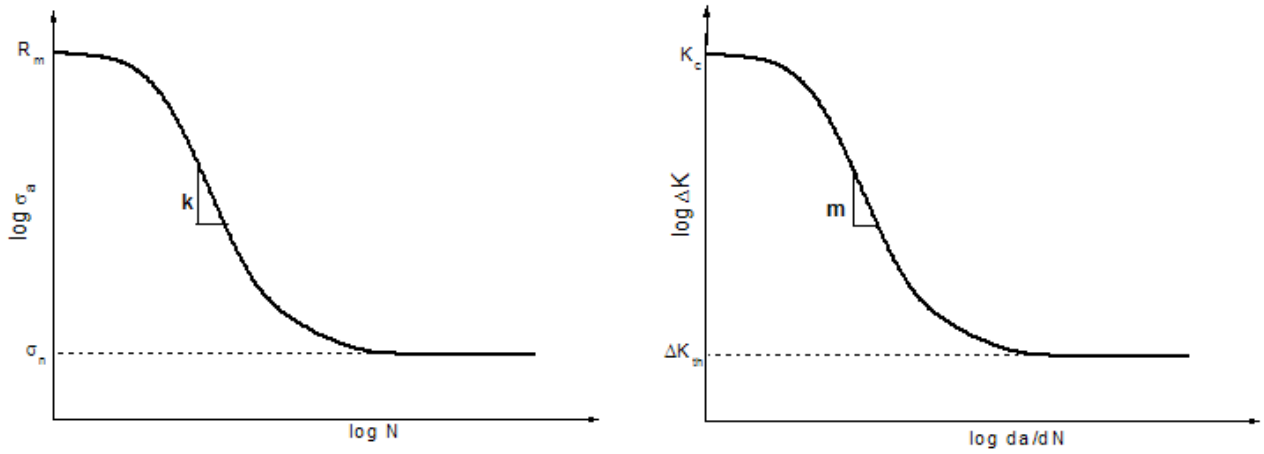

Figure 5.3: Wohler and FCGR curves.

5.1. High Cycle Fatigue of Austempered Ductile Iron

In the study of Lin at al. [12] rotary bending tests with stress ratio R equal to -1 were conducted on a number of different grades of Austempered Ductile Iron (designated as A, B, C, and D, the different chemical compositions and nodule parameters are given in table 5.1). The ADI heat-treat cycle consists of an austenitization in a salt bath at 900 °C for 1.5-2 h and 2 different austempering condition to obtain different mechanical properties related to changed microstructure. The first austempering, that generated the optimum strength (with a optimum combination of ultimate tensile strength, yield strength and hardness), was carried out at 300 °C: at this transformation temperature it was observed that the ferrite laths are finer and closer together. The second austempering, that generated the optimum strength (with a maximum value of impact energy), was carried out at 360 °C: at this temperature the ferrite laths become coarser and shorter. Chemical composition and nodule data of ductile irons are showed in table 5.1.

	C	Si	Mn	P	S	Mg	Cu	Ni	Mo	Nodule count ($n°/mm^{-2}$)	Nodule radius (μm)	Nodularity (%)
A	3.6	2.3	0.1	0.04	0.01	0.04	0.5	0.5	-	~ 100	25	~ 80
B	3.6	2.5	0.2	0.02	0.01	0.04	0.5	0.4	-	~ 110	20	~ 90
C	3.6	2.6	0.2	0.02	0.01	0.05	0.4	0.4	-	~ 150	17	~ 90
D	3.6	2.6	0.3	0.05	0.01	0.04	0.5	0.4	0.2	~ 200	12	~ 90

Table 5.1: chemical composition (%wt) and nodule data of ductile irons utilized in Lin's study [12], adapted from [12].

The effects of austempering temperatures, nodularity, nodule count and amount of retained austenite were discussed in that study [12] and were found the results presented below.

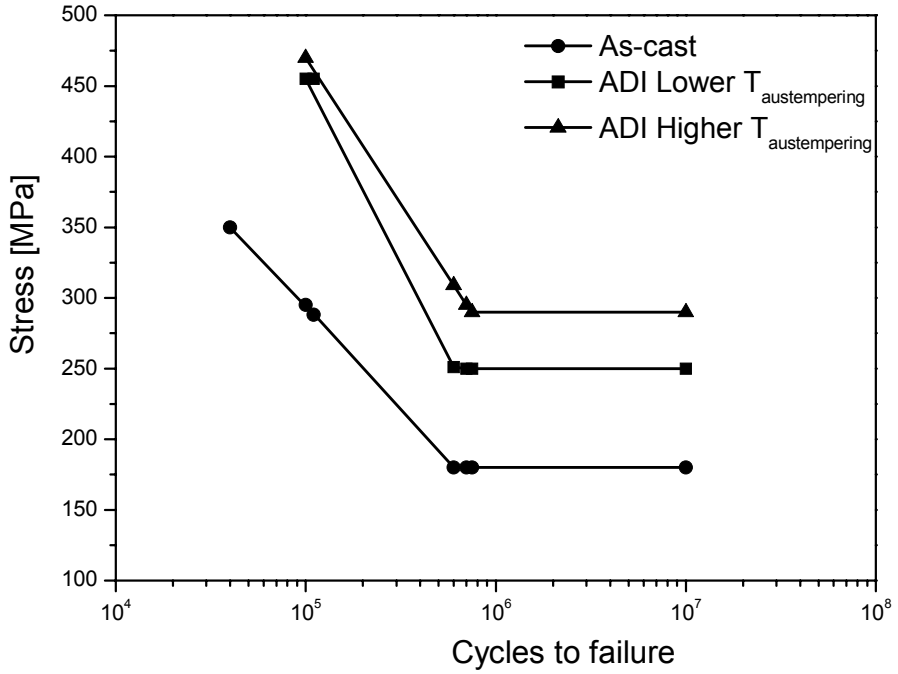

Figure 5.4: example of S/N curves for HCF obtained for as-cast iron and ADI treated at two different temperature to obtain optimum strength and toughness, adapted from [12].

The fatigue limit is not proportional to its tensile strength, but is related to its toughness and retained austenite content [12]. In general, ADI was achieved with austempering treatment that gave optimum toughness and larger amounts of retained austenite, which has a better HCF performance [12]. In addition, the fatigue ratio of ADI increased with a

decrease in tensile strength but with an increase in toughness and retained austenite content [12].

The HCF strength of ADI is increased with increasing nodularity [12]. Higher nodularity (must be > 80% according to ISO standard, but the new standard demands is >= 90%) tended to have a better HCF performance including higher fatigue limits and longer lives at stress levels above the fatigue limit [12]. Inferior nodularity means more graphite nodules of nonspheroidal shape so higher stress concentration factors and higher stress concentration at graphite/matrix interface as compared to spheroidal shape [12]. In addition, the difference in HCF strength due to varying nodularity was enhanced when the austempered temperature was decreased. This attributed to the more severe notch effect of graphite nodules in a matrix with higher strength and hardness formed at lower austempering temperatures [12].

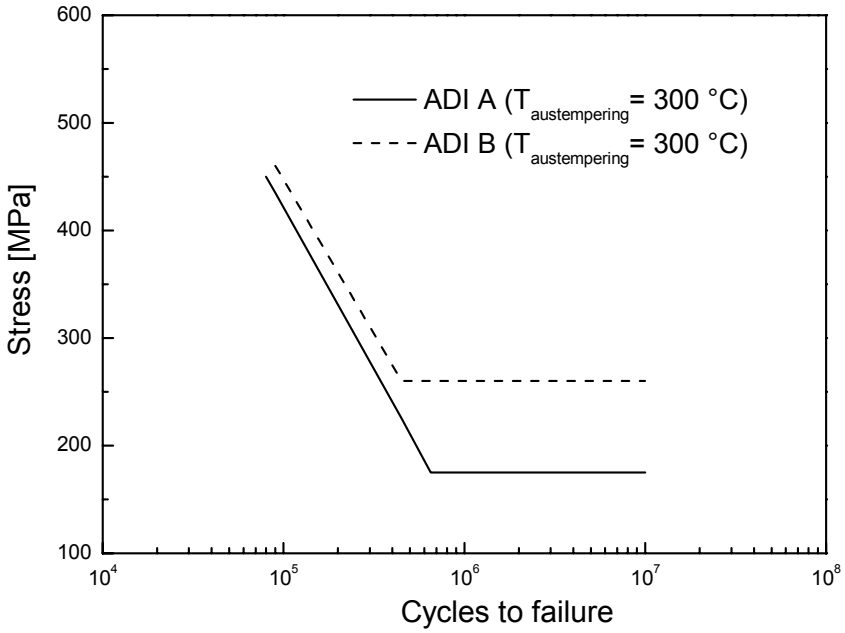

Figure 5.5: comparison of S/N curves between irons A and B at austempered temperature of 300 °C, adapted from [12].

In order to show the effect of nodularity on HCF, in Figure 5.5 the comparison between iron A and iron B is shown. These grades of ADI have difference in nodularity (~ 80% and ~ 90% respectively), but otherwise similar chemistries and close nodule counts. It can see that iron B with higher nodularity tended to have a better HCF performance including higher fatigue limit and longer life at stress levels above the fatigue limit. The difference

between the two HCF behaviours isn't strongly marked at low cycles, but it increases when the stress levels are close to the fatigue limit, where it shifts to lower value for iron with less nodularity.

The HCF resistance of ADI was improved when the nodule count increased, in particular at austempered temperatures for optimum toughness [12]. Therefore, ADI with a greater nodule count or a smaller nodule size exhibits a better HCF behaviour [12]. The more pronounced beneficial effect of a large nodule count on the HCF properties of ADI for the matrix structure with optimum toughness may be explained by the difference in the amounts of retained austenite. Greater amounts of retained austenite can create more barriers for fatigue crack growth and extend life [12].

The better HCF strength is suggested not to be attributed exclusively to the advantage of greater nodule count because this improvement was lost in LCF behaviour [12, 13]. It is probably related to the volume fraction, size and distribution of retained austenite in matrix [12]. It may be attributed to the larger amounts of retained austenite and a greater fraction of retained austenite in low concentration of carbon [12]. This low carbon austenite is more likely to transform to martensite under plastic deformation (stress-induced martensitic transformation) than carbon-enriched stable austenite, resulting in a greater fatigue crack growth resistance. The amounts of retained austenite increased with increasing the austempering temperature so a larger fraction of retained austenite would undergo martensitic transformation under plastic deformation. Stress-induced martensitic transformation of austenite occurred locally in the plastic zone ahead of the crack so as to relax the stress concentration at the crack tip. The accompanying volume change also encouraged plastically induced crack closure to occur, reducing the fatigue crack growth rate and increasing fracture toughness [12].

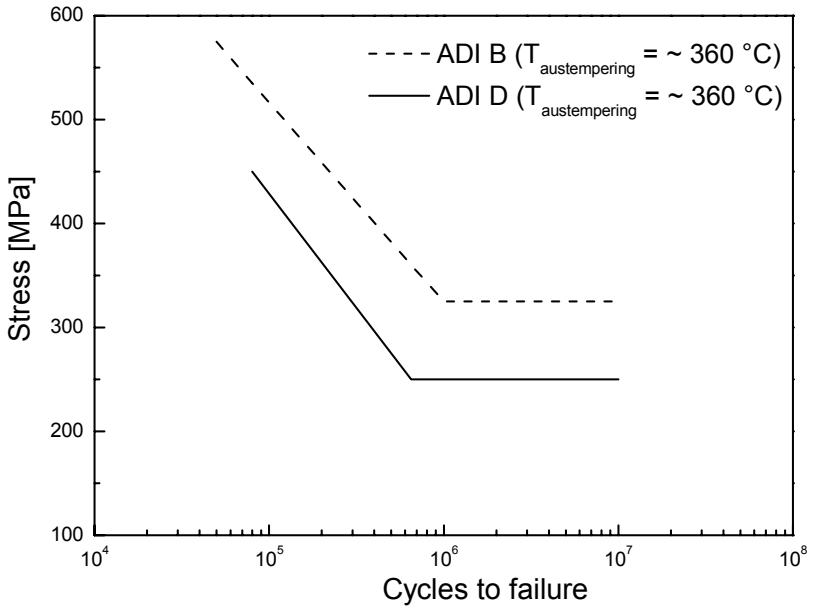

Figure 5.6: comparison of S/N curves between ductile irons B and D at austempered temperature of 360 °C, adapted from [12].

In Figure 5.6 the different behaviour between ductile iron B and D is shown. The chemical composition of iron D is close to that of iron B except for the addition of 0.2% of Mo and greater amounts of Mn. In addition, iron D has a nodule count of 200 nodules/mm^{-2}, more than the 110 nodules/mm^{-2} of iron B and also the amount of retained austenite is larger in D. ADI-B exhibits a much better HCF performance than ADI-B. The better HCF strength is not to be attributed exclusively to the advantage of greater nodule count as described above, because this improvement was lost in LCF behaviour [13]. So it can be concluded, as shown in Figure 5.6, that the effect of volume fraction, size and distribution of retained austenite in matrix strongly affect the HCF performance of ADI.

Large graphite nodules, inclusions, micro shrinkage pores, and irregularly shaped graphite clusters at or near the surfaces of the HCF specimens are the typical crack initiation [12]. Failure usually begin with extensive nodule decohesion from the matrix followed by localized plastic deformation in the matrix resulting in microcracks extending from many graphite nodules [12]. Decohesion is due to mismatch in mechanical properties between graphite and matrix structure and take place at the graphite/matrix interface at low level of strain. At the higher values of strain, localized plastic deformation and microcracking occur to relieve the stress concentrations caused by the graphite nodule voids [12].

ADI´s fatigue crack path largely depends on the location of the next nodule ahead of the crack tip [12]. It usually goes through the areas with highly distributed graphite nodules, which provide the least-energy path to link graphite nodules. For the crack path between two neighbouring nodules, fatigue crack was observed to grow along the austenite/ferrite interfaces or cut through the ferrite laths [12].
Results of another study about the high-cycle fatigue of ADI [16] show that the fatigue limit in ADI is controlled by a crack arrest. Ausferrite packet boundaries act as barriers for microstructurally-small cracks due to a requirement for the first stage growth in the ausferrite matrix. The strength of the barrier depends on the relative orientations of the microstructure at the boundary.

5.2. Low Cycle Fatigue of Austempered Ductile Iron

Lin et al. also investigated the low-cycle fatigue (LCF) properties of ADI [13]. In this work, unlike the case for HCF analysis, ADIs were tested under uniaxial condition under strain-control, constant amplitude, totally reversed loading (R = -1).
Heat treatment was consisted of first austenitization and austempering at two different temperatures to obtain two different microstructures. The chemical composition and nodule data of the different grades of iron were the same as the previous paragraph (table 5.1).

The austenitization was carried out in a salt bath at 900 °C for 1.5-2 h and 2 austempering treatments for each ductile iron were conducted to generate ADIs with two different optimal properties. For the first austempering condition, that generate the optimum strength (with a optimum combination of ultimate tensile strength, yield strength and hardness), the austempering treatment was carried out at 300 °C. At this transformation temperature was observed that the ferrite laths are finer and closer together. The second austempering condition instead, generate the optimum strength (with a maximum value of impact energy). The austempering temperature was chosen at 360 °C: at that transformation temperature the ferrite laths become coarser and shorter. The outcomes of study [13] are described below.

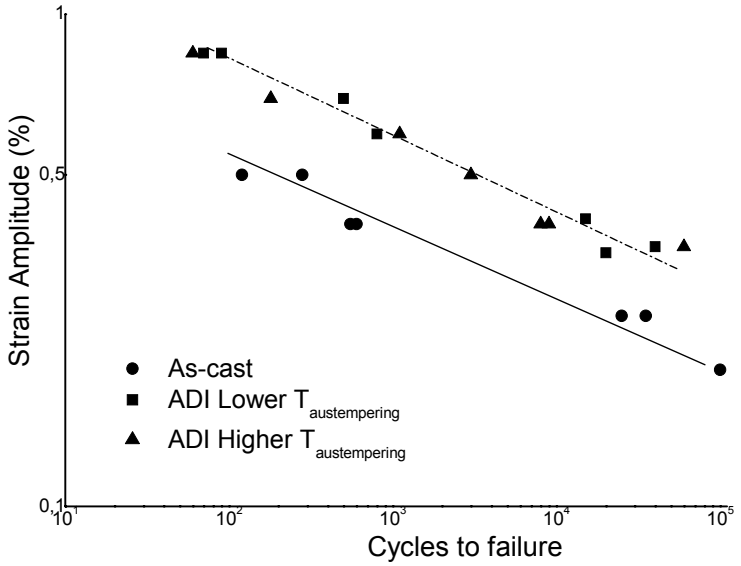

Figure 5.7: example of strain-life curves for LCF for as-cast iron and ADI treated at two different temperature to obtain optimum strength and toughness, adapted from [13].

As-cast ductile irons exhibited cycling hardening while austempered ductile irons showed cycling softening [13]. Ductile irons with initially hard and strong matrix structures will generally cyclically soften, and those with initially soft matrix structures will cyclically harden [13]. Such cyclic softening phenomenon was attributed to the continuous development of damage such as cracking and decohesion of graphite nodules at the matrix interface [13]. Whether a ductile iron austempered with the optimum strength or toughness would exhibit the optimum LCF performance may be related to graphite morphology [13].

In ADIs with a large nodule size, the voids formed by decohesion of graphite nodules would be larger as well as the induced stress concentration fields [13]. More deformation would take place in the matrix due to the larger areas under higher stress and lead to formation of more microcracks extending from the graphite nodules. So the austempered ductile irons with greater toughness would delay the propagation and link-up of microcracks and exhibit a longer LCF life [13].
On the other hand, ADIs with a smaller nodule size displayed smaller stress concentration fields and less induced deformation [13]. The formation of microcracks originated from the nodules was suppressed despite of the crack path between graphite nodules being shorter. Therefore, it would be more difficult to generate microcracks in ADIs with higher strength; so ADIs austempered at lower temperatures show higher LCF strength [13].

It was found that the LCF strength of ADI increased with increasing nodularity [13]. At both lower and higher austempered temperatures, ductile irons with better nodularity tended to have a longer fatigue life, in particular at small strain levels. Higher nodularity (> 80%) means more graphite nodules of spheroidal shape and lower stress concentration factors as compared to other nonspheroidal shapes [13]. This develops a less stress concentration at graphite/matrix interface. Therefore, increasing graphite nodularity can improve ADI's LCF strength [13].

It was found that the LCF strength of ADI increased with increasing nodule count [13]. For ductile irons with higher nodule counts, austempering for optimum strength generated the best LCF behaviour while the best LCF performance could be obtained by austempering for optimum toughness for ductile irons with lower (< 100 n°/mm^2) nodule count [13].
It was found that, as described above, an increase in nodule count could improve the LCF life of ADI for a given chemical composition. However, this improvement may be lost due to the effect of morphology of retained austenite [13]. A larger fraction of retained austenite that is not rich in carbon content, would transform to martensite under plastic deformation. Although the stress-induced martensitic transformation may have a beneficial effect on the HCF behaviour of ADI under rotary bending as reported in the previous paragraph, this is not the case for LCF behaviour of ADI under axial loading [13]. Since LCF test tests were conducted under axial cycling loading at very high stress levels, plastic deformation took place in the whole gage sections of the specimens. Consequently, larger amounts of stress-induced martensitic transformation might occur throughout the entire gage section of specimens, resulting in the embrittlement of the matrix, premature initiation of microcracks, and reduction of toughness and fatigue crack growth resistance [13]. In other words, ADI with larger amounts of austenite in low carbon concentration has a worse LCF performance under axial loading [13].

Fatigue cracks initiated not only from graphite nodules but also from casting defects. The fractures origins are identical to those observed in the HCF specimens [13].

The LCF failure in as-cast and austempered ductile irons began with extensive nodule decohesion from the matrix followed by localized plastic deformation in the matrix resulting in formation of microcracks emanating from many graphite nodules [13]. Selected

microcracks link up to form larger microcracks, which in turn can link up to initiate a primary crack or extend a propagating crack resulting in the final failure [13].

The fatigue crack propagation path depends strongly on the location of the next graphite nodule ahead of the crack tip, but in general is perpendicular to the loading direction [13]. The crack path between two graphite nodules is along the least-energy path which is often the interfaces between ferrite and austenite but is also influenced by ferrite-lath´s orientation relative to loading direction and by the presence of precipitated carbides which can change the least-energy path [13].

5.3. Low Cycle Fatigue of Austempered Ductile Irons at various strain ratios

In the study of Lin et al. [14], uniaxial LCF tests were conducted under strain-control with three strain ratios, R = -1, 0, 0.5 to investigate the low-cycle fatigue properties of ADI at various strain ratios. Two types of austempering treatments were applied to the base irons so as to investigate the response of different ausferritic structures. Chemical composition of ADIs tested is showed in table 5.2.

Element	C	Si	Mn	P	S	Mg	Cu	Fe	Bi
Percentage	3.6	2.5	0.2	0.03	0.01	0.04	0.6	bal.	40 ppm

Table 5.2: chemical composition (%wt) of ADIs tested in Lin et al. work [14], adapted from [14].

Test specimens were first austenitized in salt bath at 900 °C for 1.5 h after which they were either quenched in salt bath at 300 °C and 3 h for a higher strength value, or at 360 °C and 2 h for greater toughness; they were then cooled in forced air. As described above, a change from a fine to coarse ausferritic matrix structure can be seen as the austempering temperature increases. The greater toughness and ductility obtained at 360 °C result from the larger amounts of retained austenite present in the matrix [14].

For a given austempering treatment, the LCF life of ADI was decreased with an increase in strain ratio due to the intensifying mean stress effects [14] (Figure 5.8). The degree of

mean stress influence on ADI's LCF behaviour appeared to be function of austempering treatment and in turn the ausferritic matrix structure [14].

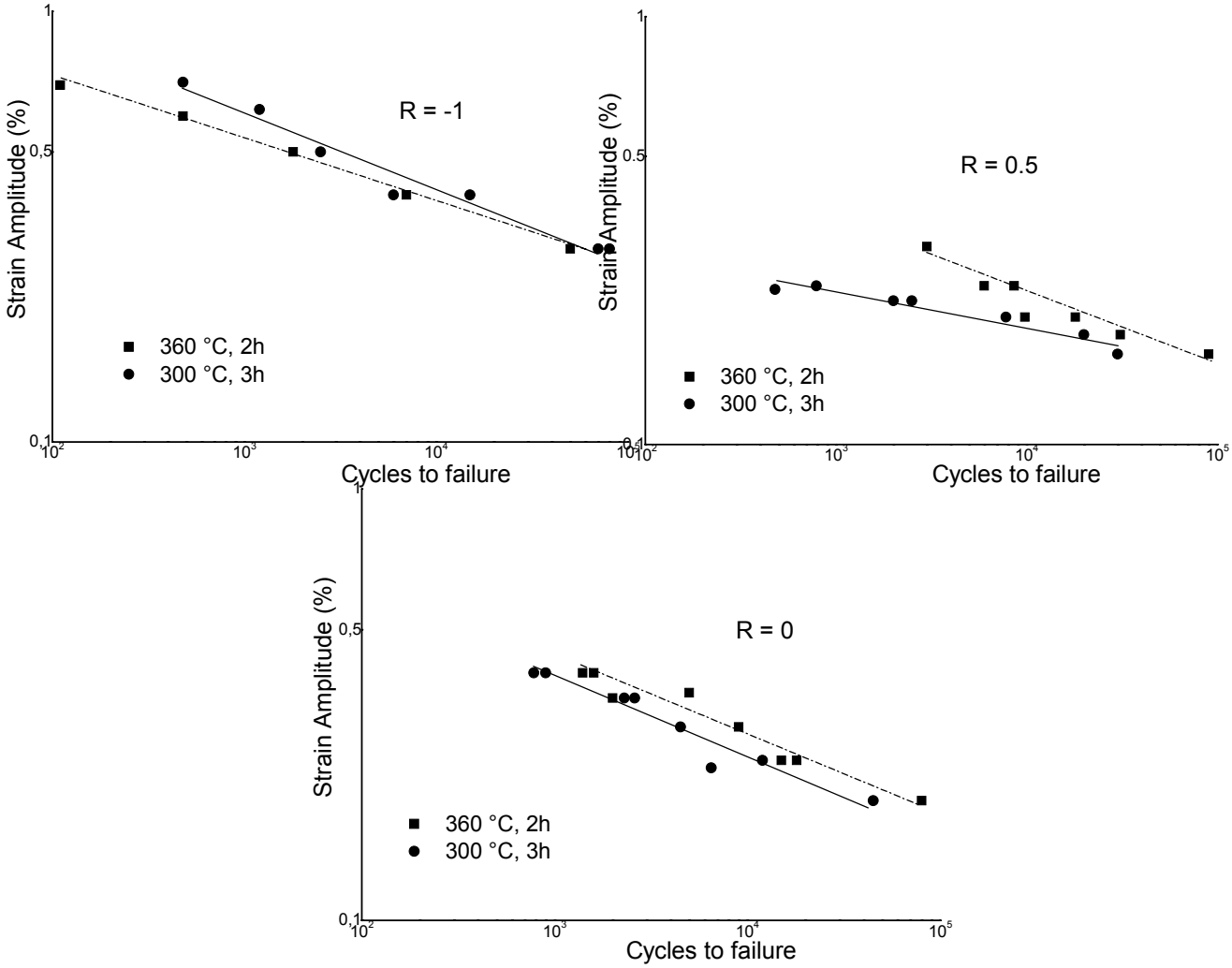

Figure 5.8: strain-life curves of ADIs in different strain ratios R, adapted from [14].

In completely-reversed LCF tests, ADI austempered at 300 °C provided more fatigue resistance than did those austempered at 360 °C due to less extent of martensitic transformation of unstable retained austenite [14]. The superiority of ADIs austempered at 300 °C to those austempered at 360 °C is related to the amounts and stability of the retained austenite in ausferritic matrix. ADIs with a greater volume fraction of retained austenite, particularly the unstable, blocky type, exhibited less LCF resistance due to the higher probability of plasticity-induced martensitic transformation under large magnitude of uniaxial loading [14]. Since LCF tests were conducted under uniaxial cycling loading at very high strain/stress level, plastic deformation took place in the whole gage sections of the specimens. Consequently, a greater extent of plasticity-induced martensitic transformation might occur during LCF test throughout the entire gage sections of ADI

specimens austempered at 360 °C, resulting in non-uniform, localized embrittlement of the matrix, premature initiation of microcracks, and reduction of toughness and fatigue crack growth resistance [14]. Therefore, the plasticity-induced martensitic transformation of unstable retained austenite is a detrimental effect on the LCF behaviour of ADI under completely-reversed uniaxial loading [14].

For the completely-reversed LCF tests, the difference in the mean stress levels between the two austempering conditions is not significant such that the LCF performance is mostly influenced by the effects of plasticity-induced transformation of unstable retained austenite to martensite [14]. For LCF tests at R = 0 and 0.5, the tensile mean stress levels are considerably higher in ADIs austempered at 300 °C than in those 360 °C ones leading to the shorter fatigue lives in ADIs austempered at 300 °C [14]. The degree of difference in the tensile mean stress level between two austempering treatments is extended as strain ratio and strain amplitude increases [14].

For each austempering treatment the fatigue life is significantly reduced with an increase in strain ratio, given a strain amplitude [14]. This can be attributed to the presence of tensile mean stresses for LCF tests at R = 0 and 0.5. The degree of reducing fatigue life by a larger strain ratio is more extensive for ADIs austempered at 300 °C indicating this grade of ADI is more sensitive to mean stress effects on LCF resistance [14] (Figure 5.9).

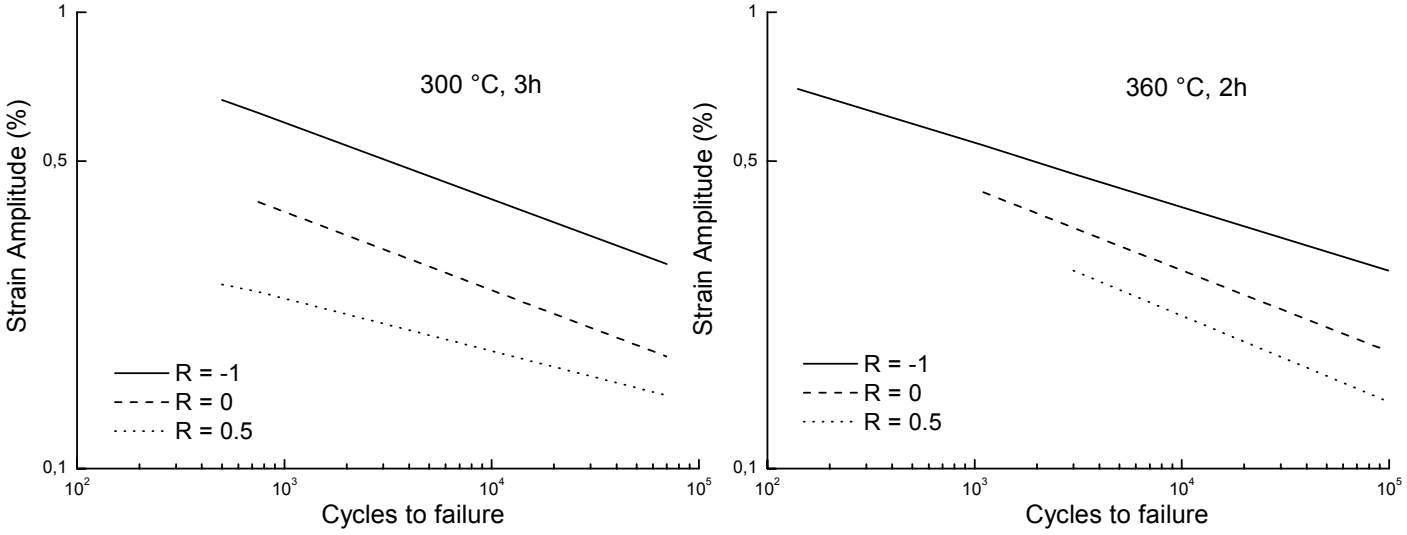

Figure 5.9: comparison of strain-life curves of ADIs with different strain ratios at two austempering conditions, adapted from [14].

5.4. Mechanism of fatigue crack growth in Austempered Ductile Iron

Fractographic analysis of fatigue fracture surfaces at threshold show striations typical of a ductile fracture mechanism [15]. In the proportional growth regime striations and cleavage planes are shown, revealing a quasi-cleavage failure mode [15]. The effect of matrix microstructure is minor, and can be attributed to the different crack closure contribution of each microstructure [15].

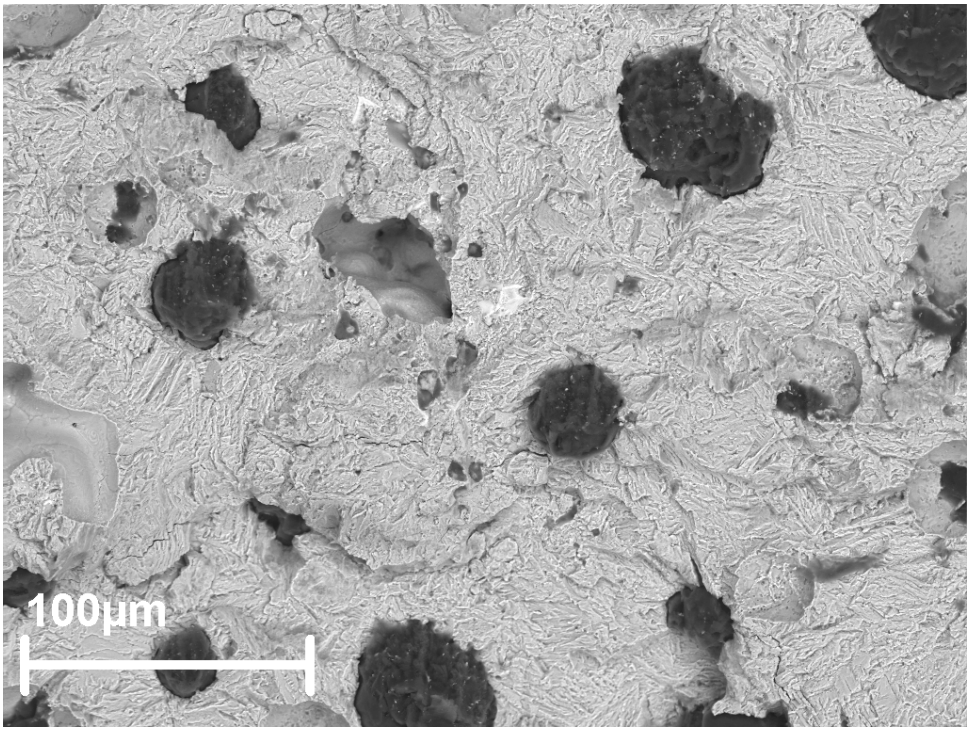

Figure 5.10: typical fracture surface in ADI.

The main propagation mechanism is given by small cracks emanating from nodules and growing towards the principal crack [15]. In other words, propagation of the main crack is partly due to the initiation and growth backwards of small cracks started at surface irregularities of the graphite nodules [15]. Initiation of these cracks is apparently activated by the stress raise produced when the tip of the main crack is at a sufficiently short distance from the nodule. These small cracks eventually coalesce with the main crack front, which continues to grow in the normal way until a new nodule is reached [15]. It is important to take into account that several nodules can be involved in the growth process at the different portions of the crack front, so that the average growth rate is affected by the size, shape and distribution of graphite nodules [15], a typical fracture surface due to fatigue is shown in Figure 5.10.

In the same study [15], Threshold and propagation fatigue regimes are analyzed for two commercial low alloy ductile cast irons, both austenitized at 900 °C for 2 h and then austempered at different temperatures and times. Two different casts were used: Cast 1 (0,28% Mn, 0,90% Cu, 0,53% Ni) was used for fatigue threshold measurements (batches named A-D), and Cast 2 (0,20% Mn, 1,33% Cu, 1,03% Ni) was used for fatigue propagation tests (batches named F-I). Samples were machined from 'Y' blocks of thickness 1 inch (cast 1), 1/2 inch. (cast 2a) and 3 inch. (cast 2b) respectively.
Crack growth rates and threshold stress intensity ranges ΔK_{th} were determined according to ASTM E-647. The results achieved are listed in tables 5.3 and 5.4 [15].

Batch	Austempering temperature [°C]	Austempering time [min]	ΔK_{th} [MPa$\sqrt{m}$]
A	260	120	4,77
B	290	120	5,18
C	320	90	5,61
D	360	90	6,35

Table 5.3: threshold stress intensity ranges for different heat treatment, adapted from [15].

Batch	Austempering temperature [°C]	Austempering time [min]	C	m
F (2a)	260	120	$8,18 \times 10^{-12}$	2,92
G (2b)	260	120	$2,39 \times 10^{-11}$	2,66
H (2a)	360	90	$1,16 \times 10^{-11}$	2,91
I (2b)	360	90	$6,79 \times 10^{-12}$	2,95

Table 5.4: values of m and C for different heat treatment, adapted from [15].

5.5. Influence of heat treatment on fatigue crack growth of Austempered Ductile Iron

Fatigue crack growth rates (FCGRs) of ADIs were compared with those of the as-cast DI with a bull's eye microstructure to examine the influence of austempering treatment on the FCG behaviour of DI dependent on the stress intensity range (ΔK) and load ratios (R) in Lin et al. study [19]. Chemical composition of iron is showed in table 5.5.

Element	C	Si	Ni	Cu	Mn	Mo	Mg	P	S
Percentage	3.5	2.3	0.5	0.4	0.2	0.2	0.04	0.03	0.01

Table 5.5: chemical composition (%wt) of iron in Lin's study [19], adapted from [19].

Influence of microstructure:

The FCG behaviour clearly shows a microstructural dependence as interactions of the FCGR curves for the as-cast DI and ADIs occurred at certain transition ΔK values [19].

For a given load ratio, the as-cast DI with a bull's eye matrix structure exhibited the lowest FCGR in the low ΔK regime [19]. In the high ΔK region, the ADIs with ausferritic matrix structures provided more or comparable FCG resistance as compared to the as-cast bull's eye microstructure depending on the R value [19]. In addition, ADI austempered at higher temperature with a coarser ausferrite matrix structure and greater amount of retained austenite exhibited lower FCGRs than did ADI austempered at lower temperature with a finer ausferritic microstructure and lower volume fraction of retained austenite [19] (see Figure 5.11).

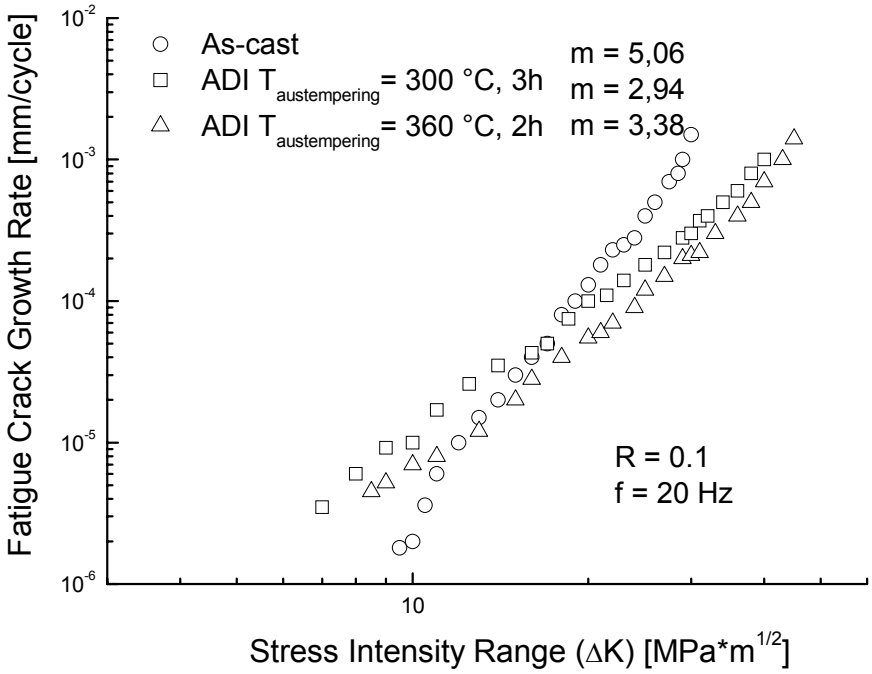

Figure 5.11: comparison of fatigue crack growth rate curves for as-cast and austempered ductile irons at R= 0.1, adapted from [19].

The graphite nodules, due to their low elastic moduli, are readily debonded from the matrix when cast iron is subjected to certain tensile loads. The stress concentration around the debonded graphite nodules would assist the nucleation and growth of microcracks from the nodule voids [19]. In the low ΔK region, where the applied load levels are small, the driving force for the direct extension of the main crack is small such that the process of linkage of microcracks emanating from the debonded-nodule voids and their coalescence with the main crack become the dominant stage in determining the FCGR [19]. Therefore, the greater FCG resistance observed at low ΔK regime for the as-cast DI may be attributed to its greater resistance to extension and linkage of microcracks from the voids around the debonded graphite nodules. As the ferrite ring around a graphite nodule in a bull's eye matrix structure is more ductile than the ausferrite, it would be easier for the microstructure to nucleate from the nodule void in an ausferritic matrix than in bull's eye structure [19]. Therefore, there would be more microcracks to link with each other and readily coalescence with the main crack in the ADIs at low ΔK regime when the driving force for the growth of the main crack is low. This might explain why the FCGRs were higher in the ADIs than in the as-cast DI at low regime [19].

In the high ΔK region where the driving force for extension of the main crack became stronger, the main crack would be prompt to interact with the graphite nodules ahead of the crack tip [19]. Therefore, the FCG behaviour at high ΔK regime would be influenced mostly by the resistance of the matrix structure to the propagation of the main crack, i.e., the fracture toughness [19]. As the ausferritic matrix structure in ADI provided more fracture toughness than did the bull's eye microstructure, the FCGRs at higher ΔK values would be lower in ADIs than in as-cast DI. In particular ADI having a coarser ausferrite microstructure and greater fracture toughness essentially exhibited the slowest FCGR at the intermediate and high ΔK regions [19].

It is believed that transformation of the unstable retained austenite under deformation to martensite around the highly stressed crack-tip area may also retard the growth of the main crack [19]. This deformation-induced martensitic transformation would relax the stress concentration at the crack tip and the accompanying volume change would also urge plastically induced crack closure to occur [19]. In this regard, ADI with a greater volume fraction of retained austenite would obtain more beneficial effects from this deformation-induced martensitic transformation to reduce the FCGR of the main crack as compared to the as-cast DI and ADI austempered at lower temperature with smaller volume fraction of retained austenite [19]. The crack closure effect caused by this type of martensitic transformation became insignificant when the load ratio increased. This might explain why the FCGR differences between ADI austempered at higher temperature and ADI austempered at lower temperature became smaller at higher R values [19].

Influence of load ratio:

The FCGR increased with an increased in load ratio for each material [19] (Figure 5.12). The load ratio effects on the FCG behaviour were more pronounced in the ADIs than in the as-cast DI [19]. In the low ΔK region where the driving force for the growth of the main crack was less intensive, the highly stressed area ahead of the crack tip was small and the nominal stress level at the ligament region in the specimen was low. As a result, a smaller number of graphite nodules were debonded from the matrix due to a lower tensile static stress level was provided to break the interface bond [19]. In addition, since the growth and linkage rather than the initiation of microcracks from the debonded-nodule voids played an important role in determining the growth rate of the main crack at low ΔK

regime, the load ratio effects became insignificant in the bull's eye structure which had more resistance to growth of microcrack than the ausferrite [19].

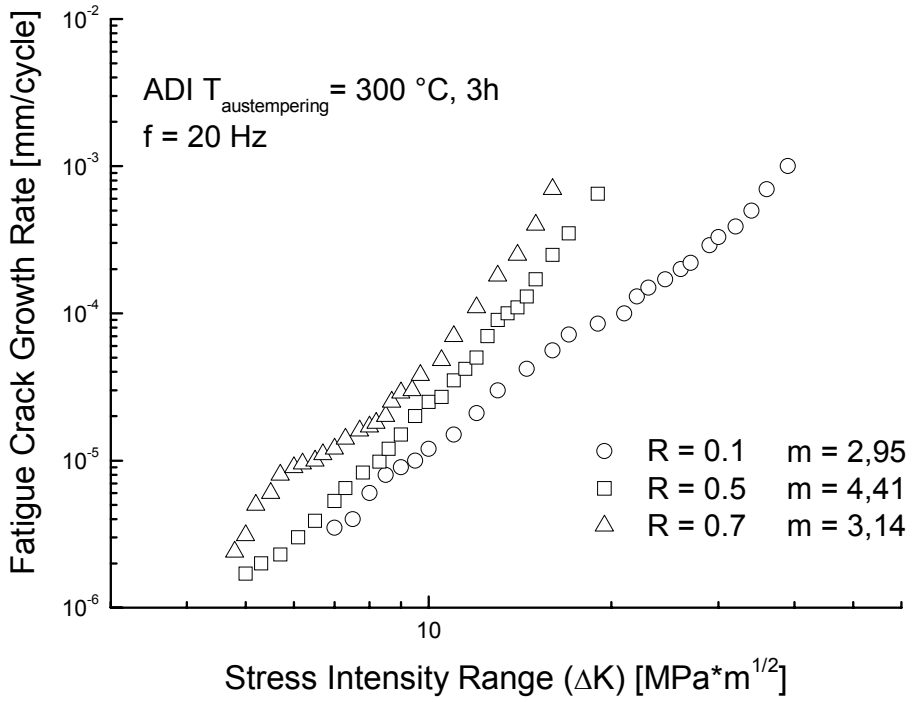

Figure 5.12: comparison of fatigue crack growth rate curves at different load ratios in ADI austempered at 300 °C, adapted from [19].

On the other hand, at the higher ΔK region, the main crack was provided with more driving force in promptly propagating toward the nodule-base microcracks or voids along its path [19]. The more microcracks or debonded-nodule voids are accessible along the propagation path of the main crack, the greater enhancement in the FCGR of the main crack will occur. Consequently, an increase in the load ratio would increase the static stress level and generate more debonded-nodule voids leading to an increase in the FCGR at high ΔK regime for the as-cast DI [19].

5.6. Effect of carbides on fatigue characteristics of Austempered Ductile Iron

The eutectic carbides remaining from the as-cast material proved to be responsible for the initiation of the majority of microcracks, except in some rare circumstances where porosity was responsible for crack initiation. The eutectic carbides, being very brittle, cracked easily [17]. The crack was not always perpendicular to the applied tensile axis and the subsequent nucleation of microcracks into the matrix was rapid [17].

Furthermore, it appears in general that the number of cracked carbides on initial loading has a significant effect in determining the life-time of a fatigue crack specimen; the higher the number of cracks on initial loading, the shorter the fatigue lifetime [17].

In general, high carbide area fractions promote coalescence-dominated fatigue crack failure, while low area fractions promote propagation-dominated fatigue crack failure [17].

The effect of carbide geometry and distribution has been investigated by classification of the features that cause individual carbides to crack and subsequently initiate microcracks [17]. Large or long and thin carbides on the whole appear to be susceptible to fracture. Carbides that are locally clustered and aligned at a high angle to the tensile axis are particularly susceptible to fracture except when the nearest neighbour is situated perpendicularly to that carbide with respect to the tensile axis. This perhaps suggests the presence of possible stress shielding effects in local populations showing a high degree of alignment [17].

The influence of the interaction between multiple cracks on crack growth behaviour greatly depends on the relative position of the cracks and the relative lengths of cracks [17]. The influence is strongest when the crack lengths are equal and decreases as the difference in crack length increases [17]. If the difference in crack length is greater than a certain level, the interaction is sufficiently small to allow the influence of interaction to be ignored. Coalescence in the specimens was typically of cracks of more comparable length, and crack interaction is therefore likely to be more significant [17].

It therefore seems reasonable to suggest that the critical factors for coalescence-dominated fatigue crack failure are the extent of damage (number of cracked carbides) on loading to maximum stress and crack growth in the depth direction following coalescence, not the nature of coalescence on the surface [17].

5.7. Effect of Titanium content on fatigue properties of Austempered Ductile Iron

There is an increasing trend to add small amounts of Ti to steels to increase their strength and deep drawability, with the aim of making lighter and thinner components, particularly in the automobile industry. As a result, there is an increasing amount of Ti-containing steel entering the scrap metal cycle and, therefore, becoming available for use by the iron foundry industry, including use for the manufacture of ductile iron castings [20].

The fatigue properties in ADIs deteriorate at higher Titanium contents, and this is attributed to the effect of Ti content on graphite nodule count [20].

In ADIs following an increase in nodule count with a decrease in Ti content , there was an apparent trend that the fatigue limit was increased [20].

It was noted that both the fatigue limit and the tensile strength of the ADIs increase with an increase in nodule count [20]. This may suggest that the nodule count affects fatigue properties in the same way as it affects the tensile strength, that is, through the effect of nodule count on unstable retained austenite. The increased spacing of the graphite nodules with the decrease in nodule count is known to be associated with an increased intercellular microsegregation of elements such as Mn and Mo (which are added to increase the austemperability). These elements locally retard the austenite transformation during austempering, resulting in less carbon enrichment of the untransformed austenite in the intercellular areas [20]. Under certain conditions, ADI can, therefore, contain areas where the retained austenite has a relatively low carbon content and may be mechanically or thermally unstable. During tensile and fatigue tests, this unstable retained austenite can undergo a strain-induced transformation to martensite [20]. The increased risk, with a decrease in the nodule count, of strain-induced martensite would lead to an easier crack initiation for ADIs with smaller nodule counts, because the strain-induced martensite is brittle. This ease of crack initiation would result in a decrease in the tensile strength and fatigue limit and is considered to be the most plausible explanation of the observed behaviour of the ADIs [20].

Further, the strain-induced martensite would reduce the crack-growth resistance, thus also reducing the fatigue life [20].

As far as the effect of Ti content on the fatigue behaviour of ADIs is concerned, it is concluded that the existence of Ti is deleterious, because the nodule count is decreased with an increase in the Ti content [20].

6. MATERIAL, EXPERIMENTS AND CHARACTERIZATION

In this chapter it's introduced the experimental procedure utilized to characterize the material and the tests conducted to analyze the properties of ADI studied.

6.1. Material

Different kind of low-alloy ductile iron have been studied. Their chemical compositions are listed in the table below. The castings of the rings were carried out by COMPONECTA for all the materials, the heat treatments were carried out by ATLAS COPCO for Alloy 1 and by ADI TREATMENT UK for Alloy 2 and 3.

The rings have internal diameter of 390 mm, external diameter of 520 mm and thickness of 25 mm, see Figure 6.1.

Material	C	Si	Cu	Ni	Mo	Mn
Alloy 1	3,55	2,42	0,68	0,52	0,11	0,20
Alloy 2	3,55	2,18	0,76	0,03	0,28	0,42
Alloy 3	3,55	2,35	0,69	0,70	0,15	0,19

Table 6.1: chemical compositions of alloys studied.

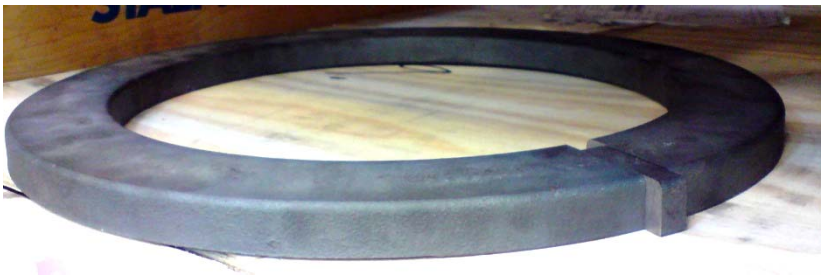

Figure 6.1: example of ADI ring.

All these alloys belong to a project started some years ago which aim is improve the characteristic of ADI.

Alloy 2 is the first developed in comparison with the other listed above and it is a ISO standard 900 ADI. It has already been studied in previous works but fatigue properties and fracture mechanism haven't been analyzed. It could be noticed that there's an higher percentage of some alloying elements (Mn and Mo mainly) compared to the other alloys,

which might lead to larger amount of carbides and segregation in the microstructure which therefore affect the properties of ADI, as described before. In this study it's taken as comparison material to evaluate the improvement of the newer alloys.

Alloy 1 has been developed to improve the previous material, to achieve refinement of the microstructure (reduce the amount of carbides and segregation) in order to improve the mechanical properties. It has reduced amount of Mn, Mo and Cu, but increased percentage of Ni.

Alloy 3 is the newest developed and its chemical composition is slightly different to Alloy 1. In fact the aim of this alloy is not improve the mechanical properties but make the ADI heat treatment feasible for industrial scale and for component which need larger casting, in order to make easier the entire process (temperature and time control). For this purpose it has mainly increased the percentage of Ni and a little bit of the other alloying elements (Mn, Mo and Cu) in order to enlarge the process window and then make the austempering time and temperature control easier. However, the increase of alloying elements, might affect the mechanical properties of this alloy.

6.2. Heat treatment

The industrial ADI heat treatment has been examined only for Alloy 1: to investigate the industrial ADI heat treatment comprising of austenitization and austempering (isothermal transformation, see Figure 6.2), both were varied separately. First, the austenitization temperature of 880 °C was investigated for austempering temperatures of 360, 385 and 400 °C. Thereafter, different austenitization temperatures of 840, 860 and 880 °C were investigated with an austempering temperature of 400 °C.

For this kind of alloy the austenitization time is 75 minutes and the austempering time is 90 minutes.

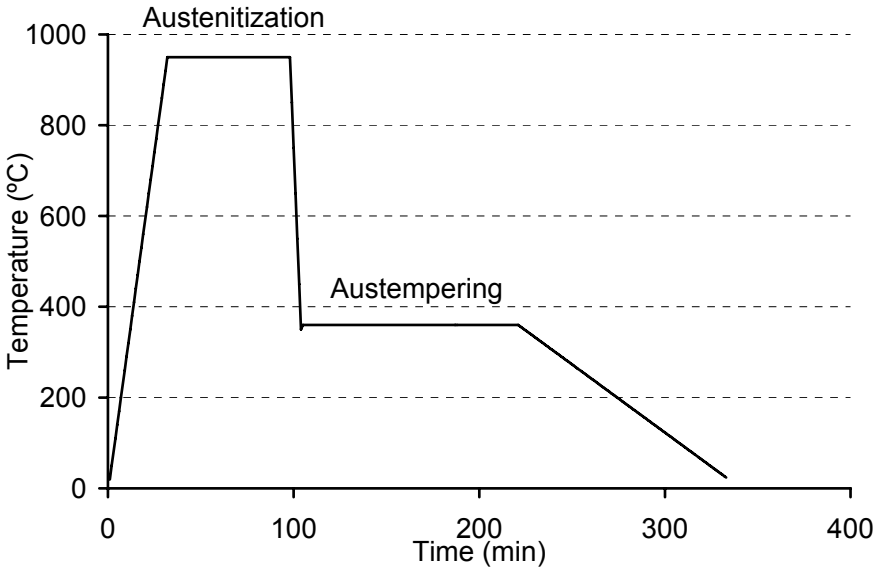

Figure 6.2: illustration of typical ADI heat treatment cycle.

Alloy 2 and 3 have been tested only for one industrial heat treatment, which consist of austenitization temperature of 840 °C and austempering temperature of 400 °C. The austenitization and austempering times are 90 minutes for both the alloys.

6.3. Characterization

The characterization of the specimens was carried out to identify several aspects of the microstructure. In particular, the aim of the characterization was to quantify the amount of martensite, the nodularity, the quantity of carbides, the segregation and porosity and analyze the morphology of ausferrite of the ADI.

To characterize the different ADIs samples were extracted by cold sawing from different positions (inner, middle and outer positions and ring's normal cutting direction). The metallographic sample preparation was carried out by using standard techniques: the specimens were grinded with 125, 78, 46, 30, 22 and 14 μm silicon carbide (SiC) papers (where the numbers represent the size of the silicon carbide particles), as well as polished with diamond paste (6 and 3 μm). Some samples were etched with Nital 3% to elucidate the phases and their morphologies.

To study the microstructure of ADI material, in particular to reveal the morphology of the different phases, in order to obtain a general overview of the microstructure of the samples, Light Optical Microscopy (LOM) was used. Some pictures of un-etched as well as etched microstructure were taken.

By un-etched pictures were measured the nodularity, the nodule count per unit of area and the nodule radius of all the samples by using the software AxioVision Rel. 4.7 coupled with the LOM, which consented to select the graphite nodules according to their colour (see Figure 6.3). The program allowed to know the form factor, the number of selected regions and their radius. The form factor of a region describes the form of a region on the basis of its circularity (a perfect circle is given the value 1, the more elongated the region is, the smaller the form factor, the value range is between 0 and 1). The calculation is based on the following formula:

$$Form\ circle = \frac{4\,\pi\ Area}{Perimeter^2}$$

where *Area* and *Perimeter* are referred to the area of filled region and the perimeter of the external contour of the nodules.

The number of regions measured displays the number of regions measured within the measured mask. The radius was calculated as radius of circle with an equal area (it is assumed that the area in question is that of a circle) using the following formula:

$$Radius = \sqrt{Area/_{\pi}}$$

With these data it has been chosen the graphite nodules and deleted the “fake” nodules as pores or other defects that were measured by the software. Following criteria has been used:

- form factor had to respect the standard demands:

0,625 < form factor < 1 → good nodule;

0,525 < form factor <= 0,625 → badly formed;

- graphite area had to be greater than 80 μm² due to the program was able to select items that had the same colour as graphite nodules but they were defects or points in the image due to the light of the microscope and the roughness of the surface.

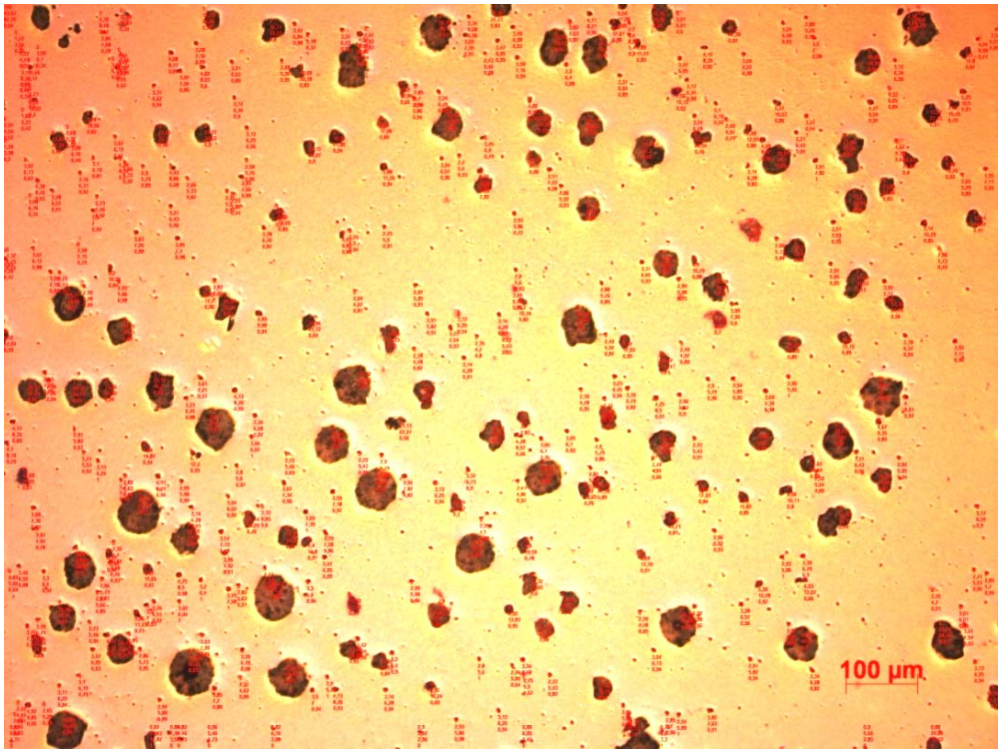

Figure 6.3: example of un-etched microstructure and graphite nodules analysis of ADI studied

For each material the measurements of nodularity, nodule size and nodule count were carried out in three different positions of the ring (inner, middle and outer) and a couple of pictures were taken for each position, in order to calculate the nodularity and nodule size of between 200 and 300 nodules for each position of the ring.

By etched pictures it was possible to analyze the phases morphology and make considerations about the microstructure. Pictures with different magnifications were taken in order to observe the shape and features of the phases, the grain boundary, and investigate the presence of carbides, segregation or unexpected phases.

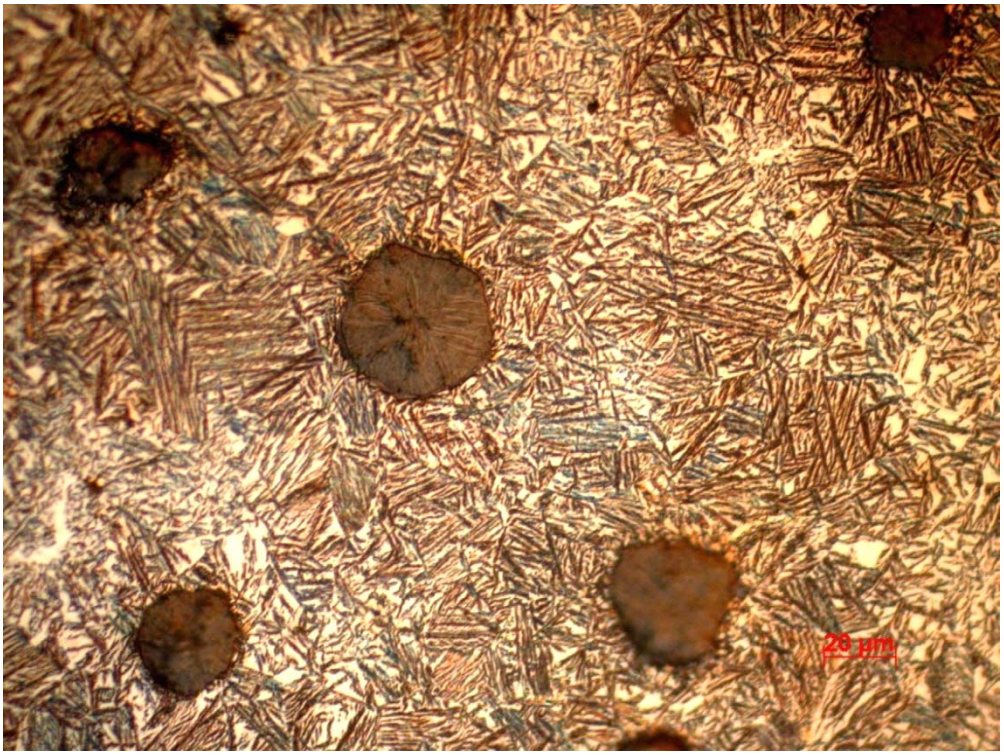

Figure 6.4: example of etched microstructure of ADI studied (Alloy 1).

The amount of retained austenite and its carbon content were measured by X-Ray Diffraction (XRD). The samples were analyzed over an angular range of 2θ 50-160° using a Chromium target and Vanadium filter at a scan speed of 0.05° s^{-1}. An X-ray diffractometer was employed to measure the retained austenite content of the ADIs using the simplified method described by Miller:

$$\gamma_{ret} = \frac{1.4I_\gamma}{I_\alpha + 1.4I_\gamma}$$

where

$$I_\gamma = \frac{I_{\gamma 220} + I_{\gamma 311}}{2}$$

$$I_\alpha = I_{\alpha 211}$$

and $I_{\gamma(hkl)}$ and $I_{\alpha(hkl)}$ are the intensities of the (*hkl*) reflections from the austenite (γ) and

the ferrite (α) phases, respectively. The profiles were analyzed in a computer to obtain peak positions as well as the integrated intensities. Volume fraction of the austenite was determined by direct comparison methods uses integrated intensities of (210) and (211) peaks of ferrite and (111), (220) and (311) peaks of austenite, in this work only the (211) peak of ferrite and the (220) peak of austenite was used due to the low intensity of the other peakes. The average carbon content was calculated using the dependence of the austenite lattice parameter on carbon content. Two models proposed by Roberts [44] and Bayati et al. [45] was used and thus calculations were performed with the equations:

$$C_\gamma = \frac{a_\gamma - 0{,}3548}{0{,}0044}$$

$$C_\gamma = \frac{a_\gamma - 0{,}3555}{0{,}0044}$$

where C_γ is its carbon content in weight percent and a_γ is the lattice parameter of austenite in nanometers.

The porosity was evaluated by Archimedes principle, which involved the measurements of the mass dry, mass in water and mass tepid (the mass of the specimen after it was dipped into water and quickly dried the surface in order to reveal the volume of open pores) of all the samples. All the measurements were performed by the balance for density

determinations Mettler Toledo AG285 which permitted to evaluate the mean porosity with the calculations listed below.

A = mass dry, B = mass tepid, C = mass in water
B - A = volume of open pores (cm^3)
B - C = exterior volume (cm^3)
100*(B - A)/(B - C) = volume of open porosity
A/(B-C) = density (g/cm^3)
100-[((A/(B-C))*100)/theoretical density] = mean porosity (%)
(where the theoretical density has been chosen equal to 7,22 g/cm^3)

The hardness was measured by using Vickers method, performed by Wolpert Universal Hardness Tester, under 3 different loads (20, 30 and 40 kg) and determined as the average value of at least 10 readings. The length of the diagonals of the pyramid indent were measured and the average of the measurements gave back the value of hardness listed in the manual of the hardness tester. The hardness was measured on samples grinded and polished but un-etched.

6.4. Fracture mechanism analysis

Samples of ADI were pulled as tensile test in order to investigate the fracture mechanism. Besides this experiment was carried out to compare the behavior when the material is subjected to static load (present test) to dynamic load (fatigue test, introduced in the coming paragraph). The aim of experiment is make a qualitative analysis about the behavior of the material when a static load is applied and investigate the fracture mechanism in ADI.

The test was performed by Scanning Electron Microscopy (SEM) to evaluate the favourite sites where the crack nucleation occurs, which is the favourite path for the crack propagation, and, in general, make considerations about the fracture mechanism showed by the material. The tensile load was applied in the SEM and increased step by step in order to analyze the entire surface of the specimen and estimate where the cracks occurred and propagated. A preload of 25 MPa was applied and the load was increased step by step from 25 to 1000 MPa.
The samples utilized for this purpose were extracted from the rings and machined in order to obtain a suitable shape for the SEM (see Figure 6.5). Then they were polished and

etched with either Nital 3% or Picric acid 3% to elucidate the different phases in the microstructure.

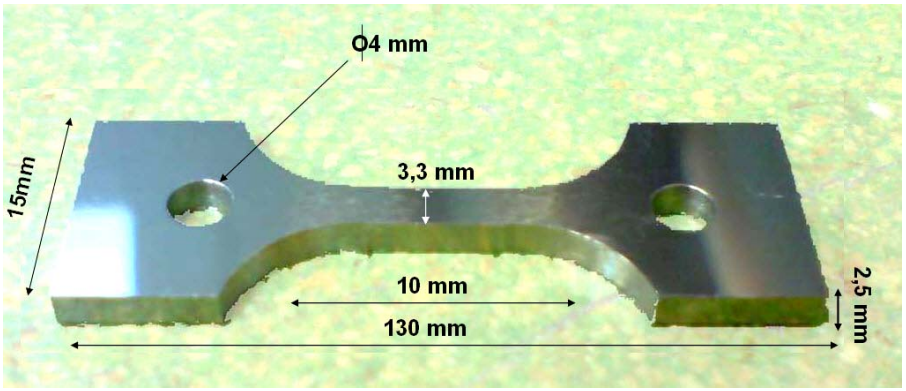

Figure 6.5: sample for fracture mechanism analysis performed by SEM.

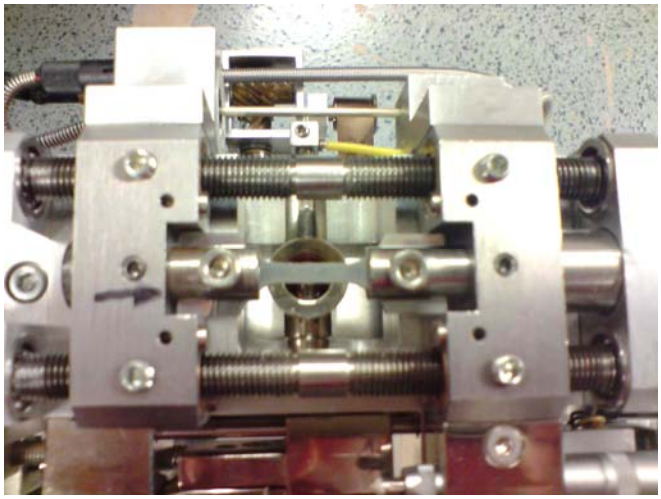

Figure 6.6: sample mounted on the tensile device of SEM.

6.5. Impact test

In order to determine the impact energy of ADI materials, the standard Charpy-type impact test for austempered ductile iron was performed following the standard ASTM A 327M. All the impact tests were carried out by ESAB.

All the tests were conducted at ambient conditions, using a pendulum-type impact machine with a capacity of at least 150 Joule. The impact tests were conducted to un-notched Charpy bars, with square cross section 10x10 mm and 55 mm of length, as

suggested in the standard adopted (see Figure 6.7). The samples were extracted from the different positions (inner, middle and outer position and normal cutting direction) for each ring and then machined in order to achieve the desirable shape and a smooth surface.

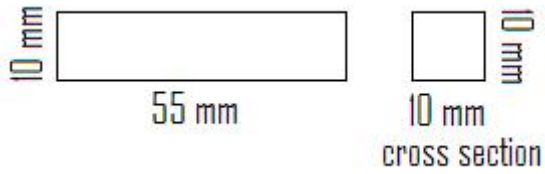

Figure 6.7: dimensions of un-notched Charpy bar impact test specimen.

The impact test was performed for all the alloys and the impact energy, or the energy absorbed by the material during the impact, necessary to break it, calculated assuming that its equal to one lost by the pendulum, was expressed in Joule.
Postfailure fractographic analysis was performed with Scanning Electron Microscopy (SEM) to evaluate the fracture surface of the broken samples.

6.6. Fatigue Crack Growth Rate test

Measurement of Fatigue Crack Growth Rates (FCGR) were conducted following the standard ASTM E 647. This test method covers the determination of fatigue crack growth rates from near-Threshold to K_{max} controlled instability. The fatigue crack growth rate (*da/dN*) is expressed as crack extension per cycle of loading. The stress intensity factor range (ΔK) is the variation in stress intensity factor in a cycle, that is $\Delta K = K_{max} - K_{min}$, where K_{max} is the maximum stress intensity factor or the maximum value of the stress intensity factor in a cycle, this value corresponds to σ_{max}, and K_{min} is the minimum value of the stress intensity factor in a cycle, this value corresponds to σ_{min} when R>0 and is taken to be zero when R<=0 (see Figure 6.8).

All tests were carried out in pull-push mode at room temperature in laboratory air, using a servo-hydraulic INSTRON 8501 test machine in load control mode. The tests were carried out at a frequency of 20 Hz, with a stress ratio $R = \sigma_{min} / \sigma_{max} = -1$ and 0. The load was varied during the test in order to achieve the entire curve for each material, from Threshold

value, defined as the asymptotic value of ΔK at which da/dN approaches zero, to critical K value, for which the crack growth rate increases to failure.

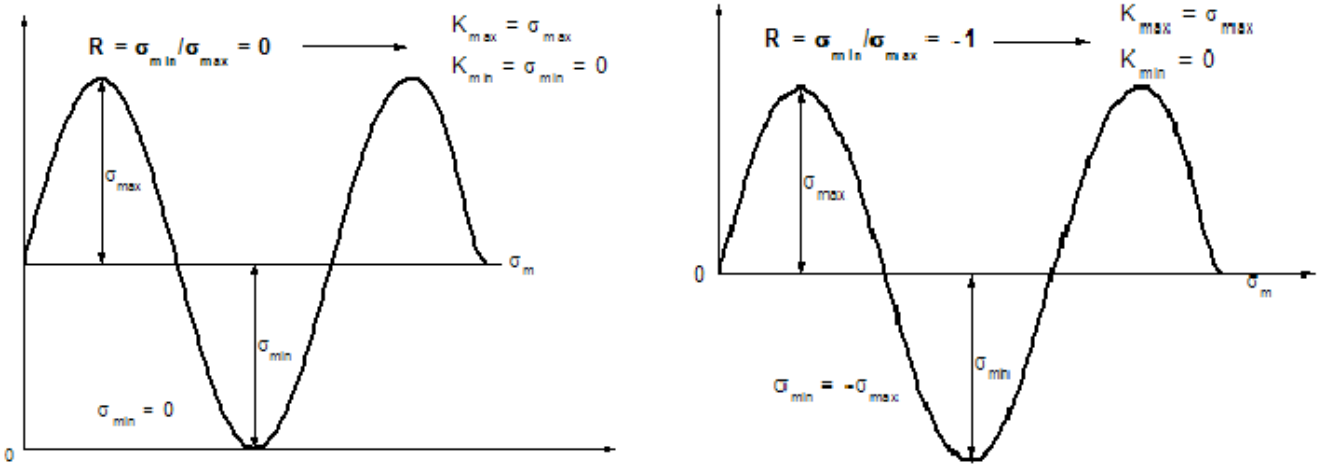

Figure 6.8: choice of K_{max} ad K_{min} for stress ratio R = 0, -1.

Not all the alloys were tested, only Alloy 2 and 3. It has been chosen these alloys to compare the newest material (Alloy 3) to the oldest (Alloy 2), in order to evaluate the real improvements and realize that both alloys fulfill the standard demands.

The samples utilized in this test measured 200 mm in length, 20 mm in width and 5 mm in thickness (rectangular cross section 20x5 mm, see Figure 6.9). They were extracted from the rings and then machined in order to achieve the shape predicted in the standard. The samples were polished to facilitate the measurements of the crack length and to observe the propagation of the crack in order to make consideration about the fracture mechanism. In each specimen was created a notch on one of its side, approximately in the middle position; it was made by hacksaw and then measured its length before start the test.

To measure the length of the crack the test machine was stopped and the length was evaluated by optical microscope 50x magnification, resolution better than 0,01 mm (see Figure 6.10).

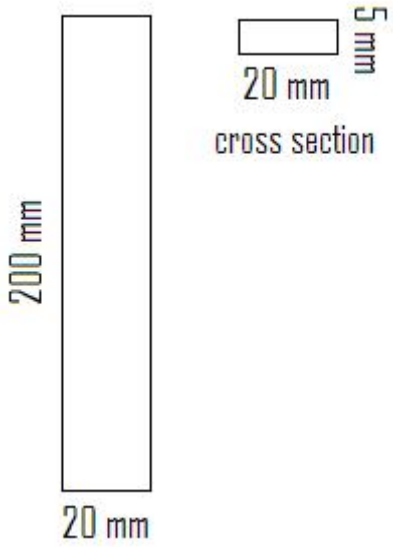

Figure 6.9: dimensions of sample for fatigue crack growth rate test.

Figure 6.10: equipment utilized in the fatigue crack growth rate test.

At the end of the experiment the length of the crack (a) in relation to the number of cycles (N) along the duration of the test has been achieved and a graphic as one shown in Figure 6.11 has plotted.

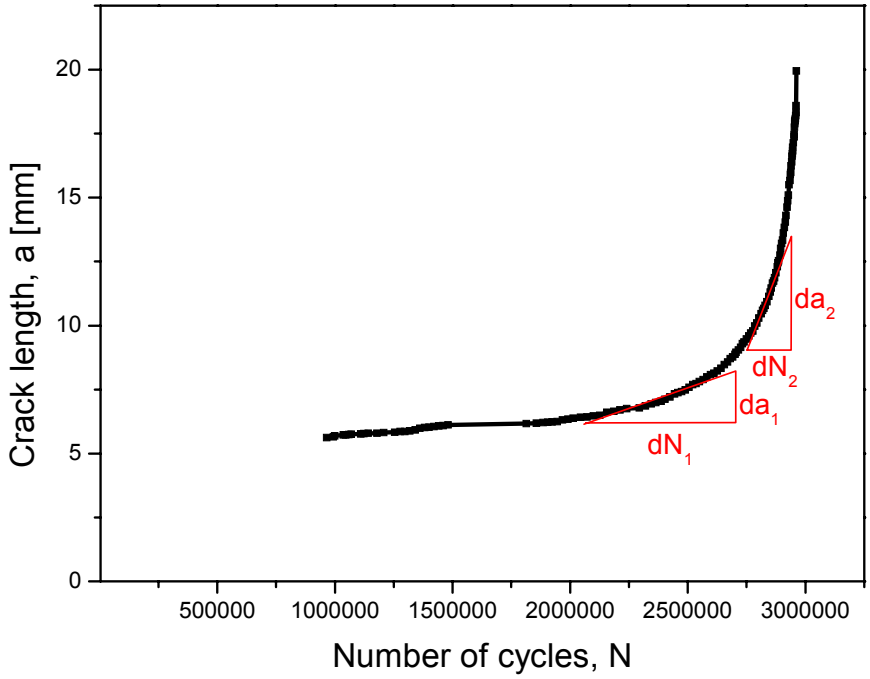

Figure 6.11: example of relation crack length-number of cycles achieved in the fatigue test.

The relation between crack length (*a*) and number of cycles (*N*) has been derived to obtain the slope of the curve for each point (*da/dN*), as shown in Figure 6.11.
To achieve the stress intensity factor range was used the following formula:

$$\Delta K = \Delta\sigma \cdot \sqrt{a \cdot \pi} \cdot f\left(\frac{a}{w}\right)$$

where: $\Delta\sigma$ is the stress range but, in order that R is equal to 0 and -1, $\Delta\sigma = \sigma_{max}$;

a is the crack length;

and $f\left(\frac{a}{w}\right)$ is a geometrical factor determined as [46]:

$$f\left(\frac{a}{w}\right) = 1{,}112 - 0{,}543\left(\frac{a}{w}\right) + 0{,}254\left(\frac{a}{w}\right)^2 + 10{,}681\left(\frac{a}{w}\right)^3 - 18{,}254\left(\frac{a}{w}\right)^4 + 10{,}356\left(\frac{a}{w}\right)^5$$

The results have been plotted as *da/dN* as a function of *ΔK* and *log(da/dN)* as a function of *log(ΔK)*, as commonly used (see Figure 6.12).

The slope of the linear part of curve achieved plotting *log(da/dN)* vs *log(ΔK)* was measured (see Figure 6.12). The slope of that curve is the same parameter (called *m*) which appears in the Paris law, a law that describe the behavior of the curve in the linear part:

$$\frac{da}{dN} = C(\Delta K)^m$$

So, since *da/dN* and *ΔK* were experimentally determined, and *m* calculated measuring the slope of the linear part of the curve, it has been possible to calculate the constant *C*.

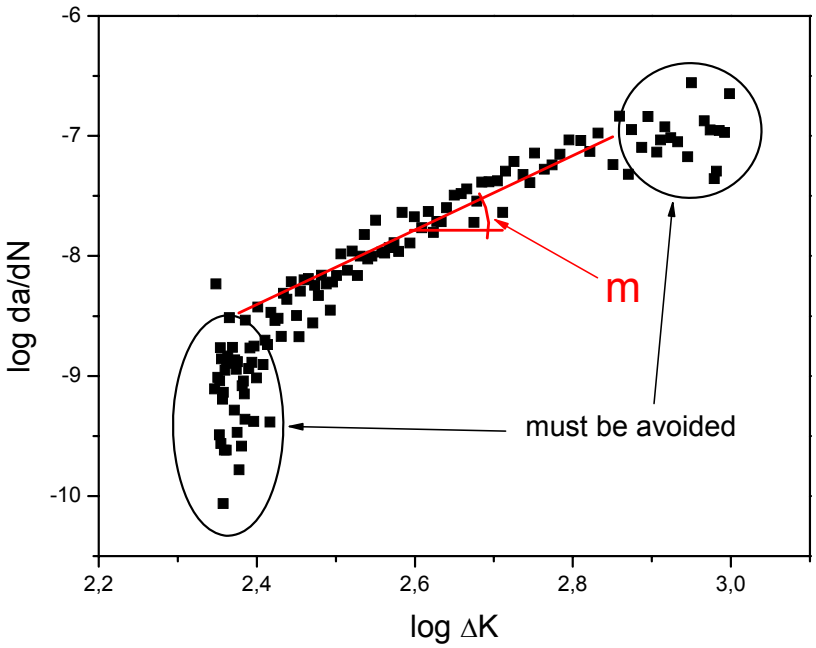

Figure 6.12: example of log(da/dN) vs log(*ΔK*), and calculation of m.

Postfailure fractographic analysis was performed with Scanning Electron Microscopy (SEM) to evaluate the fracture surface of the broken samples.

7. RESULTS AND DISCUSSION

The aim of this chapter is to show the analysis results of the investigated ADI-material.

7.1. Characterization

7.1.1. Light Optical Microscope

- **Microstructure characterization**

The pictures below show the morphology changes with austempering temperature for the investigated ADI-alloys studied.

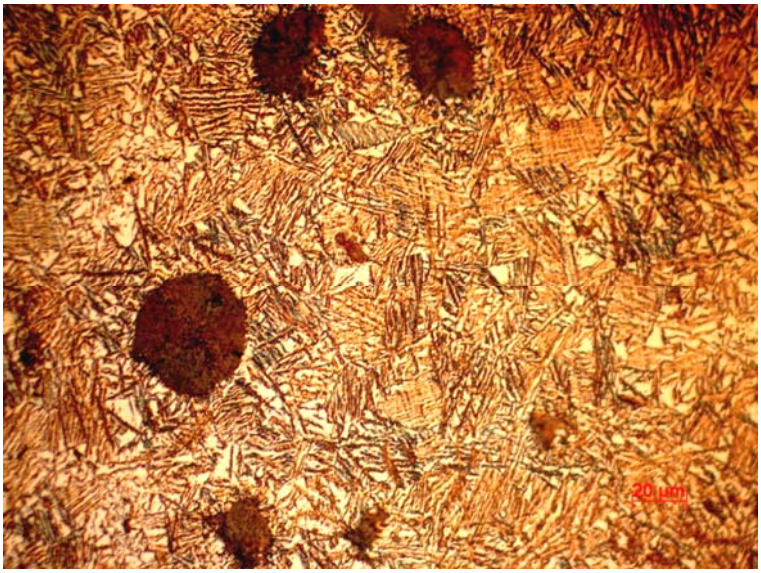
20 µm

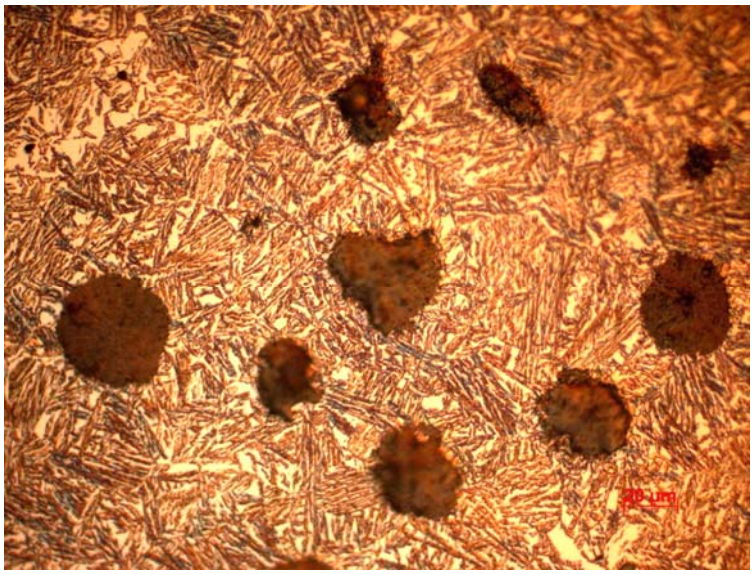
20 µm

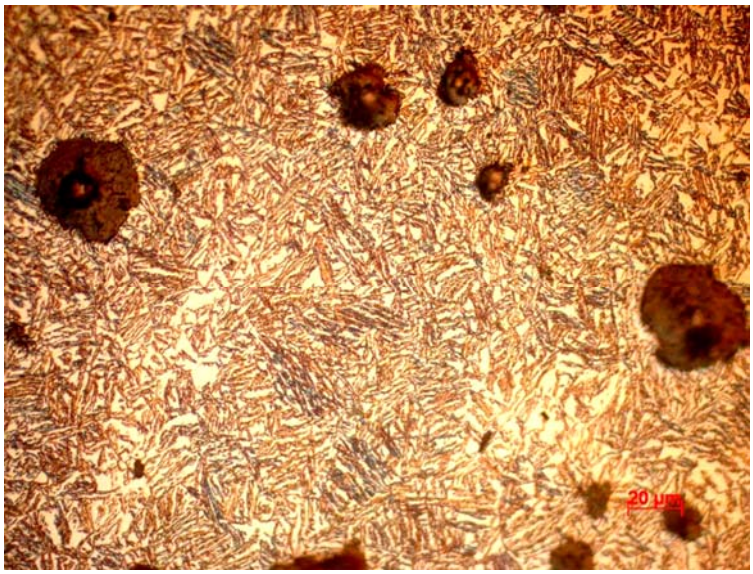
20 µm

Figure 7.1: magnification of ADI microstructure for different austempering temperatures (respectively 360, 385 and 400 °C) for the same austenitization temperature (880°C) of Alloy1.

Concerning the microstructure, as can observed in Figure 7.1, the brown needles represent the ausferrite (or acicular ferrite). They are interconnected by lighter areas, which correspond to retained austenite. The dark gray dots features are the graphite nodules.

Looking at the pictures above a clear difference between the different austempering temperatures is hard to see. That might be explained by the slightly different of the austempering temperatures chosen.

However, more small regions of retained austenite and an increase of the thickness of ausferrite needles could be seen when the austempering temperature increases from 360 °C to 400 °C. Therefore a qualitative analysis of the ferrite needles was conducted. This included the ratio between the thickness and the length of some needles of ausferrite was measured for the samples austempered at different temperatures (see Figure 7.2). At least 5 measurements for each specimen were performed, and the increase of the ratio aspect increasing the austempering temperature was confirmed (Figure 7.3).This result is in agreement with the literature [5] which asserts that at low austempering temperatures, due to high cooling, a high nucleation rate results in a large number of fine ferrite needles and, on the other hand, at higher temperatures, the lower nucleation rate results in fewer ferrite needles, each growing to a larger size. In fact, increasing the austempering temperature, resulted in the coarsening of the bainitic ferrite as well as an increase in the austenite content, as described in the previous paragraphs.

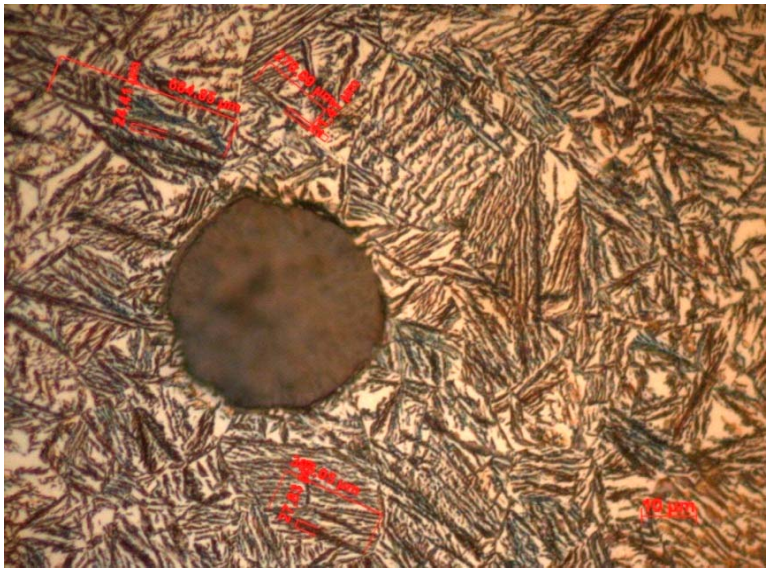

Figure 7.2: example of measurement of thickness and ratio of ausferrite needles.

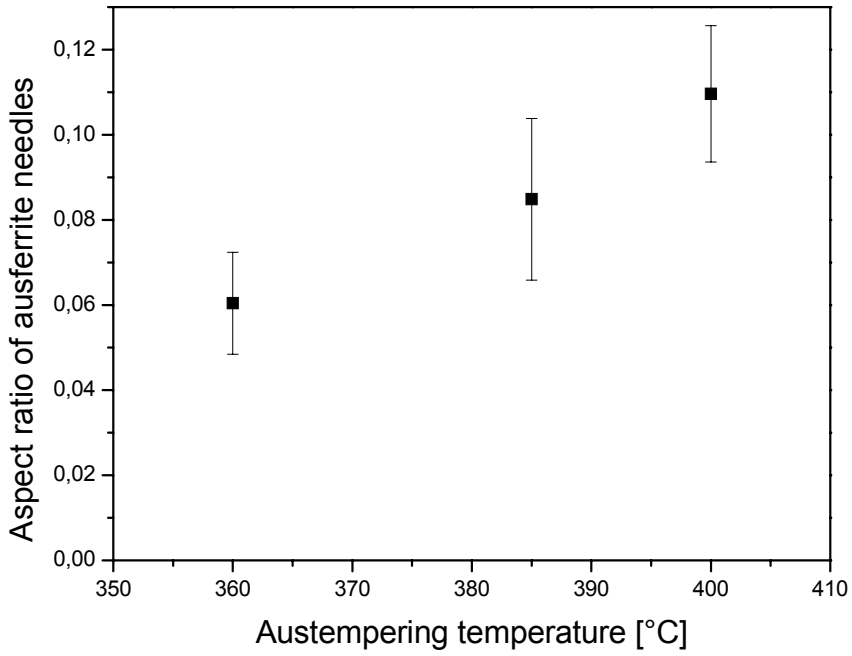

Figure 7.3: relation between aspect ratio of ausferrite needles and austempering temperature for ADIs studied.

The pictures below show the variation on the microstructure for the austenitization temperatures for Alloy 1(840, 860 and 880 °C, see Figure 7.4).

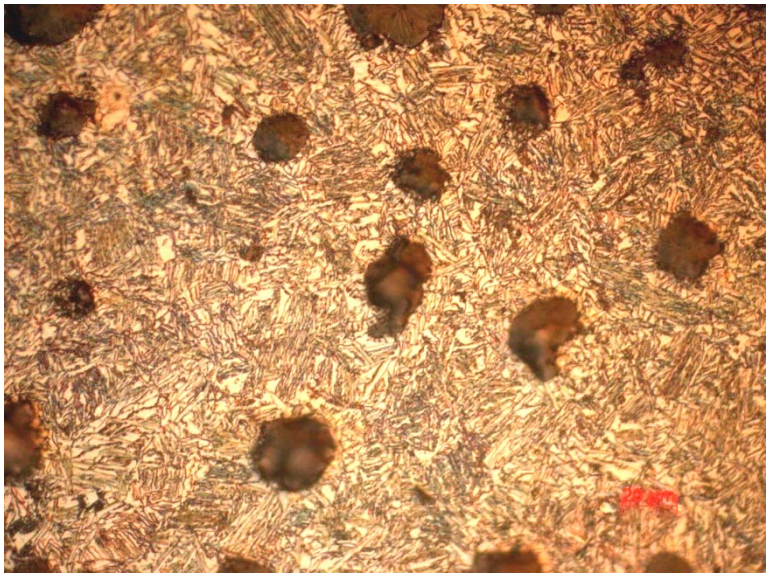

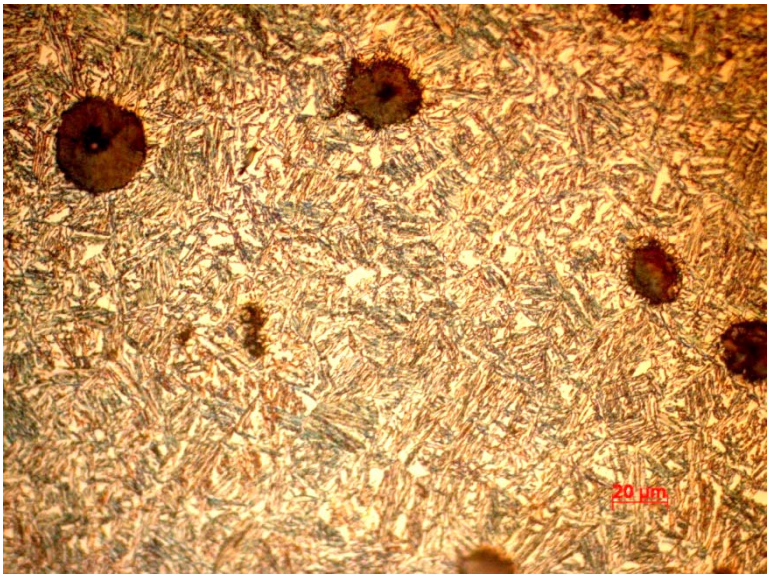
20 µm

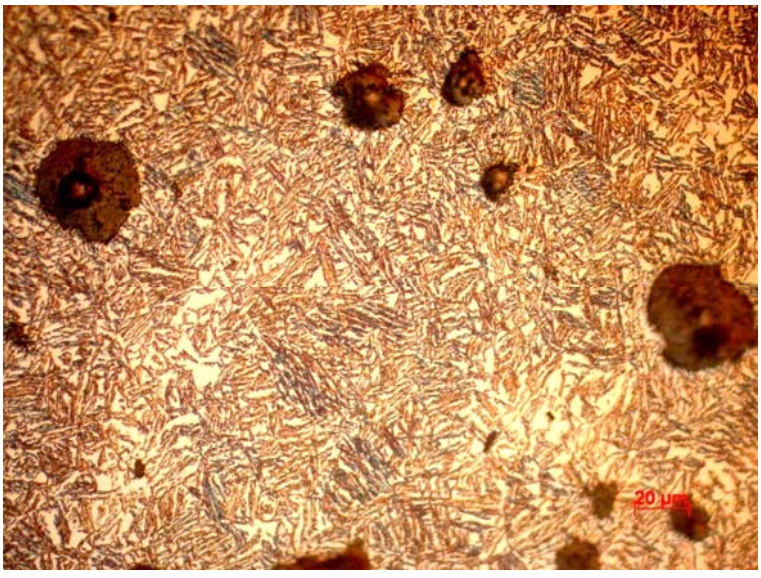
20 µm

Figure 7.4: magnification of ADI microstructure for different austenitization temperatures (respectively 840, 860 and 880 °C) for the same austempering temperature (400°C) of Alloy 1.

It was observed that the segregations aren't widespread, and also they are at least similar for the different austenitization conditions. Not shown here, the areas which delimited the cell boundaries have slightly different color compared to the bulk of the grain in the etched microstructure.

It could be concluded that the segregation are not extensive and the grain sizes are comparable for the samples carried out varying the austenitization temperature, which is the factor that control these aspects.

- **Nodularity, nodule count, nodule size**

In the table 7.1 are listed the nodularity, nodule count and nodule radius of all alloys in this work. Those parameters were measured in different positions for each sample (inner, middle and outer) in order to evaluate the variation of the graphite nodules along the ADI ring, an important factor to understand the fracture behavior.

Alloy	Sample	Nodularity (%)	Nodule count (n°/mm^2)	Nodule radius (µm)	Impact energy [J]
Alloy 1	880°C_360 °C_In	~ 81	~ 108	15,8 ± 0,5	70,9
	880°C_360 °C_Mid	~ 80	~ 90	14,3 ± 0,9	66,3
	880°C_360 °C_Out	~ 86	~ 125	14,5 ± 0,4	80,8
	880°C_385 °C_In	~ 88	~ 165	11,4 ± 0,1	90,1
	880°C_385 °C_Mid	~ 82	~128	11,1 ± 0,6	85,5
	880°C_385 °C_Out	~ 86	~ 167	10,9 ± 0,1	84,4

	880°C_400 °C_In	~ 85	~ 179	10,9 ± 0,7	94,6
	880°C_400 °C_Mid	~ 82	~ 140	10,4 ± 0,1	104,2
	880°C_400 °C_Out	~ 84	~ 178	11,0 ± 0,6	112,4
	840°C_400 °C_In	~ 86	~ 242	7,5 ± 0,1	112,0
	840°C_400 °C_Mid	~ 79	~ 53	7,9 ± 0,2	108,1
	840°C_400 °C_Out	~ 82	~ 186	6,9 ± 0,2	113,6
	860°C_400 °C_In	~ 83	~ 170	7,7 ± 0,1	121,0
	860°C_400 °C_Mid	~ 79	~ 59	8,1 ± 0,3	93,5
	860°C_400 °C_Out	~ 85	~ 169	7,3 ± 0,1	97,3
Alloy 2	840°C_400 °C_In	~ 82	~ 86	7,5 ± 0,2	97,8
	840°C_400 °C_Mid	~ 73	~ 41	7,2 ± 0,1	60,7
	840°C_400 °C_Out	~ 83	~ 66	7,4 ± 0,6	106,1
Alloy 3	840°C_400 °C_In	~ 85	~ 114	6,7 ± 0,3	113,6
	840°C_400 °C_Mid	~ 80	~ 59	7,3 ± 0,4	84,8
	840°C_400 °C_Out	~ 85	~ 96	7,0 ± 0,2	106,5

Table 7.1: nodularity, nodule count,nodule radius and impact energy for the ADIs studied.

As shown in table 7.1, the nodularity is higher than 80% for almost all the specimens. This is an important factor because the graphite nodule has a “micronotch” effect on the microstructure and can strongly affect the properties [13]. Higher nodularity means more graphite nodules of spheroidal shape and lower stress concentration factors as compared to other nonspheroidal shapes [13]. In addition, spheroidal nodules have less sites for the protrusion of graphite into matrix. This develops a less stress concentration at graphite/matrix interface.

The size of the nodules in the different samples is quite variable and can be noticed that for Alloy 1, for which the heat treatment was investigated, the sample with the biggest nodule size shows the smallest nodule count, and decreasing the nodule radius could be

seen an increase of nodule count, however when the nodule size becomes slightly different there isn't a relation between nodule count and nodule size.

Furthermore it can be noticed that, inside each kind of material (same alloy different heat treatment conditions as well), the nodularity and the nodule count in the middle part of the ring are lower than inner and middle parts. This might be due to the fact that inner part of the rings is the last one to solidify.
Finally, it can be seen that, for the three different alloys (different chemical composition) but same heat treatment conditions, the nodularity and nodule size are comparable, while the nodule count is higher for Alloy 1.

7.1.2. X-Ray analysis

By X-Ray Diffraction it was evaluated the amount of retained austenite (X_γ) and its carbon content (C_γ). The results are listed in the table 7.2.

There are two values of carbon content of retained austenite because it was measured according to two different references (respectively Roberts and Bayati). The carbon content predicted by Roberts is higher but, however, the different samples keep the same rank in the two calculation.

Alloy	Sample	Retained Austenite, X_γ (%)	Carbon content, C_γ (%)	
			Roberts	Bayati
Alloy 1	880°C_360 °C	29,6	1,87	1,72
	880°C_385 °C	24,5	1,85	1,69
	880°C_400 °C	22,6	1,86	1,71
	860°C_400 °C	26,0	1,84	1,68
	840°C_400 °C	20,9	1,90	1,74
Alloy 2	840°C_400 °C	32,5	1,90	1,74
Alloy 3	840°C_400 °C	34,6	1,82	1,66

Table 7.2: amount of retained austenite and its carbon content for the ADIs studied.

The first observation is that the carbon content range is slightly different for Alloy 1 (maximum value is 1,90 and the minimum is 1,82 for Roberts, 1,74 and 1,66 for Bayati). It might be due to the small difference between the austenitization temperature, which controls the carbon content of the matrix.

The amount of retained austenite increases when the austempering temperature decreases, for the samples austenitized at the same temperature (880 °C, Alloy 1). This is not in agreement with what asserted by the literature.

In the samples austempered at the same temperature (400 °C), it can't be noticed a relation with the variation of austenitization temperature, which controls the carbon content of retained austenite. In fact the value of carbon reaches the maximum at 840 °C.

Comparing the three alloys with different chemical composition but same austenitization and austempering temperatures, Alloy 1 shows the lowest amount of retained austenite but the highest percentage of carbon content, which leads to the stability of retained austenite. But the amount of retained austenite is noticeably higher in Alloy 2 and 3. The difference might be due to the different austenitization times (75 minutes for Alloy 1, 90 minutes for Alloy 2 and 3).

7.1.3. Porosity

The measure of porosity listed in table 7.3 shows that it's comparable for all the specimens studied. In fact the values of the mean porosity are slightly different for all the samples. The mean porosity is less than 1% for all the alloys, that means porosity is not, at least, the most important defect for the materials studied; the most dangerous defects are dross shrinkages, than porosities.

Alloy	Sample	Mean Porosity	
Alloy 1	880°C_360 °C_In	0,17	0,13 ± 0,07
	880°C_360 °C_Out	0,08	
	880°C_385 °C_In	0,27	0,28 ± 0,03

	880°C_385 °C_Out	0,30	
	880°C_400 °C_In	0,88	0,83 ± 0,07
	880°C_400 °C_Out	0,78	
	840°C_400 °C_In	0,63	0,79 ± 0,22
	840°C_400 °C_Out	0,95	
	860°C_400 °C_In	0,69	0,69 ± 0,00
	860°C_400 °C_Out	0,69	
Alloy 2	840°C_400 °C_In	0,32	0,26 ± 0,09
	840°C_400 °C_Out	0,20	
Alloy 3	840°C_400 °C_In	0,11	0,26 ± 0,21
	840°C_400 °C_Out	0,41	

Table 7.3: porosity determined for ADI samples studied.

7.1.4. Hardness

In the table below are listed the values of hardness (Vickers) measured for the different alloys studied.

Alloy	Sample	Vickers Hardness (HV)	
Alloy 1	880°C_360 °C_In	351,6 ± 4,9	366,2 ± 16,9
	880°C_360 °C_Out	380,8 ± 10,2	
	880°C_385 °C_In	355,2 ± 29,7	341,0 ± 25,4
	880°C_385 °C_Out	326,8 ± 10,1	
	880°C_400 °C_In	314,7 ± 15,3	308,0 ± 14,3

	880°C_400 °C_Out	301,2 ± 9,2	
	840°C_400 °C_In	291,6 ± 5,0	298,0 ± 9,9
	840°C_400 °C_Out	304,4 ± 9,5	
	860°C_400 °C_In	295,5 ± 7,7	314,4 ± 23,4
	860°C_400 °C_Out	333,3 ± 17,4	
Alloy 2	840°C_400 °C_In	284,6 ±12,1	285,1 ± 5,8
	840°C_400 °C_Out	285,6 ± 6,5	
Alloy 3	840°C_400 °C_In	265,5 ± 5,8	267,1 ± 7,1
	840°C_400 °C_Out	268,6 ± 7,1	

Table 7.4: values of hardness for ADIs tested.

In Alloy 1, for which different austenitization and austempering conditions were studied, the hardness shows an increase when the austempering temperature decreases. This is in agreement with the literature data , which shows an enhance of strength (with a optimum combination of ultimate tensile strength, yield strength and hardness) when the austempering temperature decreases. Anyway the variation between the different austempering temperatures is small, so the hardness values are comparable into the same range considering the standard deviation.
The variation of austenitization temperature doesn't show the same effect.

In the alloy with different chemical composition but same austenitization and austempering conditions the values of hardness are slightly different, and it's not possible to predict a relation between them.

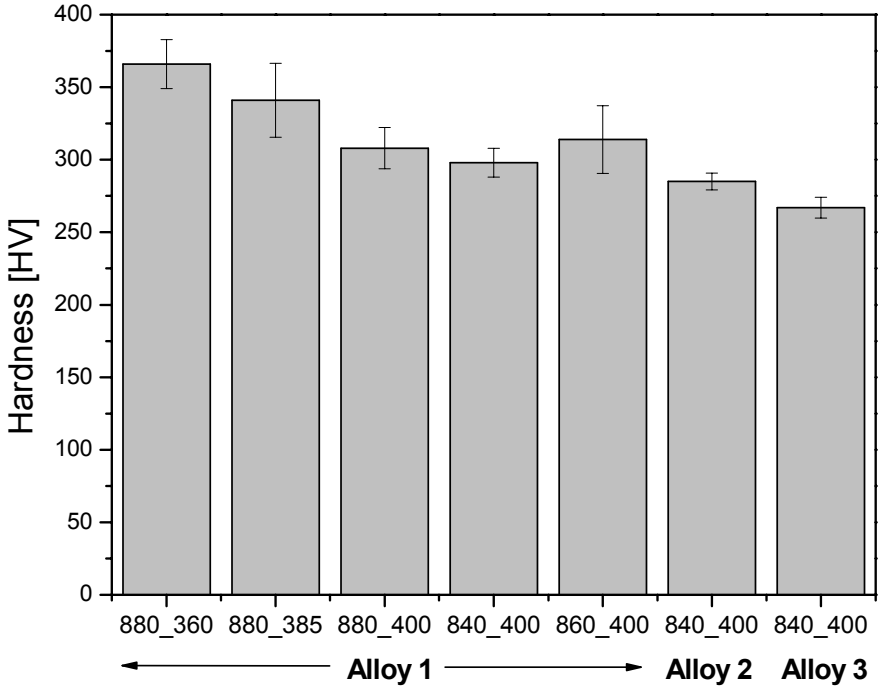

Figure 7.5: hardness and related standard deviation in ADIs.

7.1.5. Carbides study

An investigation about the presence of carbides was carried out in the ADIs studied.

Alloy 1 is the material with the smallest amount of alloying elements in this study, so it is supposed to be the alloy with lowest carbide formation.

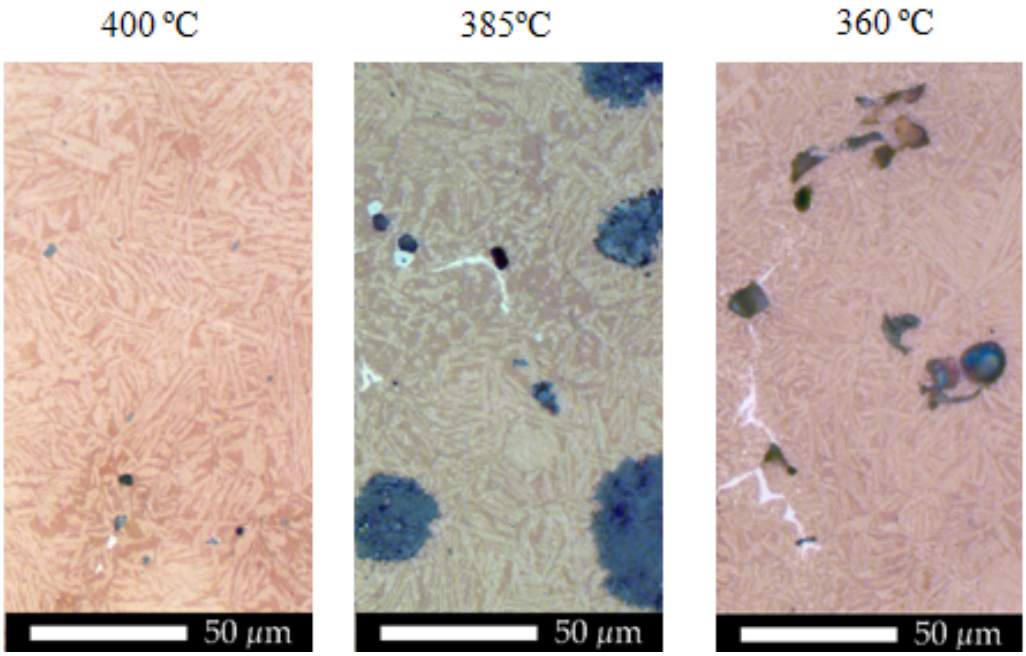

Figure 7.6: carbides in Alloy 1 for different austempering temperature.

From Figure 7.6, a slightly increase of amount of carbides can be observed when the austempering temperature decreases from 360 to 400 °C in Alloy 1. However, since the percentage of carbides is very low, it wasn't possible to quantify the amount of carbides for the different heat treatment conditions in Alloy 1.

In all the cases, the carbides formation occurs in the cell boundary, where the alloying element segregate during the solidification of the material.

On the other hand, Alloy 2 is the material with highest percentage of alloy elements, compared to Alloy 1 and 3. It means that a larger amount of carbides should be expected.

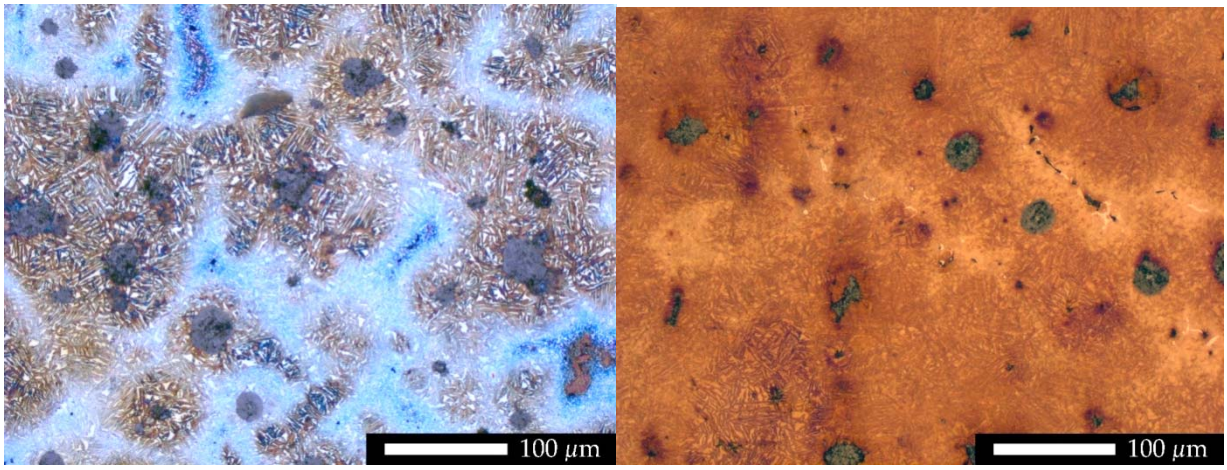

Figure 7.7: etched and heat tinted microstructure of Alloy 2.

The microstructure in Figure 7.7 shows the presence of the cell boundary segregation in Alloy 2. It can be seen also the formation of carbides at the cell boundary, they are present as white spots or for flattened shape, as it can be noticed on the heat tinted microstructure on the right.

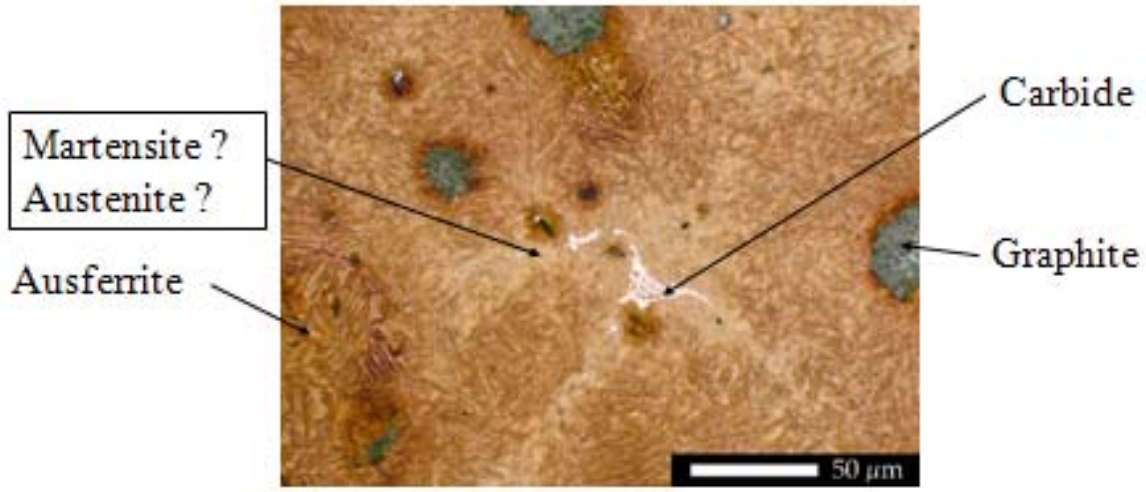

Figure 7.8: heat tinted microstructure of Alloy 2.

Figure 7.8 shows the presence of carbides in higher magnification. It is also possible to see bright areas that could be indentified as martensite or low carbon austenite. It's very hard, also for an expert eye, to distinguish which phase it is, but, if it is low carbon austenite, it may transform to martensite when a load is applied, due to its instability caused by its low carbon concentration.

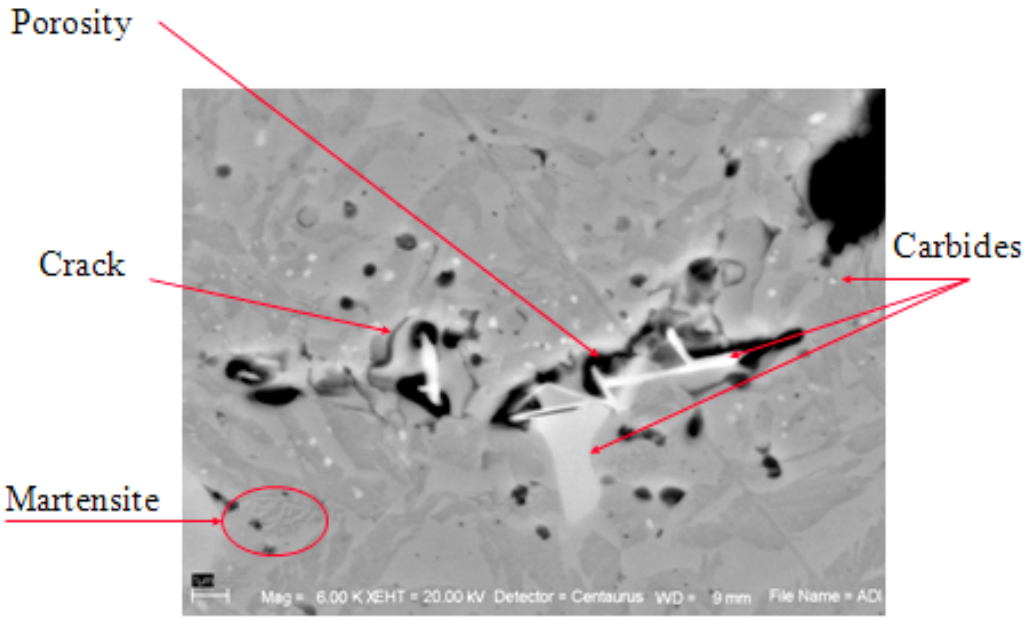

Figure 7.9: some defects in Alloy 2 microstructure revealed by SEM.

As shown in Figure 7.9, the carbide (white) is surrounded by porosity, which may be a crack initiation site. Also in Figure 7.9 a small area that could be martensite could also be seen.

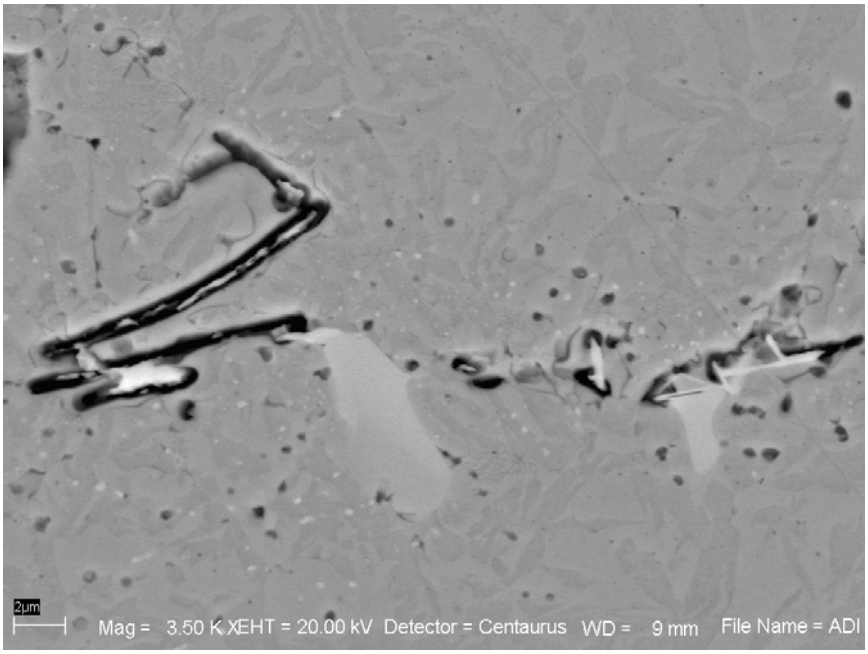

Figure 7.10: carbide in Alloy 2 revealed by SEM.

Also in Figure 7.10 it can be noticed porosity along the boundary of the carbide. Besides the EDS analysis carried out for some carbides detected in the microstructure, has

revealed the presence of Molybdenum as main element as well as traces of Titanium and Vanadium (Figure 7.11).

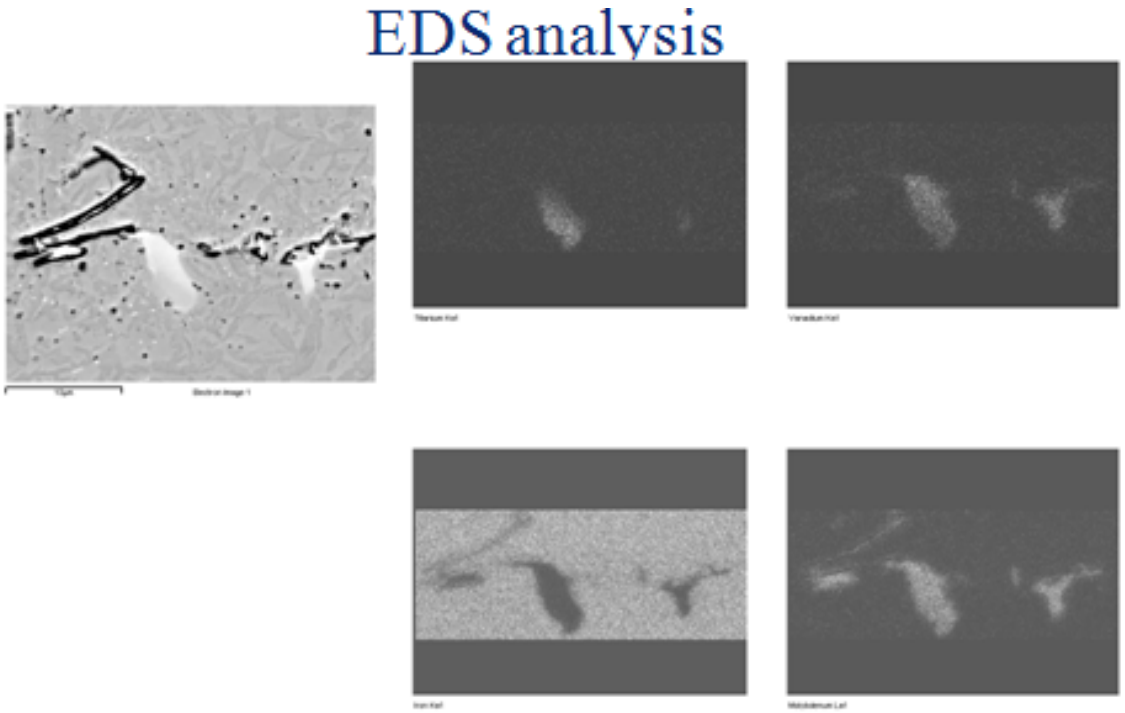

Figure 7.11: EDS analysis of the carbide showed on figure 5.

Alloy 3 has also a small amount of carbides, which is expected of the alloying elements in this alloy are less than in Alloy 2, but slightly higher than in Alloy 1.

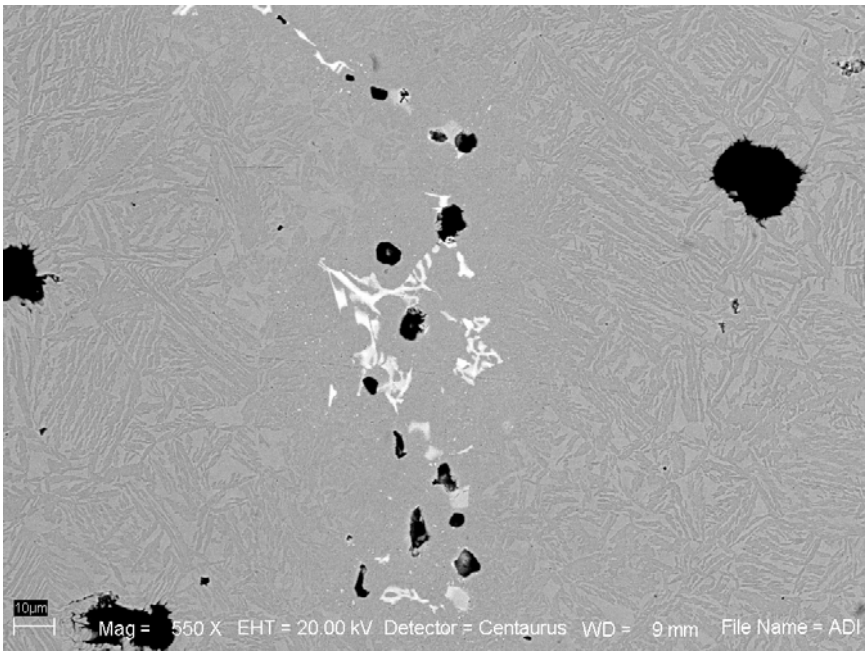

Figure 7.12: carbide in Alloy 3 revealed by SEM.

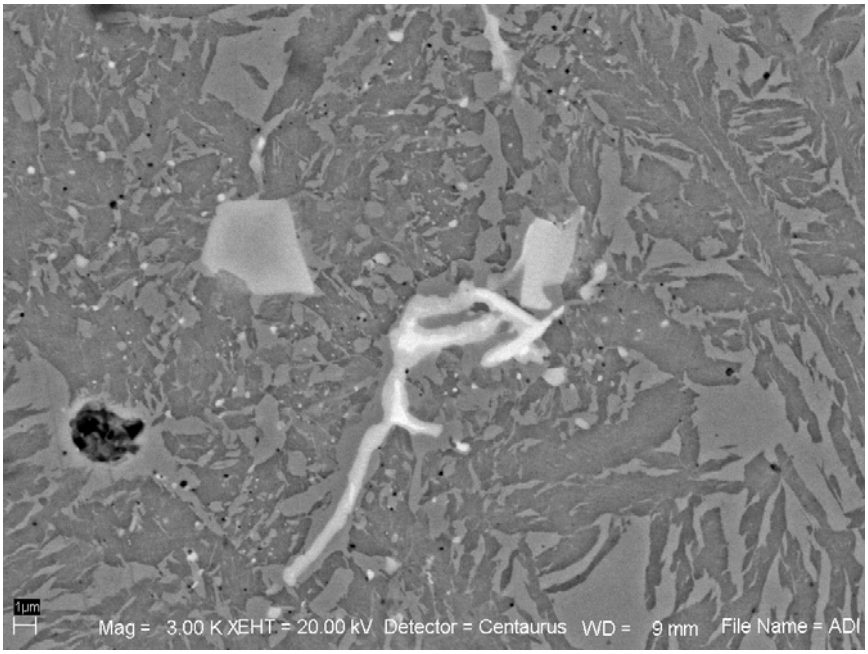

Figure 7.13: carbide in Alloy 3 revealed by SEM.

In Figure 7.12 and 7.13 it can be seen two examples of carbides formation in Alloy 3. As for Alloy 2, the EDS analysis has revealed the presence of Molybdenum as main element in the composition of the carbides and traces of Vanadium and Titanium.

In Figure 7.12 it is also possible to see the probable presence of martensite in the microstructure, noticeable by the grey areas around the carbides, in which it's difficult to see the needles of ausferrite. However, the XRD analysis used for the austenite amount and carbon concentration (spectra not shown here) had <3%martensite for all the alloys studied.

An estimate of the amount of carbides was carried out by thermodynamical simulation with J-MatPro software. It was found that the amount of carbides is about 0,1%wt for Alloy 3 and 0;35% for Alloy 2. However, since it is only a simulation, it must be used carefully. It provides a more accurate estimate than point counting, which wasn't possible to carry out for Alloy 3. However, the investigation by point counting was carried out for Alloy 2 and it revealed a maximum percentage of carbides of 0,5%, which is consistent with the simulation.

7.2. Impact test

The impact energies for all the ADIs materials studied are showed in the following graphics (Figures 7.14 and 7.15).

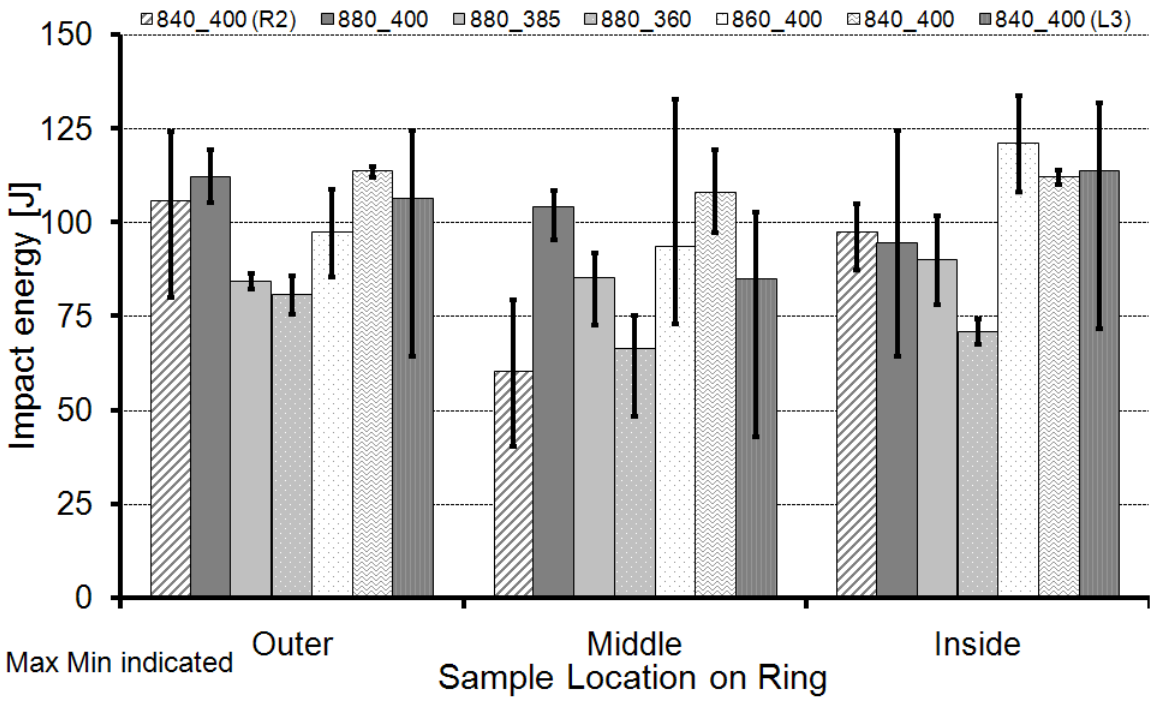

Figure 7.14: impact energies of all the materials shared by sample location on ring, maximum and minimum values are indicated.

In Figure 7.14 it can be seen a big scattering around the average values for many samples. However it can be noticed, in general, lower impact energy for the samples located in the middle of the ring. This is due to the “microstructure quality” of the material in that location. In fact, the middle part of the ring is the last one to solidify so the segregation of alloy elements is higher than the inner and outer part of the ring, so probably the concentration of carbides and defects is more elevated. The presence of defects lead to decrease the impact properties of ADI, and probably it is also the cause of the big scattering shown by the impact energies.

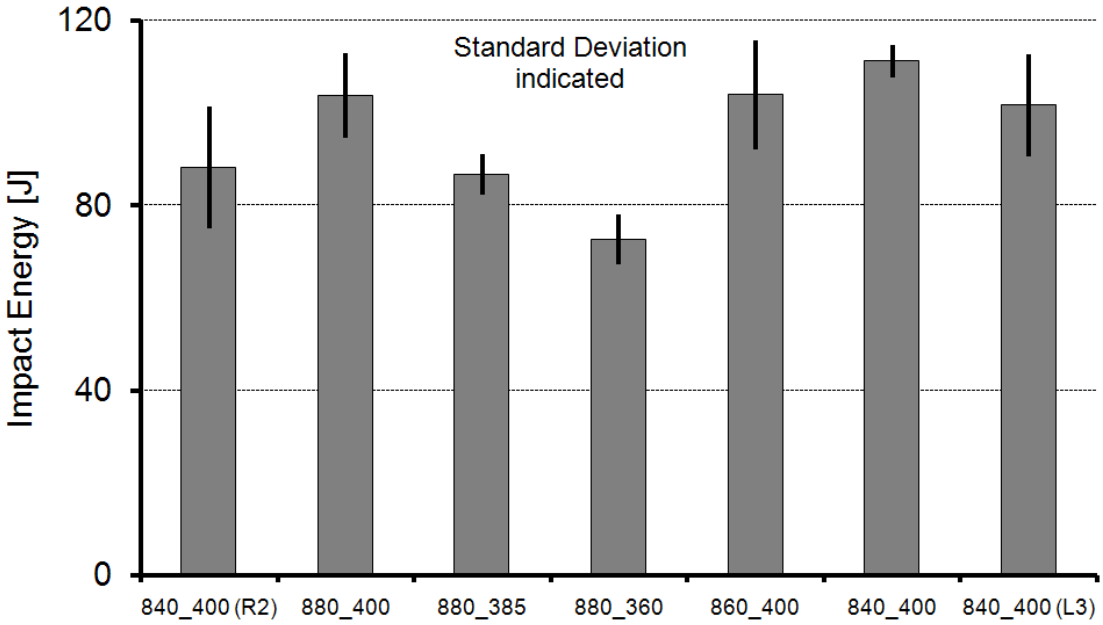

Figure 7.15: average impact energies and standard deviations for all the materials studied.

The graphic in Figure 7.15 shows the average values of impact energy between the different locations on the rings. It can be noticed an increase of the impact energy when the austempering temperature increases. In fact for Alloy 1, which the industrial ADI heat treatment was studied, the impact energy raises from samples austempered at 360 °C to ones austempered at 400 °C. On the other hand, the specimens austenitized at different temperatures don't show a big variation. However, the samples austenitized at 840 °C and austempered at 400 °C show at least the highest average value for the same class of alloy, but, considering the standard deviation, the impact energies of the samples austenitized at the same temperature are similar.

Comparing alloys with different chemical composition but with the same heat treatment conditions, it can be seen how Alloy 1 shows the highest impact energy. Alloy 3, considering the standard deviation, has slightly worse impact properties, whereas Alloy 2 has the lowest impact energy.

These results are expected, in fact Alloy 2 is the material with more alloy elements, which promote the formation of carbides that impair the impact properties of ADI, as discussed before. Alloy 1 and 3 have slightly different chemical composition and showed lower amount of carbides than Alloy 2.

- **Effect of the graphite nodules**

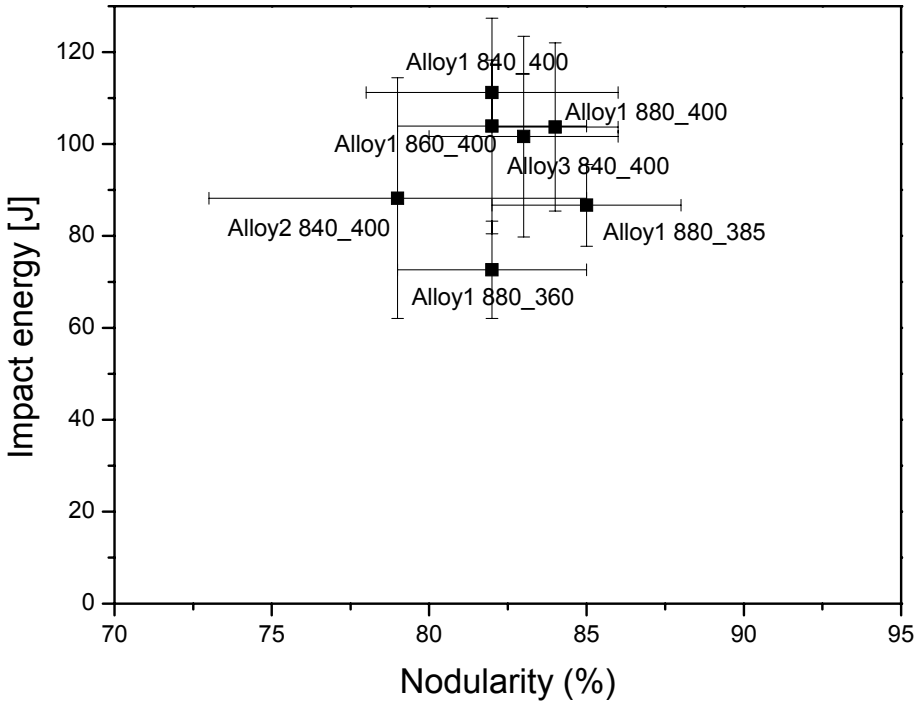

Figure 7.16: relation between impact energy and nodularity for ADIs studied.

As shown in Figure 7.16, the nodularity affects the impact energy, in fact increasing the nodularity, the “notch effect” inside the material is lower and the impact energy increases. However, the values of nodularity of the materials studied are comprised in a small range, so it can’t be seen a clear relation between nodularity and impact properties.

However, it was observed that the nodularity doesn’t depend on the heat treatment, neither of the composition. The main factor is the cooling rate during the casting. It can be observed in Figure 7.17, the variation of nodularity in the ring location for Alloy 1, for which the ADI heat treatment was studied: the middle part of the ring is the one which the cooling is more slowly and the values of nodularity are lower, independently of the heat treatment. In fact there is no relation between nodularity and heat treatment conditions, but in each sample, the nodularity shows the lowest value in the middle part of the ring.

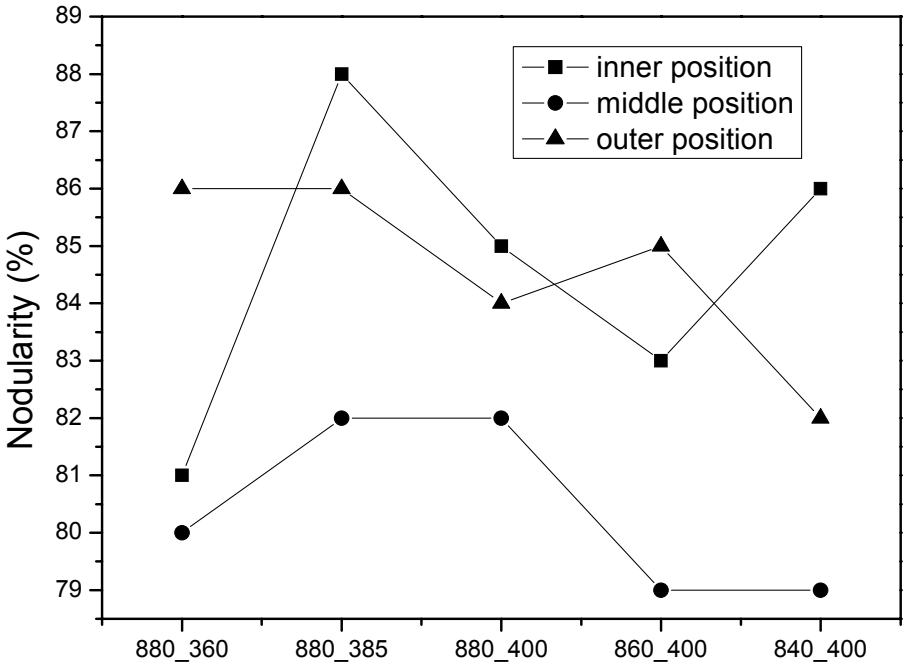

Figure 7.17: variation of nodularity in the ring location in Alloy 1.

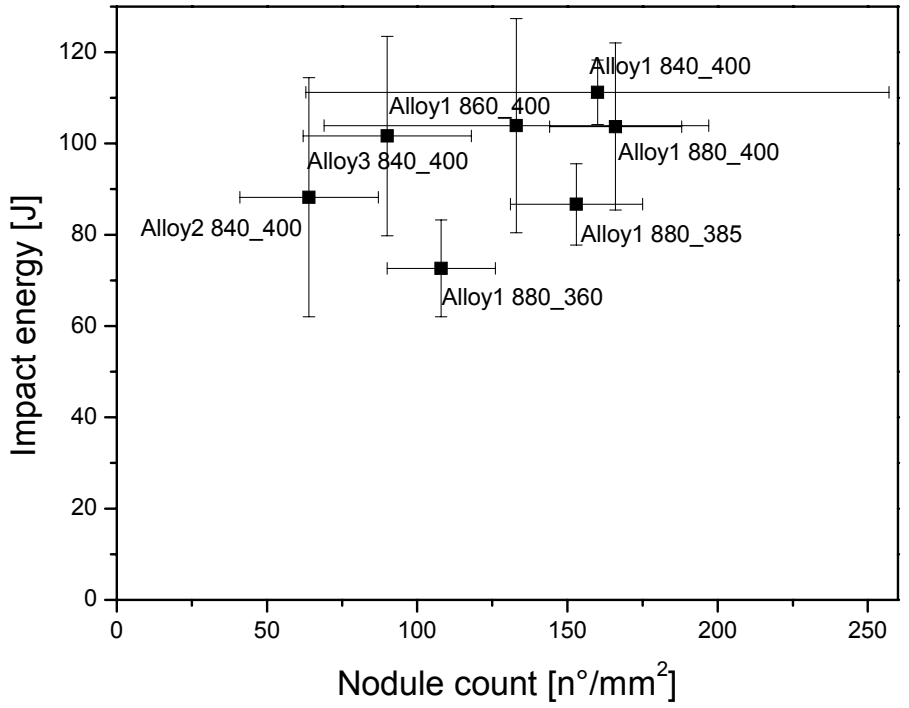

Figure 7.18: relation between impact energy and nodule count for ADIs studied.

It can be noticed in Figure 7.18 that the impact energy increases when the nodule count increases. The way to optimize the number of nodules is determined by the composition and the casting before the heat treatment.

As shown in the previous paragraph, the alloy that shows the highest number of graphite nodules is Alloy 1, which it's also the material that shows higher impact properties.

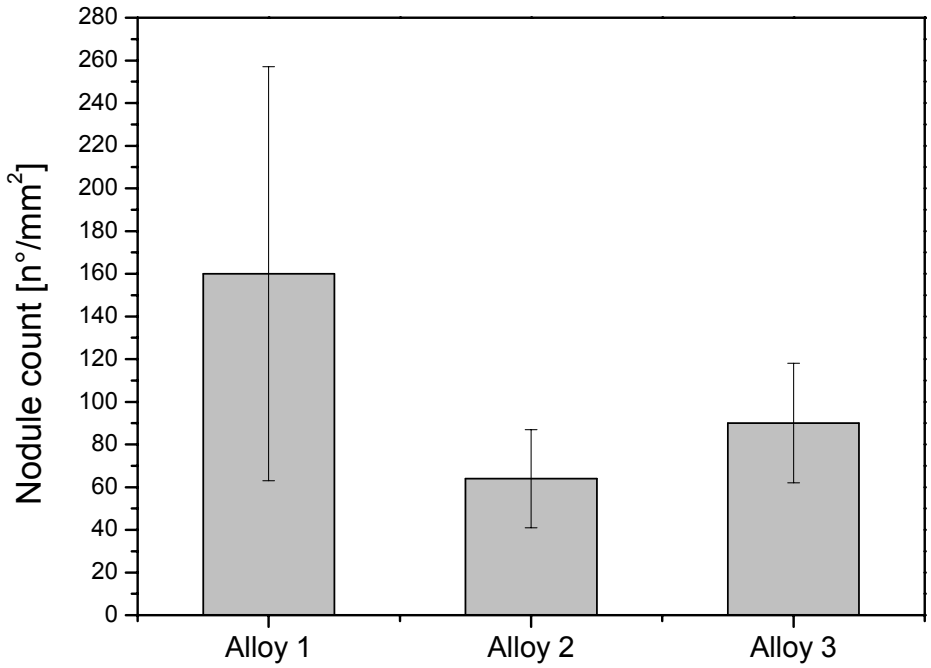

Figure 7.19: nodule count in the different alloys for the same heat treatment conditions.

The alloy element that promotes the formation of nodules of graphite is the silicon. The silicon promotes graphite formation, decreases the solubility of carbon in austenite, increases the eutectoid temperature and inhibits the formation of bainitic carbides [1]. The most important factor to achieve high nodule count is to be near to the eutectoid point, in order to increase the inoculation [1].

Moreover has been observed that the austenitization temperature or the austempering temperature do not affect to the number of nodules. It could be concluded that, in order to obtain good impact properties, a composition that promotes the formation of graphite nodules must be selected, due to the subsequent heat treatment will not change this parameter.

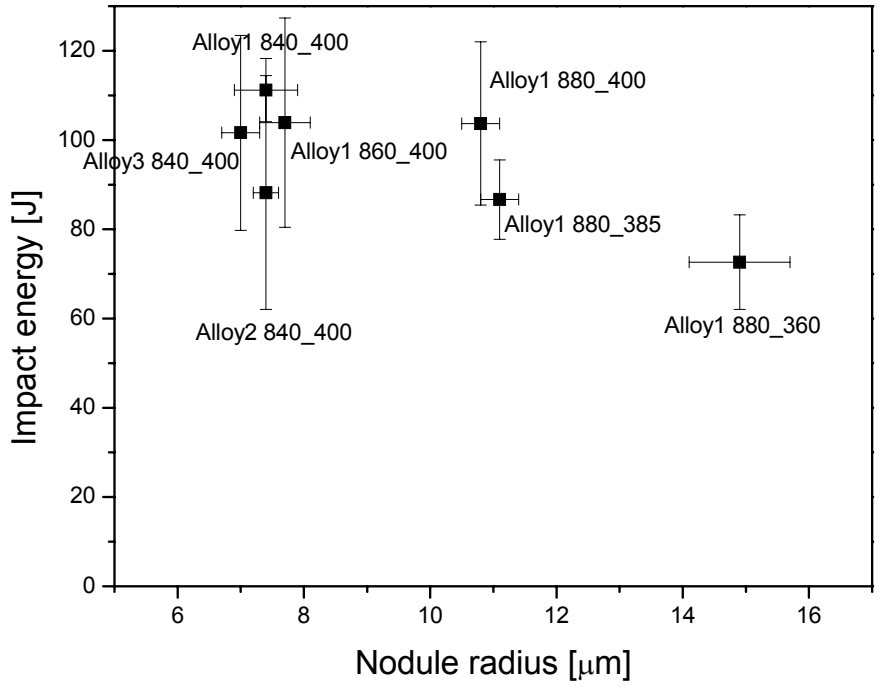

Figure 7.20: relation between impact energy and nodule radius for ADIs studied.

As shown in Figure 7.20, another important factor for the impact properties is the size of the graphite nodules. The results show an increase of impact energy when the size of the graphite nodules decreases.

Moreover, it can be observed that the austenitization temperature is connected with the size of the nodules. As shown in Figure 7.21, increasing the austenitization temperature, the nodule size increases, for the sample austempered at the same temperature in Alloy 1. This result is not expected. In fact, the austenitization temperature should slightly affect the nodule size [1], and, moreover, in the opposite way [1]. So, probably, the growth of nodule radius when the austenitization temperature increases, is only a particular case of the samples studied.

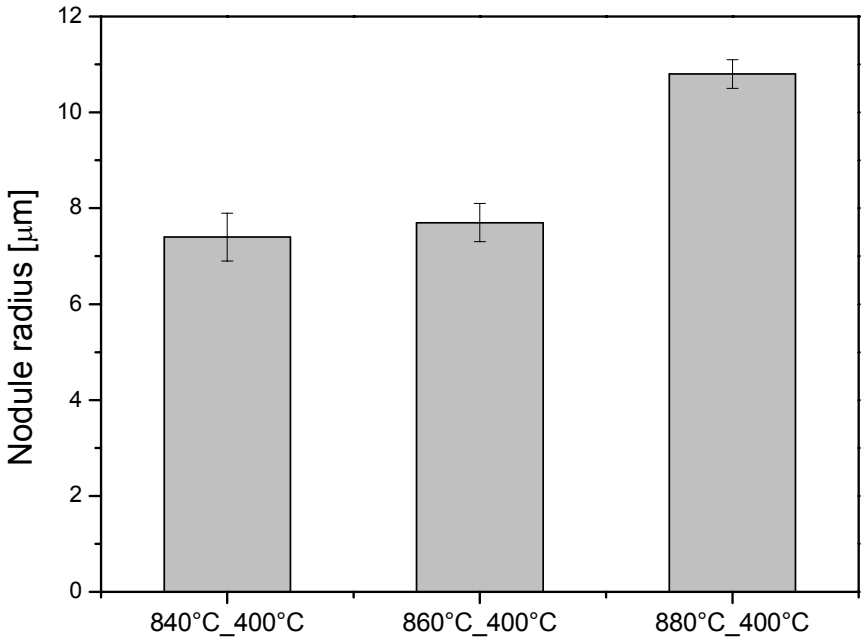

Figure 7.21: radius size for samples austenitized at different temperatures but austempered at same temperature (Alloy 1).

As shown in Figure 7.22, in the samples austempered at 400 °C, the nodule size is smaller. They also show the higher impact energy, so it can be concluded that the nodule size is an important factor for the impact properties, which increase when the nodule size decreases.

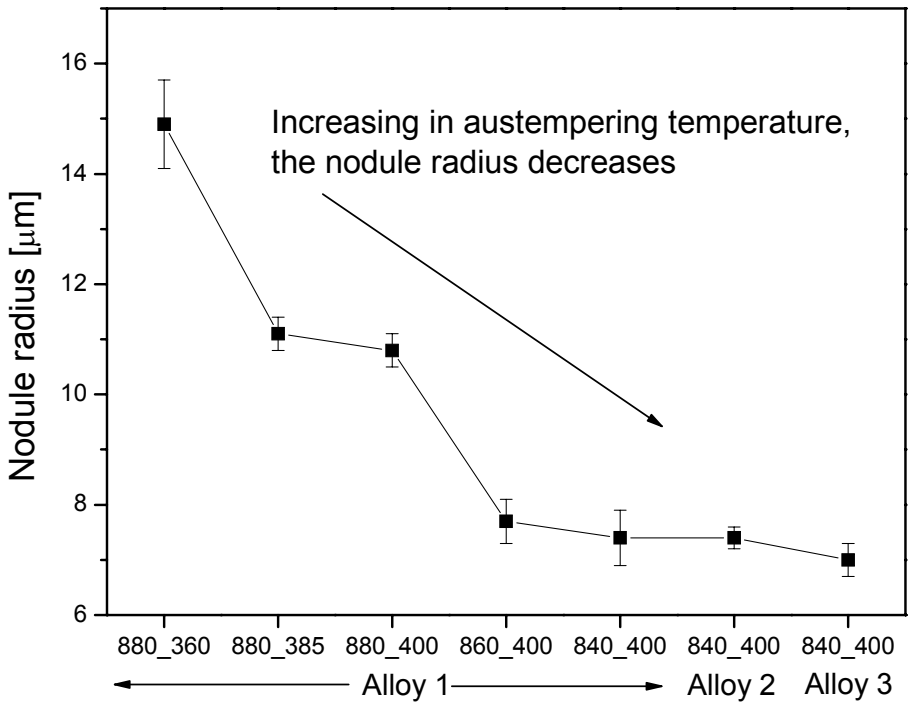

Figure 7.22: variation of nodule size for different heat treatment conditions.

- **Effect of retained austenite**

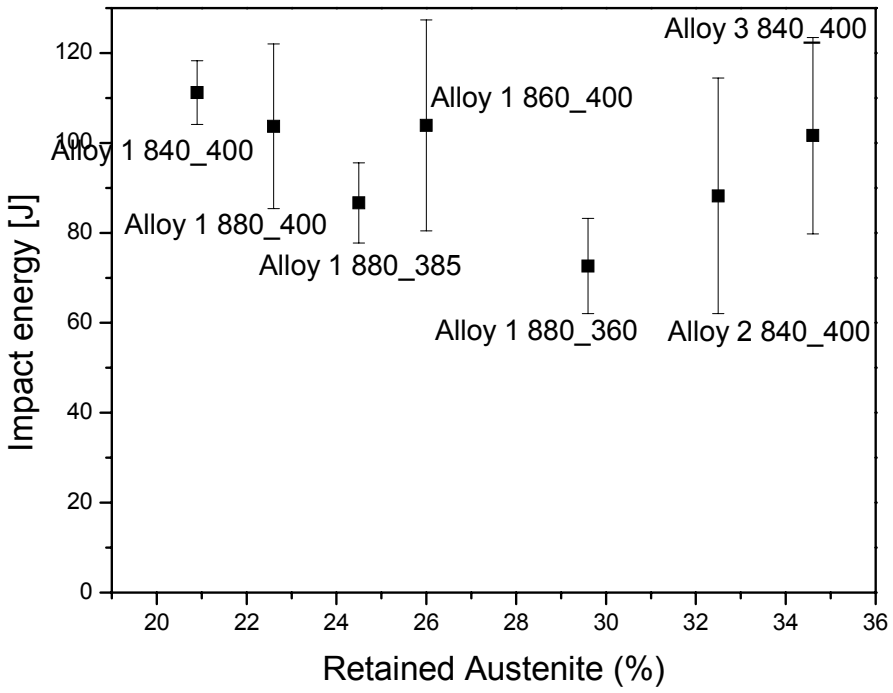

Figure 7.23: relation between impact energy and amount of retained austenite for ADIs studied.

The amount of retained austenite is another important factor, in particular for the fracture toughness of ADI, as explained in the literature review.

In this study, as shown in Figure 7.23, there is not a clear relation between impact properties and amount of retained austenite. In fact, for instance, the sample with the lowest amount of retained austenite (Alloy 1 austenitized at 840 °C and austempered at 400 °C) is the one which has the highest impact energy (at least considering the average value). However, Alloy 3 shows the highest amount of retained austenite as well as elevated impact energy.

It could be concluded that, probably the effect of the graphite nodules affects more than the amount of retained austenite, in the ADIs studied.

➢ **Fractographic analysis**

An investigation of the surface of the failed samples after the impact test was carried out by Scanning Electron Microscope (SEM). It was analyzed the fracture surface of the samples which showed higher and lower impact energies.

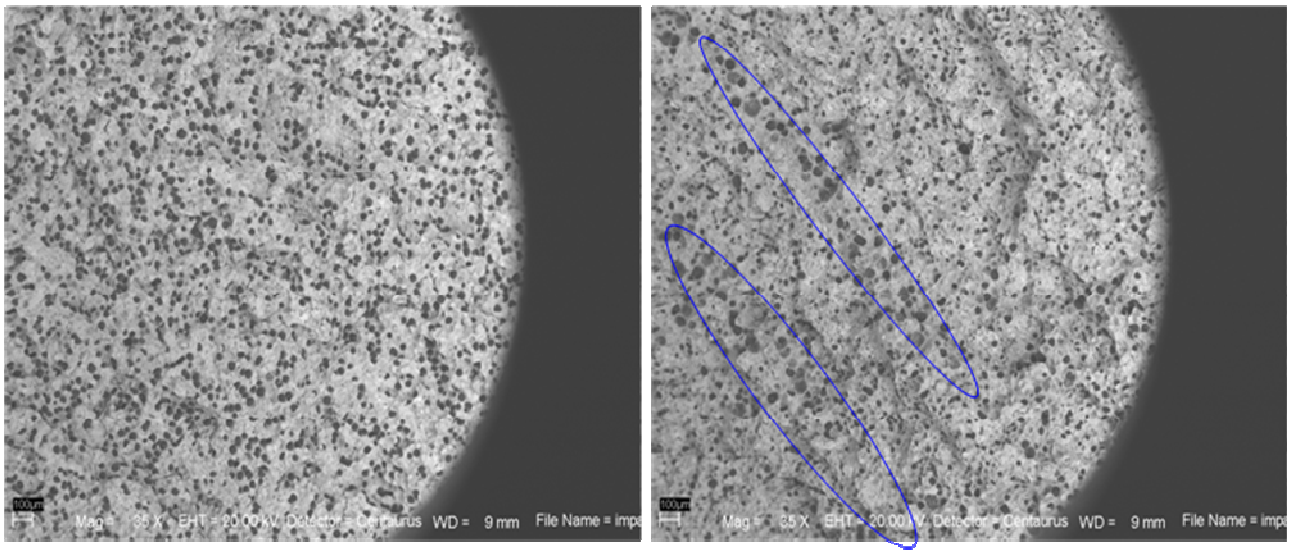

Figure 7.24: comparison between sample with higher and lower impact energy respectively.

It can be noticed in Figure 7.24 that the sample with lower impact energy (on the right), shows graphite nodules aligned in a row (pointed out by the blue ovals in the picture). That doesn't appear in the fracture surface of the sample with higher energy. In Figure 7.25 it can be observed tha the cleaved surfaces are fingerprinted by the ausferrite structure, which means that the fingerprint for Alloy 1 austempered at 400°C was wider and deeper. In Figures 7.26 and 7.27 evidence of graphite nodules debonding form the matrix can be seen after the impact tests, which evidently was also the dominant mode of fracture in the FCGR experiments. Furthermore, in Figure 7.28 the crack propagation at the cell/grain boundary is seen. From these diagrams, it can be concluded that the crack path preferentially intersects graphite nodules, and if the distance between the nodules are small and the nodules aligned, the crack will propagate easily and the impact energy will be low.

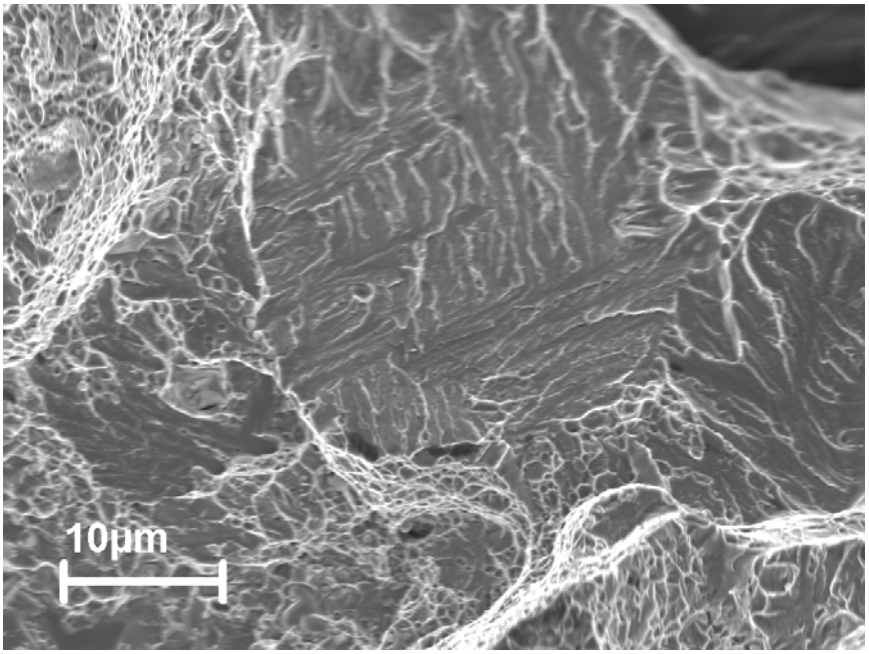

Figure 7.25: plastic deformation in the fracture surface.

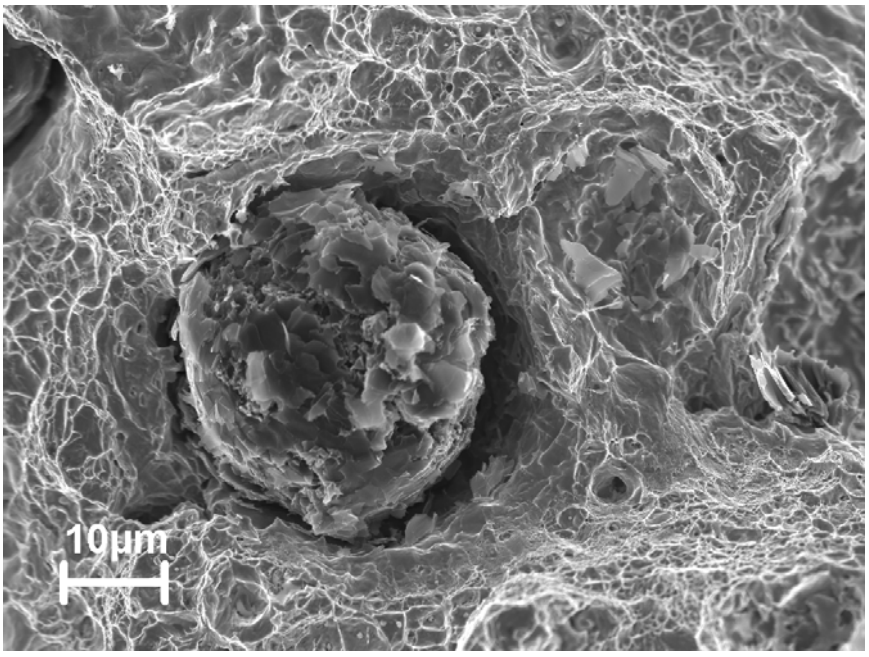

Figure 7.26: decohesion of a graphite nodule.

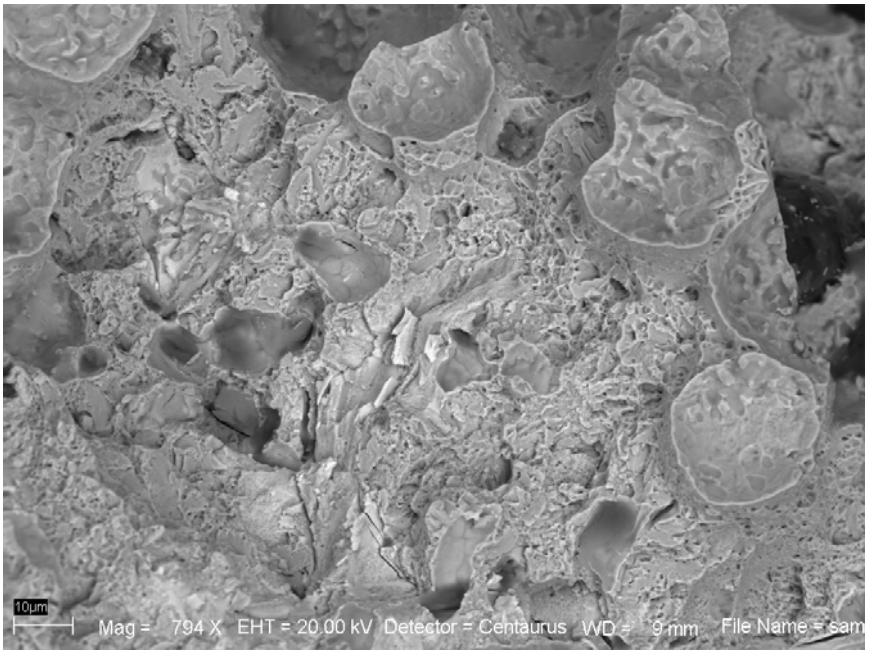

Figure 7.27: the debonding of the graphite nodules.

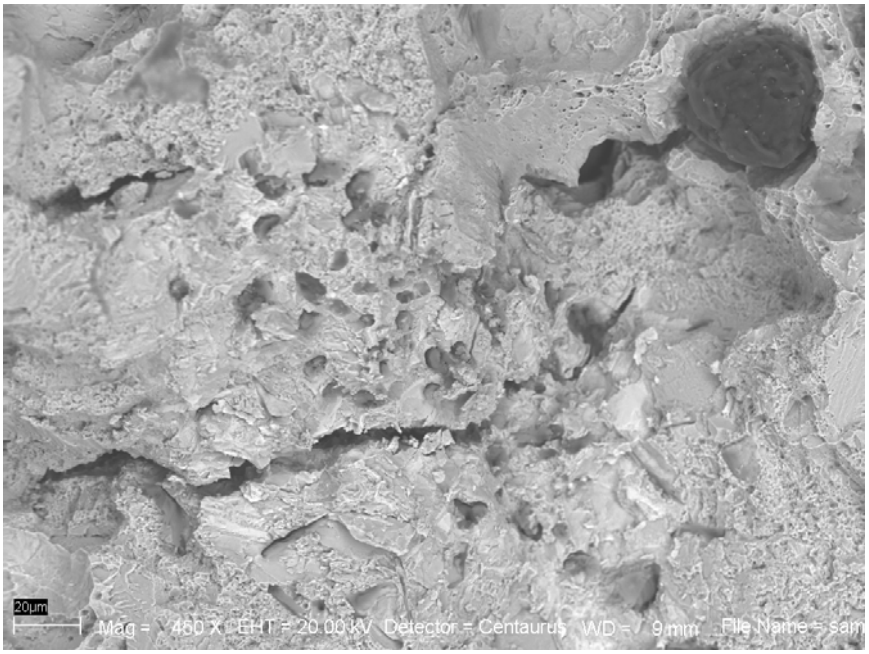

Figure 7.28: crack propagation in the cell/grain boundary.

7.3. Fracture mechanism analysis

The fracture mechanism of ADI was investigated performing a tensile test on the Scanning Electron Microscope (SEM). The behavior of the material when the load increase was study, analyzing the sites of nucleation of the crack and its propagation.

The behavior of the material is shown in Figure 7.29.

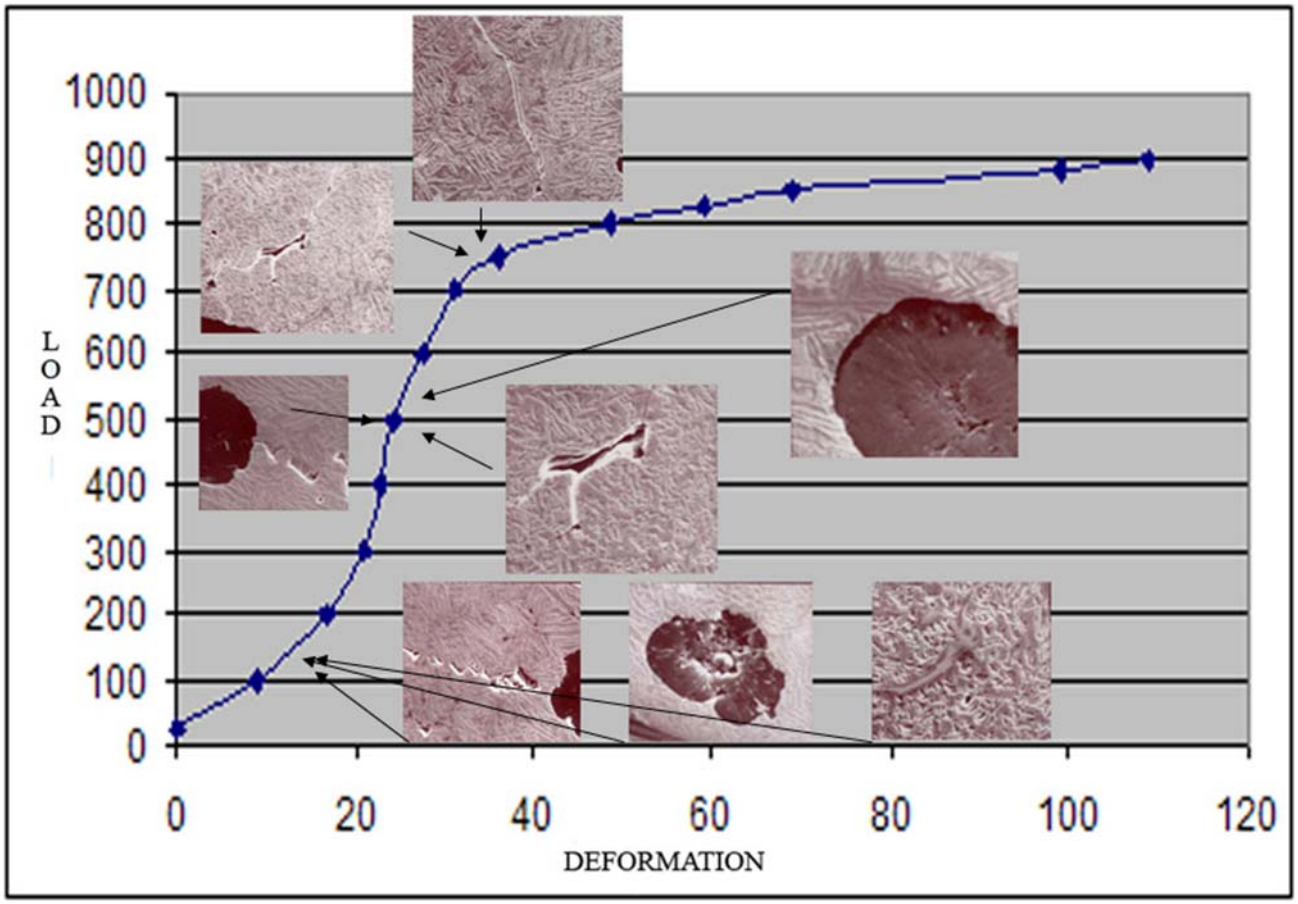

Figure 7.29: crack behavior in the load-deformation diagram.

It was observed that the nucleation of the cracks occurs on the defects of the material, as pores or carbides mainly, but also due to the decohesion at the interface between matrix and graphite nodules.

In Figure 7.30, it's shown an example of crack nucleation on a pore. It could be noticed, spotlighted with the green circle in the picture, the presence of carbide.

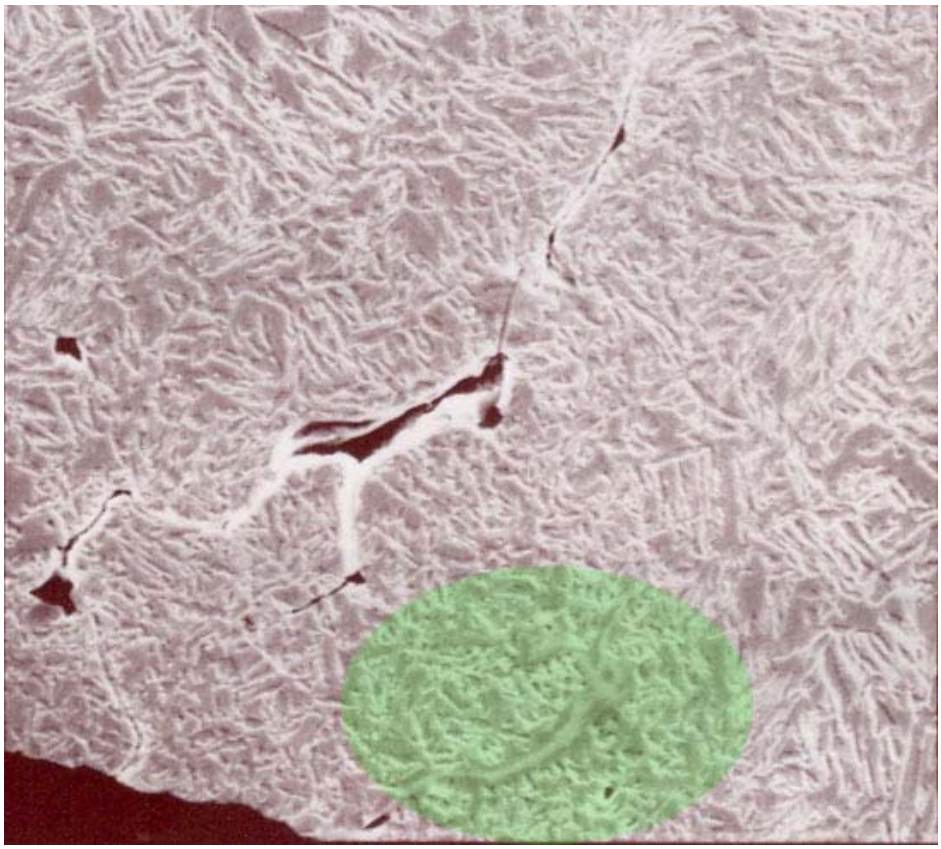

Figure 7.30: example of crack nucleation in a pore.

In this case the crack prefers to nucleate on the pore instead of the carbide, but it's only a case, it can't say as a general behavior.

Furthermore, the propagation of the same crack is shown in Figure 7.31. It can seen that the crack propagated along the grain boundary, highlighted with the red line. In this case the crack prefers to propagate and probably join other cracks, along the grain boundary instead of join the carbide shown in the picture before. This behavior could be due to the less toughness of the cell boundary, where the segregations takes place, than the matrix of the material, consists of retained austenite and needles of ausferrite.

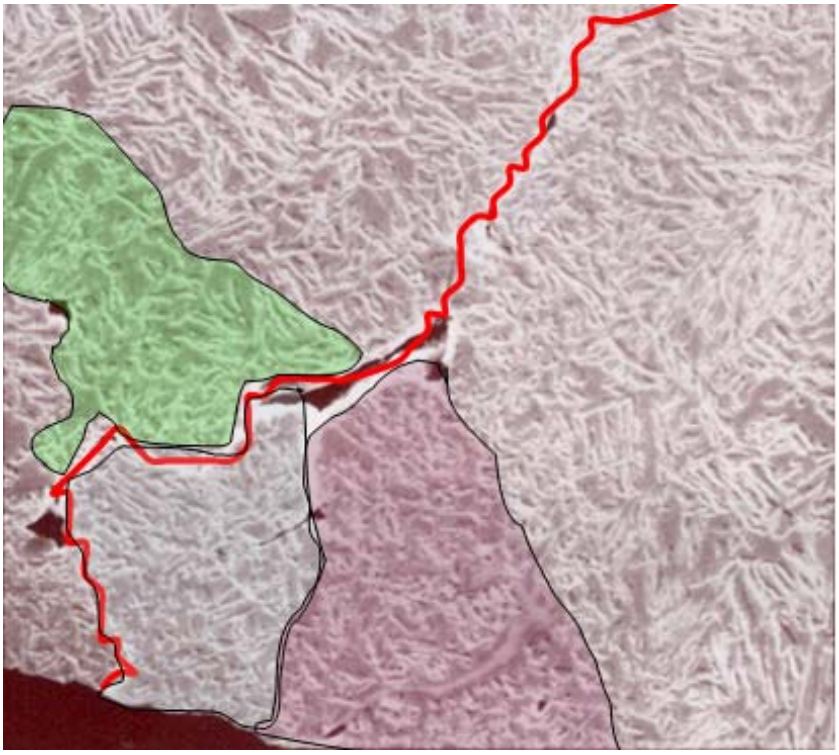

Figure 7.31: example of crack propagation.

On the other hand, in the literature [17] it is asserted that carbides are the main responsible of crack initiation. In this study it was found that cracks could be occur caused by different kind of defects, but the porosity was discovered to be the most dangerous crack initiator.

Another site of crack nucleation is the matrix/graphite nodule interface. In Figure 7.32 is shown the decohesion that occurs, in Figure 7.33 a crack is propagating from a nodule.

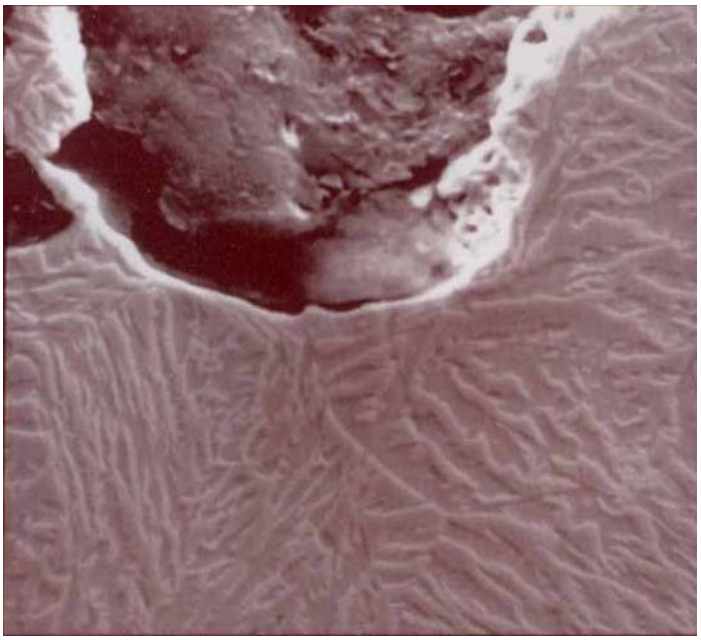

Figure 7.32: decohesion of the graphite nodule.

It can be noticed that a large nodule size leads the formation of voids due to the decohesion of graphite nodules as well as induced stress concentration fields. More deformation would take place in the area near the graphite nodules which promote the formation of cracks extending from the nodules. So it can be concluded that the crack initiation should be easier as larger is the nodule size.

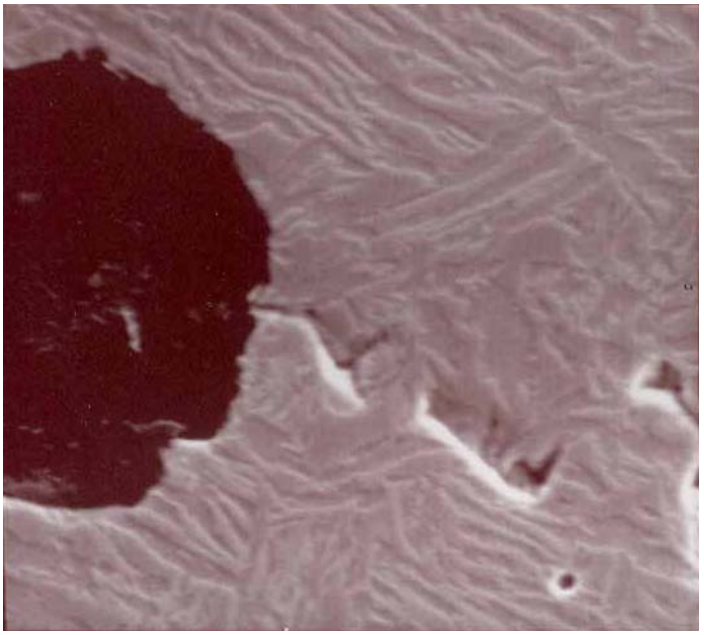

Figure 7.33: crack propagation from the graphite nodule/matrix interface.

It can be affirmed that the preferential crack path is between two neighboring nodules, and the crack growth would be faster as closer are the two nodules. However, the growth can take place along the austenite/ferrite interface or cut the ferrite laths. It's very hard to assert which is the easiest path for the crack growth because it was found that it depends on the orientation of the ferrite laths. If they are oriented perpendicularly with the direction which the load is applied, the ferrite laths might be the favourite path. On the other hand, in this work, a preliminary XRD investigation was carried out on failed samples of ADI, and it revealed a big amount of ferrite on the fracture surface. This supports the theory for what the crack growth occurs along interface austenite/ferrite, but this should be investigated further.

7.4. Fatigue Crack Growth Rate test

The Fatigue Crack Growth Test allow to measure the variation of crack length (a) in relation to the number of cycles passed during the test, as described in the experimental procedure chapter. By that curve it was possible to evaluate the fatigue crack growth rate (da/dN), expressed as crack extension per cycle of loading, and the stress intensity factor range (ΔK) is the variation in stress intensity factor in a cycle: the results achieved are shown in the following paragraph.

The graphic in Figure 7.34 shows the comparison of the fatigue crack growth behavior of Alloy 2 and Alloy 3 for the load case R = -1.

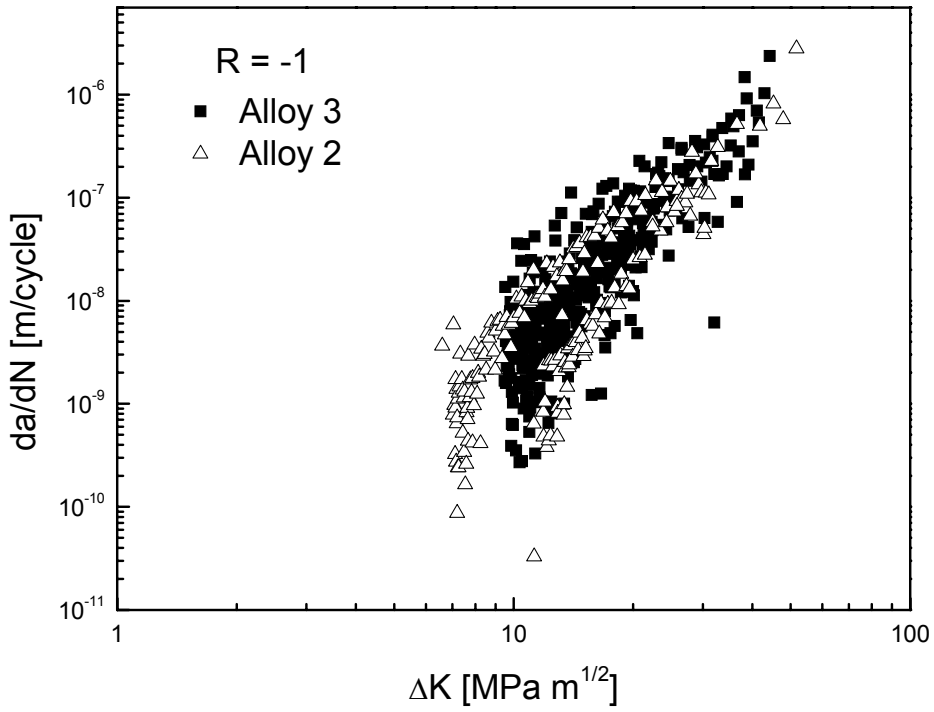

Figure 7.34: comparison of fatigue crack growth behavior of Alloy 2 and 3 for R = -1.

As shown in Figure 7.34, it can be noticed a “double branch” near the threshold in Alloy 2 when two specimens are tested. Microstructural evaluation reveals that there is a difference in pearlite content between the two specimens. In the right specimen in Figure 7.34 there is about 25% pearlite while in the specimen to the left on average 10% (estimation by point counting). Pearlite should not be present in ADI and this is probably due to some error in the casting process.

In specimen 2 (left curve in Figure 7.34) the pearlite distribution is uneven, there is more pearlite on one side. Another difference is the distribution of graphite, in both specimens there is a skeleton of coarse graphite and a finer distribution within the area defined by the coercer graphite. A striking difference is that coarse pearlite stringers appear in conjunction with a band of graphite. There are also areas of local porosities in the left specimen (specimen 1). In specimen 2 the fraction of isolated porosities is about 0,6%.

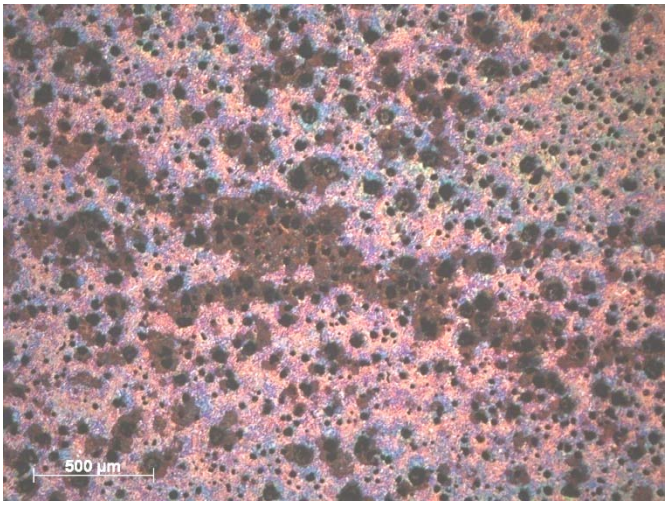

Figure 7:35: Example of pearlite in specimen 2, etched in Picral.

In all other microstructural parameters there are minor differences. Nodularity is between 86 and 93%, nodule count between 153 and 163 nodules/mm^2. Graphite area fraction is practically the same. To conclude, specimen 2 (left curve in Figure 7.34) seems to best represent the properties of a pearlitic free Alloy 2–specimen. Specimen 4 (R = 0) show no sign of pearlite. Reasons for the pearlite appearance is found both in the foundry process (micro segregation and graphite distribution) but also in the heat treatment procedure, possibly to long transfer time between the austenitiation furnace and the salt bath.

Alloy 3 shows a big scattering, particularly in the linear region. That's might be explained by the method chosen to measure the crack propagation rate. Here the local propagaton rate on one of the outer surfaces is measured. According to the standard a smoothing operation should be done which gives a mean value for the propagation rate over the whole cross section. Such a procedure will eliminate most of the scatter but also hide some of the variations caused by the local microstructure.

The slope of the linear region for the different alloys is slightly different. Value of m (constant in the Paris region stating the slope) differs between the two specimens. The specimen with low pearlite content has a m = 3,16 (left curve) and m = 5,15 for the right curve (this specimen have a high pearlitic content, about 25% of the matrix). Alloy 3 has a m value equal to 3,34. Reasons for the difference lie in the pearlite content. In the right curve the pearlite is concentrated to bands of coerce graphite. This is probably due to micro segregation of some chemical elements during solidification of the alloy. It´s

believed that the specimen with the lower pearlite content represents the “true” crack propagation curve for Alloy 2.

The threshold value (ΔK_{th}), equal to the stress intensity range (ΔK) for which the fatigue crack growth rate (da/dN) reaches the minimum value, is 7,20 MPa√m for Alloy 2 and equal to 10,35 MPa√m for Alloy 3. 10,35 MPa√m have a closer resemblance to normal ferritc/pearlitc cast iron.

The graphic in Figure 7.36 shows the comparison of the fatigue crack growth behavior between Alloy 2 and 3 for R = 0.

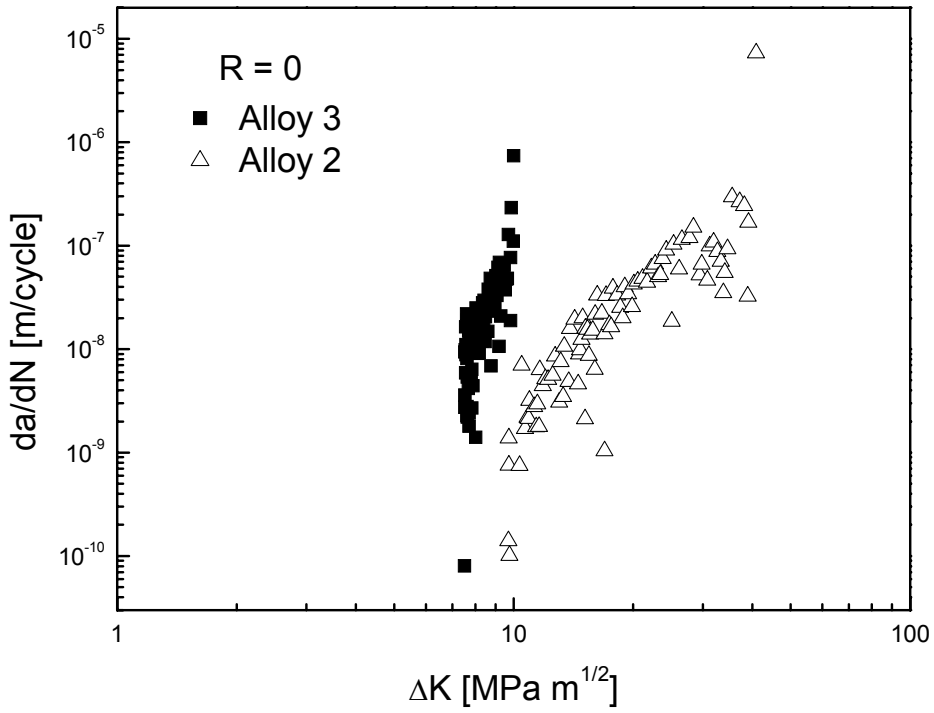

Figure 7.36: comparison of fatigue crack growth behavior of Alloy 2 and 3 for R = 0.

As shown in Figure 7.36, it’s a huge difference between case R = 0 for Alloy 2 and Alloy 3. The m value for Alloy 2 is 3,14, while for Alloy 3 is 4,54. It means that the slope of the Alloy 3 curve is higher than Alloy 2, so the fatigue crack growth rate is higher for Alloy 3 when the crack growth is linear. A striking difference is the nodule count between the two alloys. Alloy 3 has 231 nodules/mm^2 while Alloy 2 has 153 nodules/mm^2. All other parameters are quite the same. As only one specimen is tested for Alloy 3 more investigations must be implemented for this load case.

The threshold value is 9,76 MPa√m for Alloy 2 and 7,53 MPa√m for Alloy 3. According to the results achieved, the crack growth doesn't occur for higher stress intensity range in Alloy 2.

The graphic in Figure 7.37 shows the comparison of the fatigue crack growth behavior of Alloy 2 for R = 0 and -1.

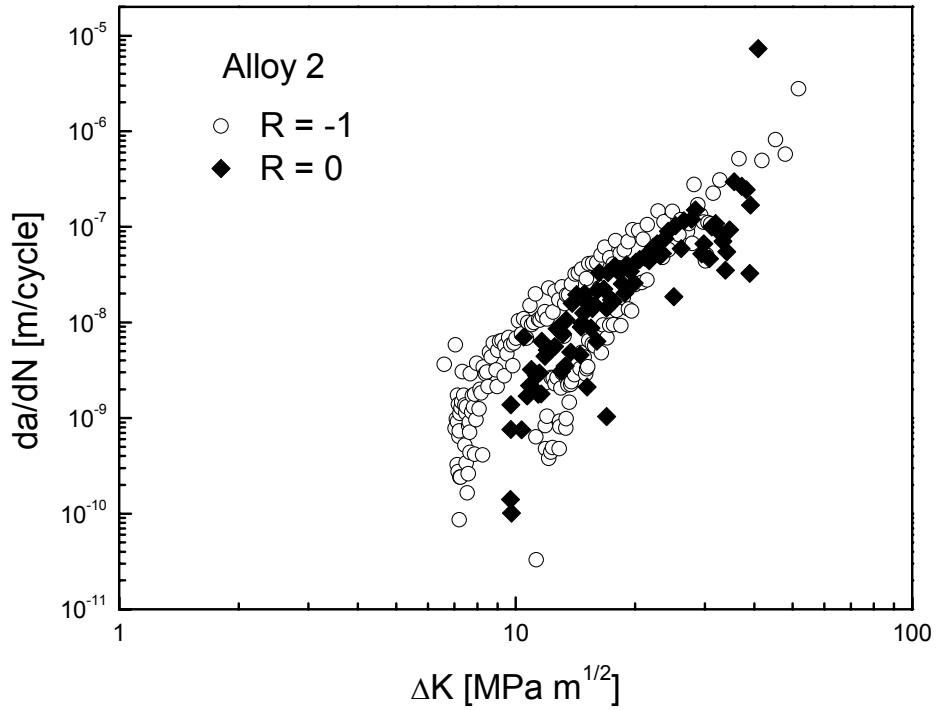

Figure 7.37: comparison of fatigue crack growth behavior of Alloy 2 for R = 0, -1.

As shown in Figure 7.37, the behavior of Alloy 2 at different R is similar. The slope of the linear region for both curves are compared, the value for R=-1 is 3,16 and m=3,14 for R=0. They are practically the same. Load case R=-1 seems to have a slightly higher C-value.

The threshold value of curve for R = 0 is lower than R = -1. They are respectively 9,76 MPa √m (R=0) and 7,20 MPa √m (R=-1).

The graphic in Figure 7.38 shows the comparison of the fatigue crack growth behavior of Alloy 3 for R = 0 and -1.

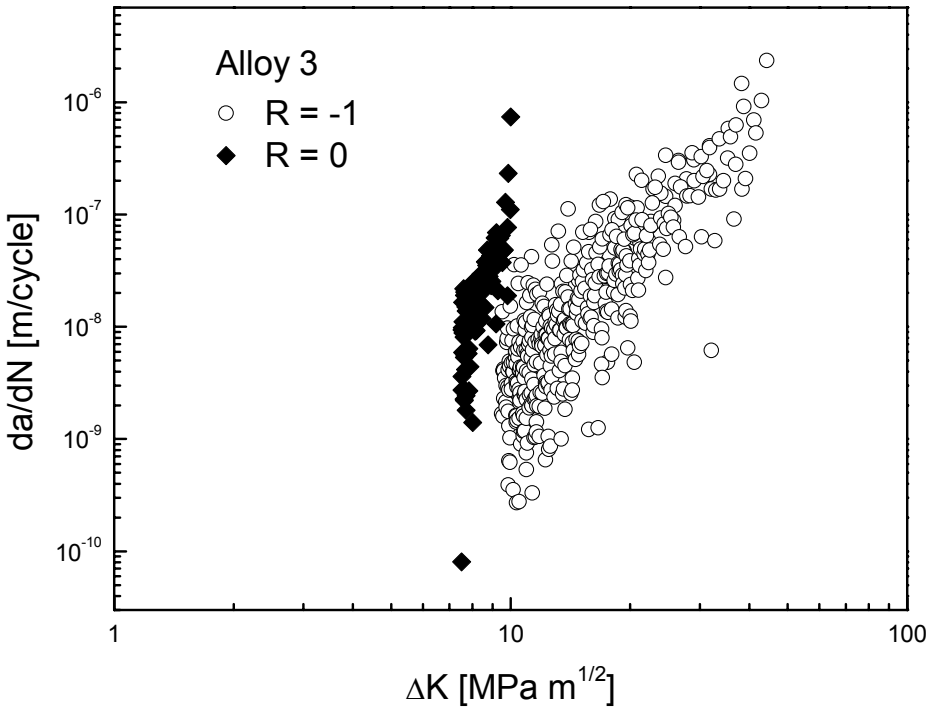

Figure 7.38: comparison of fatigue crack growth behavior of Alloy 3 for R = 0, -1.

As shown in Figure 7.38, Alloy 3 improves the fatigue crack growth behavior when R goes from 0 to -1. The value of m is 4,54 for R = 0 curve and 3,34 for R = -1 curve. It means that the propagation of the crack, in the region where the crack growth rate is linear with the stress intensity range, is faster for R = 0 than R = -1. Anyway the m value for R = -1 is more realistic, probably something didn't work well during the test performed with R = 0.
Also the stress intensity factor near threshold is lower for R = 0, equal to 7,53 MPa√m, compared to R = -1, where is equal to 10,35 MPa√m. It means that the crack growth doesn't occur for higher stress intensity range when R = -1 compared to R = 0.

In the table 7.5 are listed the values of m and ΔK_{th} for all the alloys tested. Besides it was calculated the value of the constant C, which appears in the Paris law.

Material	R	m	C	ΔK_{th} [MPa$\sqrt{m}$]
Alloy 2	-1	3,16	6,3 x10^{-12}	7,20
	0	3,14	2,4 x10^{-12}	9,76
Alloy 3	-1	3,34	2,6 x10^{-12}	10,35
	0	4,54	1,4 x10^{-12}	7,53

Table 7.5: summary of values of m, C and ΔK_{th} for Alloy 2 and 3.

As described before, the value of m raises when R increases from -1 to 0 for Alloy 3, and it is similar for Alloy 2. It means that the crack propagates faster for R = 0 than R = -1, at least in Alloy 3. It must be specified however, that the value measured for Alloy 3 with R = 0 is not realistic compared to the literature. Comparing the different alloys, Alloy 2 shows slower crack propagation (lower values of m that means lower slopes) than Alloy 3. However, considering the m value of Alloy 3 R = 0 less realistic, and the shape of the curve of Alloy 2 R = -1 that shows two branches, the difference between the slope of all the curves is not so large.

On the other hand, ΔK_{th} decreases when R passes from -1 to 0 in Alloy 3, and increases in Alloy 2. It means that the crack growth doesn't occur for higher stress intensity range when R is equal to 0 compared to -1 in Alloy 3, and the opposite happens in Alloy 2. However, more investigations must be implemented for Alloy 3 load case R = 0. Moreover, Alloy 2 has lower values of ΔK_{th} for R = -1, but higher for R = 0. In both cases, the results are not completely clear: in order to the presence of the two branches in the Alloy 2 curve for R = -1 due to pearlite formation and the not realistic results achieved for Alloy 3 R = 0 test, it's hard to conclude which one has the lower stress intensity range near threshold value.

- **Fracture surface analysis**

Some of the specimens after the FCGR tests were analyzed by Light Optical Microscope (LOM) and by Scanning Electron Microscopy (SEM).

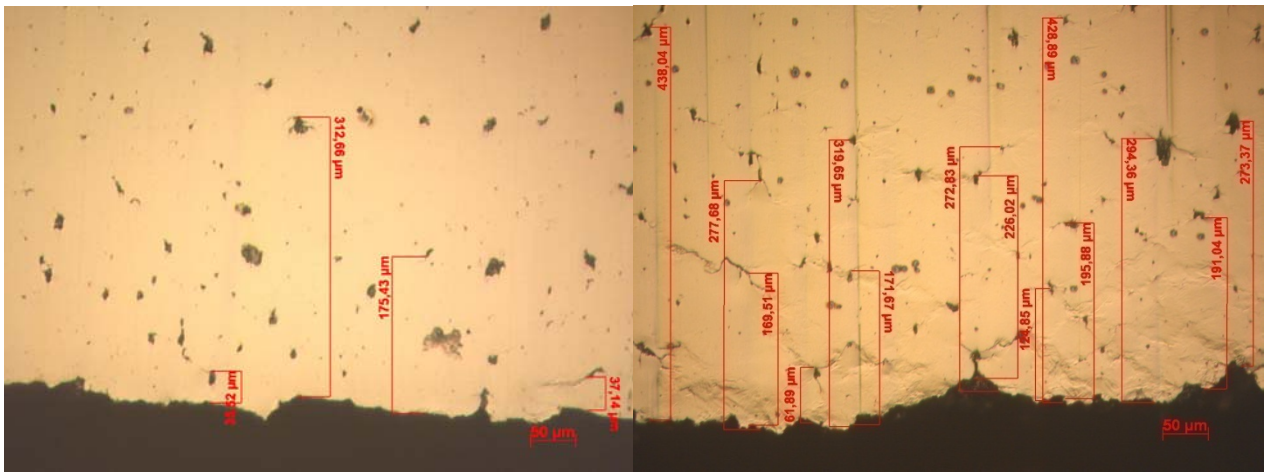

Figure 7.39: fracture surface of Alloy 2 respectively near the notch and on the opposite side.

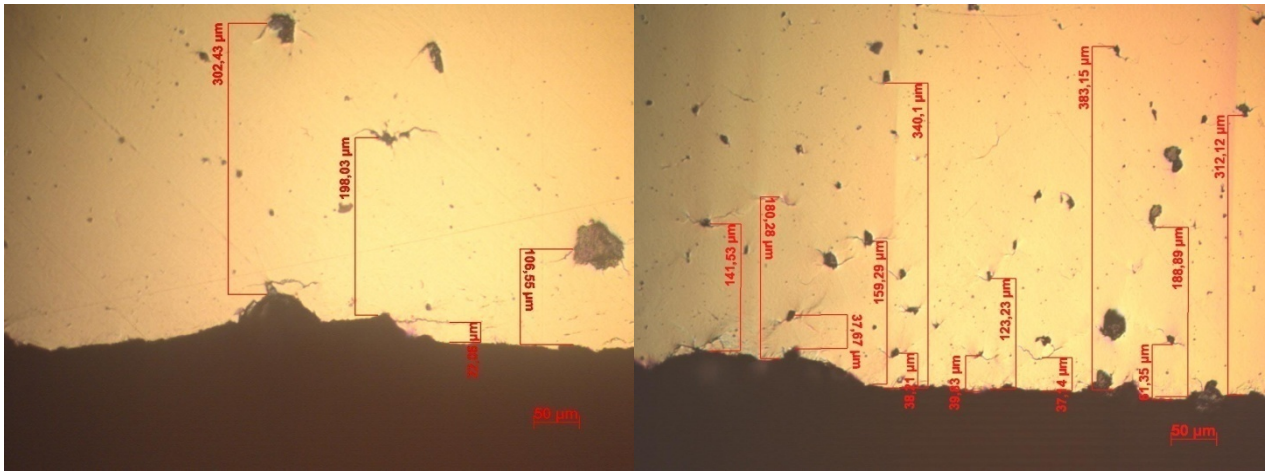

Figure 7.40: fracture surface of Alloy 3 respectively near the notch and on the opposite side.

It can be noticed from the Figures 7.39 and 7.40 that, for both the materials, there are numerous small cracks beyond the main crack which brought to failure. As shown in the images, those cracks are smaller near the notch (low ΔK) compare to the opposite side of the sample, where the main crack is propagating (higher ΔK). These smaller cracks develop mainly in the plastic zone that surround the main crack. Initiation spots seem to bee the scattered isolate micro shrinkages and the graphite nodules. Interesting to observe is that the number of secondary cracks increases in number as the stress

intensity range increases. This observation supports the hypothesis that most of the secondary cracks initiate in the monotonic plastic zone. One other observation is that graphite nodules is the location of most cracks. They act as local stress raisers, according to solid mechanics theory they can give a local stress increase of a factor two to three depending of size and distribution.

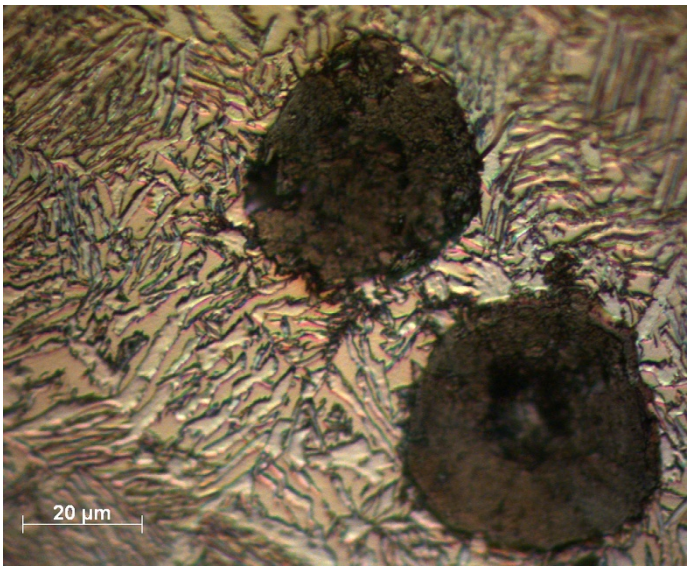

Figure 7.41: Crack initiated at nodules

In Figure 7.41 an example is given of a crack that initiated at the bigger nodule and grows to the left against the neighbour nodule and touches the interface between matrix and graphite. In this case the crack seems to prefer the ferrite/austenite interface, which was also found in [13]. This finding is also supported by measuring on the fracture surface with preliminary XRD analysis that gives a massive ferrite peak and a much smaller austenite peak. However, it can not be ruled out that the crack could entirely propagate in the ferrite, which should be investigated futher.

Observations during the fatigue test are that smaller cracks in front of the main crack grow independent and that some of them join the main crack. This causes variation in the local propagation rate.
Measuring the area fraction of graphite on some of the images of the fracture surfaces by point counting present 20-30 % graphite compared around 10 % of an randomly selected surface. The graphite fraction seems to increase with stress intensity.

- **Fractographic analysis**

An investigation of the fracture surface of some of the FCGR specimens was carried out by Scanning Electron Microscope (SEM), in order to obtain a deeper analysis of the phenomena that takes place during crack propagation.

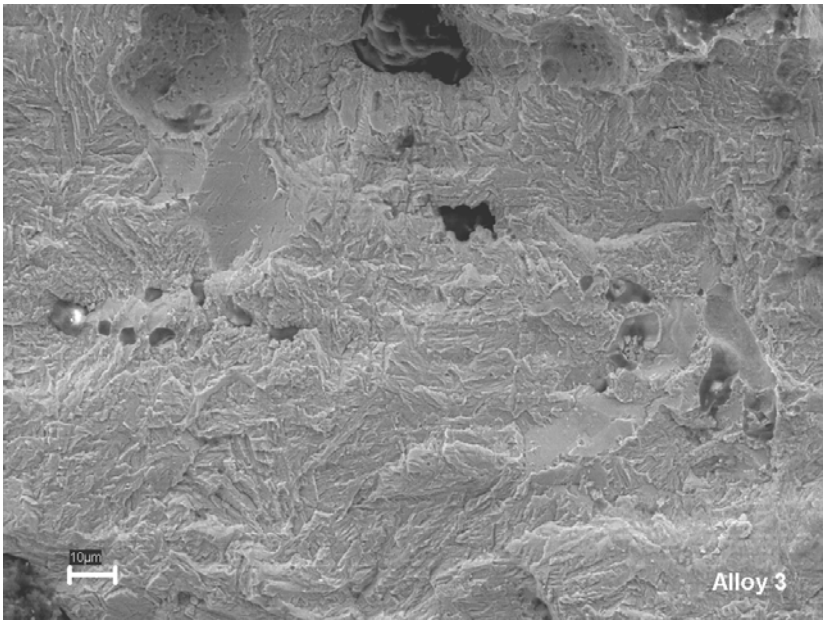

Figure 7.42: A general overview of fracture surface at low ΔK.

Fracture surface in Figure 7.42 represents a good average of what happens at low ΔK levels. Features that seems to guide the crack through the microstructure is shrinkages, graphite nodules and cell boundaries. All these features determine both crack initiation and how the crack chooses its path. Figure 7.42 shows a section around a cell boundary. It appears that the porosity and the cell border graphite initiate the fracture. There are also occasional cleavage facets. A normal fracture surface is ductile. This is clearly visible on the traces of the needles in ausferrite shown in Figure 7.43.

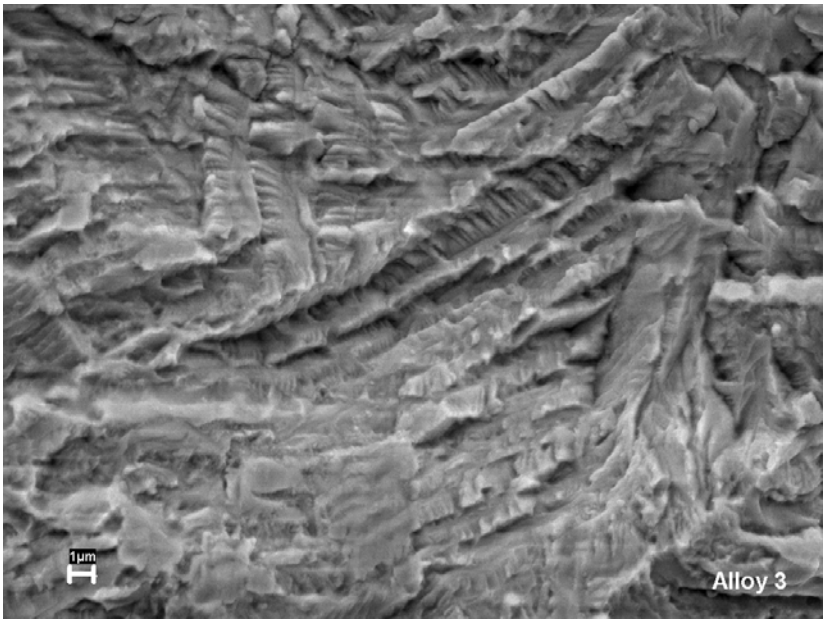

Figure 7.43: close-up of fracture surface, can be clearly seen the needles and can be recognized the ductile fracture.

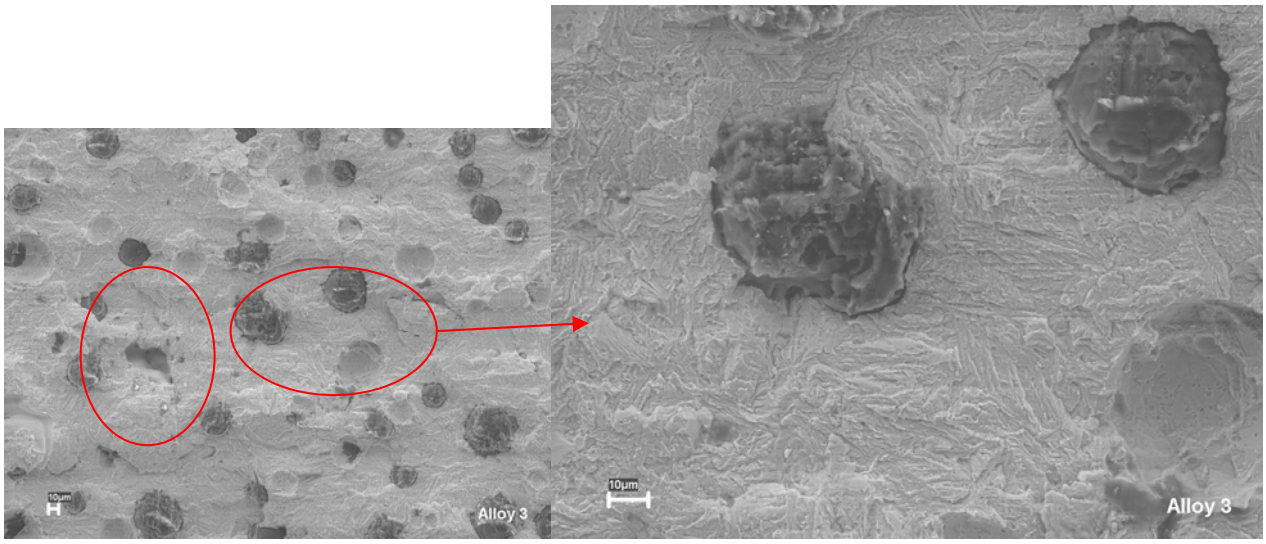

Figure 7.44: close-up of a ductile fracture with nodules.

Figure 7.44 shows that there is a small plastic activity around the nodules, this is typical of fatigue. It is also clear that there is an increased amount of graphite nodules on fracture surface, including detachment of nodules. This suggests that nodules govern the fracture process. The small picture on the left also shows that a cell boundary with the graphite particles and a very small suction.

It can be seen in Figure 7.45 that the nodules seem to be intimately linked to the matrix, so there are large number nodules that is "broken". Besides, it could be noticed that the

fracture area, especially at low ΔK, show less topography compared to fracture surfaces at higher stress intensities.

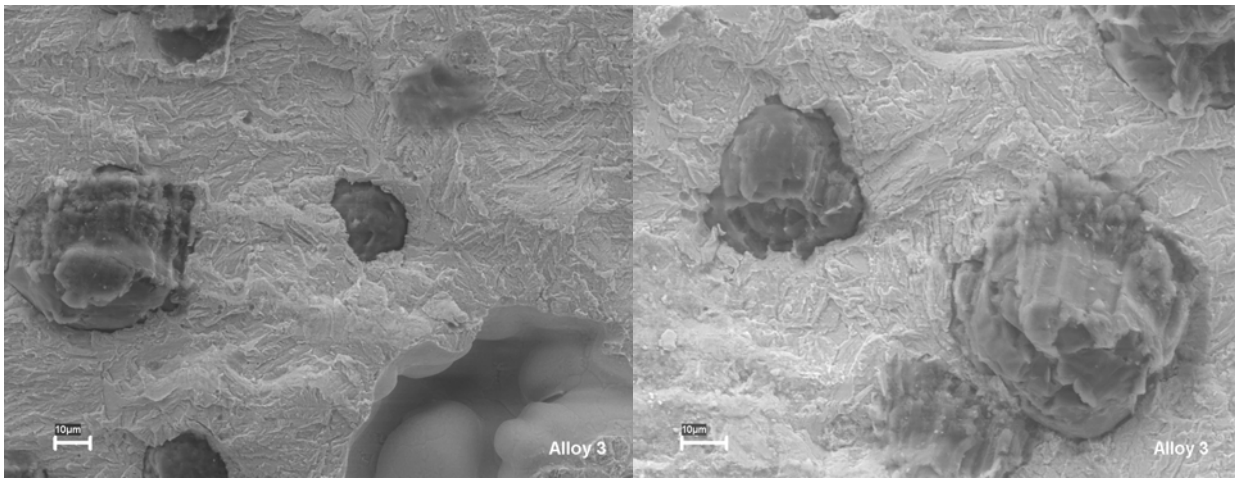

Figure 7.45: broken nodules and damaged "flattened" areas.

When ΔK increases, the number of secondary cracks increases in number (Figure 7.46). It is interesting to notice that these cracks are main cracks along the growth direction, but they seem to go down into the test specimen.

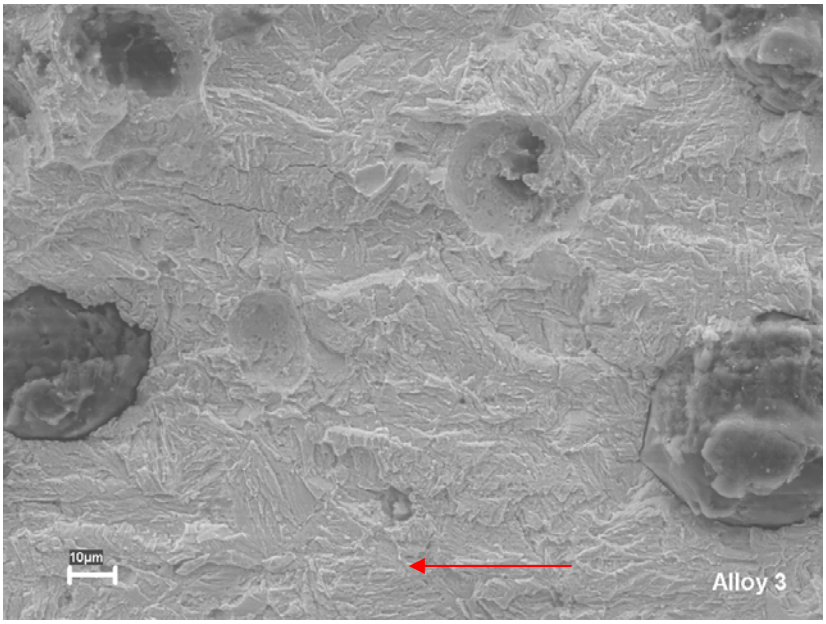

Figure 7.46: secondary crack between nodules, the arrow shows the main crack growth direction.

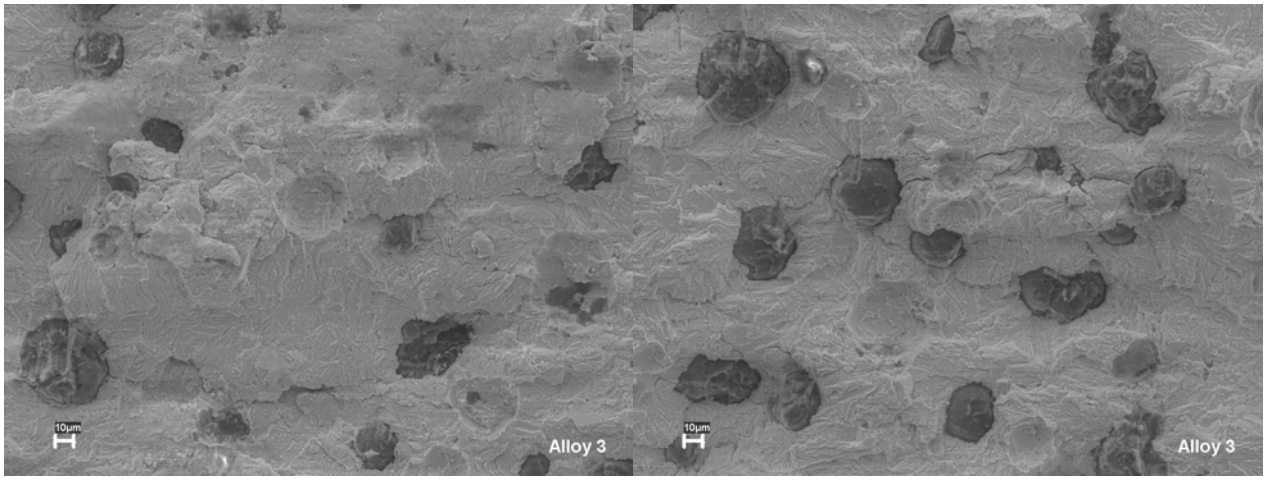

Figure 7.47: the main crack direction showed in Figure 7.46.

It was noticed that the secondary cracks usually are parallel to the main crack on specimens surface. Secondary cracks in the center of the rod appear to be twisted 90 degrees, compared with the outer surface.

Point counting on some of the images shows that the amount of graphite on the surface is around 20%, the corresponding estimate of normally ductile iron is around 30%. This may indicate that the matrix has a greater impact in ADI if it is compared with normal ductile iron.

8. CONCLUSION

The aim of the study was to evaluate the impact and the fatigue properties of Austempered Ductile Iron.

The impact energy was found to be related with the morphology of graphite nodules. Improved impact properties were obtained when the nodularity and the nodule count increased. On the other hand, the impact energy decreased when the nodule size increased. However in this work, the effect of the amount of retained austenite was found to be less important than the graphite nodules. Moreover, the impact properties are strongly affected by the defects like porosity, carbides and segregation mainly, but, also the formation of martensite. They are the cause of the scattering achieved in the impact energies and explain the lower values obtained in the middle location of the rings.

From investigating the fracture mechanism that occurs in ADI, it was observed that the crack path preferentially intersects the graphite nodules. This is also a possible explanation why the graphite nodules were more important for the fracture mechanism than the retained austenite, which was also observe for the impact test. In this work, the most dangerous crack initiator was found to be the pores, but also the carbides and the nodule/matrix interface. The decrease of properties associated to the debonding of graphite nodules is made easier with nodule size increases.

It was observed that the crack growth between two neighboring nodules depends on the orientation of the ferrite laths. In fact the crack growth can take place along the austenite/ferrite interface or cut the ferrite laths. In this work, it was found that the crack path probably takes place along the austenite/ferrite interface, but this should be investigated further.

For the fatigue test, faster crack propagation was found for R = 0 than R = -1 in Alloy 3 and similar in Alloy 2. However, the value measured for Alloy 3 with R = 0 is not consistent to that found in literature in terms of m value. Comparing the different alloys, the difference between the slope of all the curves is not so large. Alloy 2 shows slower crack propagation than Alloy 3, despite of Alloy 2 at R = -1 had a curve shape with two branches.

On the other hand, ΔK_{th} decreases when R passes from -1 to 0 in Alloy 3, and increases in Alloy 2. It means that the crack growth doesn't occur for higher stress intensity range when R is equal to -1 compared to 0 in Alloy 3, and the opposite happens in Alloy 2. Comparing different alloys at the same load case, Alloy 3 has higher threshold value than Alloy 2 for R = -1, and lower for R = 0. Although, the results are not completely clear: the formaton of pearlite affected the test, it should not be present in ADI and this is probably due to some error in the casting process.

The fracture surface analysis of fatigue samples showed that the number of secondary cracks increases in number as the stress intensity range increases. Besides, the graphite nodules are the location of most cracks, due to the local stress increase.
Observations during the fatigue test are that smaller cracks in front of the main crack grow independent and that some of them join the main crack. This causes variation in the local propagation rate.
Measuring the area fraction of graphite on some of the mages of the fracture surfaces by point counting present 20-30 % graphite compared around 10 % of an randomly selected surface. The graphite fraction seems to increase with stress intensity.

9. REFERENCES

[1] E. Dorazil, *High strength Austempered Ductile Cast Iron*, Ellis Horwood series, translation editor: H. Morrogh, 1991

[2] http://www.durhamfoundry.com/austempered_ductile_iron.htm

[3] http://www.aditreatments.com/background.php

[4] J. Hidalgo, *Improving the Fracture Toughness of Dual-phase Austempered Ductile Iron*, Master Thesis, Department of Material and Manufacturing Technology, Chalmers University of Technology, Göteborg, Sweden 2008, Chalmers Tekniska Högskola ISSN 1652-8913

[5] C.Glondu, *Improving the Toughness of Austempered Ductile Iron*, Master Thesis, Department of Material and Manufacturing Technology, Chalmers University of Technology, Göteborg, Sweden 2007, Chalmers Tekniska Högskola ISSN 1652-8913

[6] http://www.ductile.org/didata/section4/4intro.htm

[7] http://www.aditreatments.com/applications.php

[8] Y. Tanaka, H. Kage, *Mater. Trans.* JIM

[9] B. V. Kovacs, *Modern Casting*, 1990

[10] S. K. Putatunda, P. K. Gadicherla, *Effect of Austempering Time on Mechanical Properties of a Low Manganese Austempered Ductile Iron*, Department of Chemical Engineering and Materials Science, Wayne State University, Detroit, Journal of Materials Engineering and Performance, vol. 9(2), pp. 193-203, 2000

[11] http://www.advancedcast.com/austempering-process.htm

[12] C.-K. Lin, P.-K. Lai, T.-S. Shih, *Influence of microstructure on the fatigue properties of austempered ductile irons-I. High-cycle fatigue*, Department of Mechanical Engineering, National Central University, Taiwan, International Journal of Fatigue vol. 18, No. 5, pp. 297-307, 1996

[13] C.-K. Lin, T.-P. Hung, *Influence of microstructure on the fatigue properties of austempered ductile irons-II. Low-cycle fatigue*, Department of Mechanical Engineering, National Central University, Taiwan, International Journal of Fatigue vol. 18, No. 5, pp. 309-320, 1996

[14] C.-K. Lin, Y.-L. Pai, *Low-cycle fatigue of austempered ductile irons at various strain ratios*, Department of Mechanical Engineering, National Central University, Taiwan, International Journal of Fatigue vol. 21, No. 1, pp. 45-54, 1999

[15] G. L. Greno, J. L. Otegui, R. E. Boeri, *Mechanism of fatigue crack growth in Austempered Ductile Iron*, University of Mar de la Plata, Argentina, International Journal of Fatigue vol. 21, No. 1, pp. 35-43, 1999

[16] M. D. Chapetti, *High-cycle fatigue of austempered ductile iron (ADI)*, INTEMA (Institute for Materials Science and Technology), CONICET-University of Mar de la Plata, Argentina, International Journal of Fatigue vol. 29, pp. 860-868, 2007

[17] B. Stokes, N. Gao, K. K. Lee, P. A. S. Reed, *Effects of Carbides on Fatigue Characteristics of Austempered Ductile Iron*, University of Southampton, UK, Metallurgical and Materials Transactions A, vol. 36A, pp. 977-988, 2005

[18] M. Cavallini, O. Di Bartolomeo, F. Iacovello, *Fatigue crack propagation damaging micromechanism in ductile cast irons*, University of Roma La Sapienza and Cassino, Italy, Engineering Fracture Mechanics, vol. 75, pp.694-704, 2008

[19] C.-K. Lin, C.-W. Chang, *Influence of heat treatment on fatigue crack of austempered ductile iron*, Department of Mechanical Engineering, National Central University, Taiwan, Journal of Materials Science, vol. 37, pp. 709-716, 2002

[20] J. Luo, R. A. Harding, P. Bowen*, Evaluation of Fatigue Behavior of Ductile Irons with Various Matrix Microstructures*, University of Birmingham, UK, Metallurgical and Materials Transactions A, vol. 33A, pp. 3719-3730, 2002

[21] P. P. Rao, S. K. Putatunda*, Influence of Microstructure on Fracture Toughness of Austempered Ductile Iron*, Department of Chemical Engineering and Materials Science, College of Engineering, Wayne State University, Detroit, Metallurgical and Materials Transactions A, vol. 28A, pp. 1457-1470, 1997

[22] G. Francucci, J. Sikora, R. Dommarco, *Abrasion resistance of ductile iron austempered by the two-step process*, University of Mar de la Plata, INTEMA, CONICET, Argentina, Materials Science and Engineering A, vol. 485, pp. 46-54, 2008

[23] I. Riposan, M. Chisamera, L. Sofroni, *Cast Met.*, 1990, vol. 2, pp. 207-213

[24] R. C. Voigt, C. R. Loper, *Proc. 1st Int. Conf. on Austempered Ductile Iron*, Chicago, 1984

[25] R. C. Voigt, *Ph. D. Thesis*, University of Winsconsin-Madison, 1981

[26] E. V. Pereloma, C. S. Anderson, *Microstructure and properties of austempered ductile iron subjected to single and two step processing*, Department of Materials Engineering, Monash University, Victoria, Australia, Materials Science and Technology, vol. 22, No. 9, pp. 1112-1118, 2006

[27] S. K. Putatunda, P. V. Gadicherla, *Effect of Austempering Time on Mechanical Properties of a Low Manganese Austempered Ductile Iron*, Department of Chemical Engineering and Materials Science, College of Engineering, Wayne State University, Detroit, Journal of Materials Engineering an Performance, vol. 9, pp.193-203, 2000

[28] ASTM Handbooks, volume 4 *Heat treating*, section *Quenching media for austempering*

[29] ASTM Handbooks, volume 4 *Heat treating*, section *Equipment and Processing*

[30] ASTM Handbooks, volume 4 *Heat treating of Ductile Irons*, section *Quenching and Tempering Ductile Iron*

[31] L. Pook, *Metal Fatigue: what it is, why it matters*, Solid Mechanics and its Applications, vol. 145, Springer, 2007

[32] J. Schijve, *Fatigue of Structures and Materials*, Kluwer Academic Publishers, 2001

[33] R. I. Stephens, A. Fatemi, R. R. Stephens, H. O. Fuchs, *Metal Fatigue in Engineering*, John Wiley & Sons, Second Edition, 2001

[34] G. I. Rees, H. K. D. H. Bhadeshia, *Material Science and Technology*, vol. 8, pp. 985-993, 1992

[35] N. A. Chester, H. K. D. H. Bhadeshia, Journal of Physics IV, vol. 7. C5, pp. 41-46, 1997

[36] E. V. Pereloma, S. H. Zahiri, C. H. J. Davies, *Material Science and Technology*, vol.17, pp. 1563-1568, 2001

[37] E. V. Pereloma, S. H. Zahiri, C. H. J. Davies, *Material Science and Technology*, vol.18, pp. 1163-1167, 2002

[38] M. Delia, M. Alaalam, M. Grech, *Effect of Austenitizing Conditions on the Impact Properties of an Alloyed Austempered Ductile Iron of Initially Ferritic Matrix Structure*, Department of Metallurgy and Materials, Faculty of Engineering, University of Malta, Journal of Materials Engineering and Performance, vol. 7(2), pp.265-272, 1998

[39] O. Erić, M. Jovanović, L. Šidanin, D. Rajnović, S. Zec, *The austempering study of alloyed ductile iron*, Materials and design, vol. 27, pp. 617-622, 2006

[40] Bayati, Elliott, Materials Science and Technology, 11:285, 1995

[41] Hamid Ali AS, Uzolov KI, Darwish N, Elliott R, Materials Science and Technology, 10:35, 1994

[42] T. Skaland, D. Grog, *Nodule Distribution in Ductile Cast Iron*, AFS Trans., vol. 56, pp. 153-157, 1991

[43] B.Y. Lin, E.T. Chen, T.S. Lei, *The Effect of Segregation on the Austemper Transformation and Toughness of Ductile Irons*, Department of Mechanical Engineering and Technology, National Taiwan Institute of Technology, Taipei, Taiwan, Journal of Materials Engineering and Performance, vol. 7(3), pp. 407-419, 1998

[44] C. S. Roberts, *Trans AIME*, 1953, vol. 197 pp.203-206

[45] H. Bayati, R. Elliott, *Austempering process in high-manganese alloyed ductile cast iron*, Mat. Sci. Tech., 11, 284-293 (1995)

[46] K. Hamberg, *Microstructural Influence on the Fatigue Properties of Steels*, Department of Engineering Metals, Chalmers University of Technology, Göteborg, Sweden 1986